Mikada, H., Becker, K., Moore, J.C., Klaus, A., et al., 2002
Proceedings of the Ocean Drilling Program, Initial Reports Volume 196

3. Site 1173[1]

Shipboard Scientific Party[2]

SITE SUMMARY

We drilled Holes 1173B and 1173C to obtain logging-while-drilling (LWD) data at a reference site on the seaward flank of the Nankai Trough and to install an Advanced CORK (ACORK) long-term subseafloor hydrogeologic monitoring experiment. These holes complement Hole 1173A, which was cored from the surface to basement during Leg 190. This site provides a basis for comparison of physical and chemical properties between the incoming undeformed sediments and rocks of the Shikoku Basin with deformed materials of the accretionary prism and underthrust sediments cored at sites to the northwest.

At Site 1173, the LWD tools measured resistivity at the bit (RAB), sonic velocity, density, porosity, natural gamma ray production, and photoelectric effect from the seafloor to basaltic basement (Fig. F1). Additionally, the tools provided estimates of hole size and borehole resistivity images. A measurement-while-drilling (MWD) system provided information on weight on bit, torque, heave, resistivity, density, and sonic velocity that was communicated to the surface and displayed instantaneously during drilling.

Log Quality

The overall quality of the LWD logs recorded in Holes 1173B and 1173C is excellent. The LWD logs generally agree with the more limited Hole 1173A wireline logs. In Holes 1173B and 1173C, the drilling rate was maintained between 35 and 60 m/hr throughout the section and all measurements were made within 1 hr of bit penetration. At least two depth points were measured in each 0.3-m interval. The caliper shows that the gap between the bit radius and the hole is <1 in throughout both holes, with the exception of the uppermost 75 m of Hole 1173C, where soft sediment washed out a gap up to 2 in long. Therefore, the

F1. Site 1173 summary diagram, p. 38.

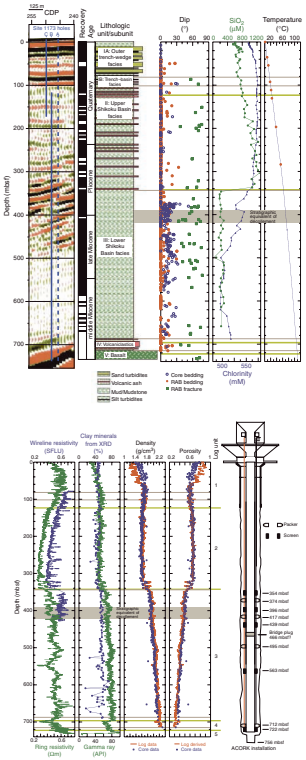

[1]Examples of how to reference the whole or part of this volume. [2]Shipboard Scientific Party addresses.

Ms 196IR-103

density log over this shallowest 75-m interval is unreliable. This was the first ever use of the LWD Anadrill Integrated Drilling and Logging (IDEAL) sonic-while-drilling (ISONIC) velocity tool in such fine-grained, unlithified sediment and the first use ever by the Ocean Drilling Program (ODP). Although the tool worked well, the processing of the waveforms was not straightforward and will have to be improved postcruise to yield reliable sonic velocity data.

Log Units and Lithology

Both visual and multivariate statistical analyses of the logs define five log units that account for the lithologic variations observed in the cores.

A high variability in the differential caliper log and a large number of caliper values >1 in reflect bad borehole conditions during drilling of the upper 75 m of log Unit 1 (0–122 meters below seafloor [mbsf]). This log unit shows high neutron porosity and low density values with a high standard deviation. These variations might be in part real and reflect the presence of silt and sand turbidites of the outer trench–wedge facies. A significant decrease in resistivity, density, and gamma ray and an increase in neutron porosity with depth show an abnormal compaction trend and define log Unit 2 (122–340 mbsf). This log unit correlates with lithologic Unit II (102–344 mbsf), which consists of hemipelagic mud with abundant interbeds of volcanic ash. The low density could be related to a cementation effect caused by the formation of cristobalite. The log Unit 2/3 boundary correlates with the diagenetic phase transition between cristobalite and quartz. High gamma ray, density, and photoelectric effect log values that increase continuously with depth characterize log Unit 3 (340–698 mbsf). Resistivity and, less obviously, gamma ray logs show a cyclicity of values (480–700 mbsf) that reflects changes in lithology, which may in turn reflect an interbedding of coarser and finer grained sediments. Log Unit 4 (698–731 mbsf) is defined by broad variations in photoelectric effect, resistivity, neutron porosity, and gamma ray logs that correlate well with the presence of the volcaniclastic facies of lithologic Unit IV (688–724 mbsf). Log Unit 5 (731–735 mbsf) shows an abrupt increase in resistivity and a decrease in gamma ray log values, which characterize the basaltic oceanic basement.

Structural Geology

Structural data determined from RAB images of medium-focused resistivity (penetration depth 7.6 cm beyond standard borehole radius) indicate sparse deformation and predominantly subhorizontal bedding dips. Increases in bedding dips (5°–35°) at 50–200 mbsf and below ~370 mbsf are in agreement with core data from Leg 190 Hole 1173A. Fractures are oriented at high angles (40°–80°), show normal displacement where measurable, and have variable strike orientation. Resistive fractures dominate and might reflect nonconductive clay gouge, mineralization, or porosity collapse due to compaction. An increase in fracture intensity occurs at 380–520 mbsf, correlating with an increase in bedding dip. The upper limit of this zone corresponds to the projected stratigraphic equivalent of the décollement zone. At ~500 mbsf, bands of heterogeneous (mottled) high resistivity are thought to represent zones of intense deformation or brecciation. In general, the deformation observed in Holes 1173B and 1173C is consistent with extensional

faulting probably related to basinal compaction and burial and not to propagating compressional deformation from an accretionary wedge.

Physical Properties

LWD density data in Holes 1173B and 1173C closely match core physical properties data from Hole 1173A, except for the uppermost 60 m, where differential caliper values exceeded 1 in. LWD densities are nearly constant in log Subunit 1b (55–122 mbsf) and Unit 2 (122–340 mbsf), with the notable exceptions of two high-amplitude variations near the transition from lithologic Unit II (upper Shikoku Basin facies) to III (lower Shikoku Basin facies). Log Unit 3 (340–698 mbsf) is characterized by a steady increase in density consistent with normal compaction. The LWD resistivity logs clearly respond to the lithologic boundaries identified in Hole 1173A. Within log Unit 2 resistivity decreases with depth while density is constant, whereas in log Unit 3, resistivity is about constant with depth and density increases. All LWD resistivity logs show a similar overall trend, in good agreement with wireline logs, where available. Shallow button resistivities that are consistently higher than medium and deep resistivities is an unusual and unexplained feature of Site 1173 LWD data.

Logs and Seismic Reflection Data

The velocities from the core and wireline data and densities from the core and LWD data from 0 to 350 mbsf were used to generate a synthetic seismogram in good agreement with the seismic reflection data. Good correlations exist between the synthetic seismogram and the seismic reflection data at ~80–100 (trench–basin transition facies), ~175, ~265–270, and ~300–350 mbsf (associated with the upper to lower Shikoku Basin unit boundary and the log Unit 2/3 boundary). A change in physical properties associated with the phase transition from cristobalite to quartz may be, in part, responsible for this reflection. High reflectivity in the synthetic seismogram beneath ~350 mbsf does not match with the low reflectivity in the seismic data of the lower Shikoku Basin unit (log Unit 3) and may be caused by a sampling bias in the core velocity measurements.

ACORK Installation and Basement Coring

A four-packer, five-screen, 728-m-long ACORK string (Fig. F1) was deployed through the sediment section in Hole 1173B, configured to emphasize long-term observations of pressures in three principal zones, as follows:

1. Oceanic basement below 731 mbsf, to determine permeability and pressures in young oceanic crust being subducted, and thereby assess the role of oceanic crust in the overall hydrogeology of the Nankai Trough. A screen was installed immediately above the ACORK shoe, centered at 722 mbsf, and a packer was placed immediately above the screen.
2. Lowermost Shikoku Basin deposits, well below the stratigraphic projection of the décollement zone, to assess the hydrological properties of a reference section of the lower Shikoku Basin deposits and test for fluid pressure propagation from basement or

possibly higher in the section. A packer was centered at 495 mbsf to isolate a screen centered at 563 mbsf.

3. The stratigraphic equivalent of the décollement zone at ~390–420 mbsf in the upper part of the lower Shikoku Basin deposits seaward from Sites 1174 and 808. A symmetric array ~100 m long, comprising three screens separated by two packers, was built into the ACORK string such that the three screens were centered at 439, 396, and 353 mbsf. Objectives of this array include (1) documenting the variation of hydrogeologic properties across and away from this zone as a reference for the state of the formation before the décollement zone actually develops closer to the trench axis and (2) detecting the possibility of elevated fluid pressure or fluid flow along the stratigraphic projection of the décollement zone. In addition, the central screen in this array (i.e., the screened interval that spans the stratigraphic equivalent of the décollement zone) includes a second small-diameter line for eventual sampling of formation fluids from the wellhead.

After installation of the ACORK, the rotary core barrel (RCB) coring bottom-hole assembly (BHA) was successfully deployed through the ACORK casing to deepen the hole into basement to assure that the signal of basement hydrogeologic processes will be transmitted to the deepest screen. A total of 19.5 m into basement was cored, with a recovery of 5.2 m (27% recovery). The core comprises basaltic basement overlain by a thin veneer of volcaniclastics.

Following basement coring, the final step in the ACORK installation at Hole 1173B was deployment of a bridge plug to seal the bore of the casing and isolate the basement section to be monitored by the deepest screen. This was intended to be set very near the bottom of the ACORK string, allowing future deployment of other sensor strings within the central bore. However, the bridge plug apparently set prematurely at 466 mbsf; this was not sensed at the rig floor, and ensuing operations resulted in breaking the pipe off at the ACORK head. Nevertheless, detailed analysis suggests that the bridge plug is indeed set, and a video inspection confirmed that there is no broken pipe outside the ACORK head to inhibit future data recovery operations.

BACKGROUND AND OBJECTIVES

Site 1173 is located in the outer margin of the trench fill of the Nankai Trough ~11 km seaward of the deformation front (Fig. F2). Cored to basement during Leg 190, Site 1173 provides a reference for the physical and chemical nature of the sediments at the subduction zone, before they are deformed either by incorporation into the accretionary prism or by being underthrust beneath the décollement zone. Such reference sites are essential in understanding processes at subduction zones because changes in the sediments entering the subduction zone occur rapidly.

Site 1173 penetrates ~80 m of the trench-wedge deposits and all of the subjacent sequence of the Shikoku Basin (Shipboard Scientific Party, 2001). At Sites 1174 and 808, this reference section is buried by more than 350 m of trench sediments (Moore et al., 2001) (Fig. F3). The "Leg 196 Summary" chapter and Moore et al. (2001) provide additional topical and regional background for Site 1173.

F2. Locations of Leg 196 drill sites, p. 40.

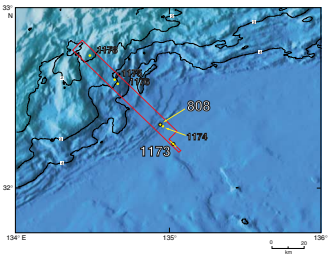

F3. Seismic line crossing Site 1173, p. 41.

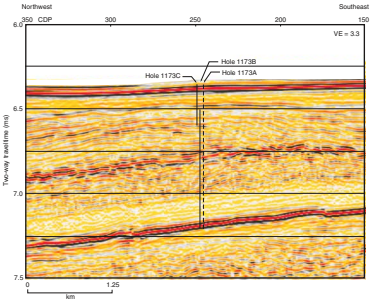

Legs 190 and 196 shared similar goals at Site 1173: to determine the physical and chemical state of the section incoming to the subduction zone as a reference in an overall program to define the interrelationship of the dynamics of deformation and fluid flow processes in an accretionary prism characterized by thick terrigenous sediments. Whereas Leg 190 approached these goals by coring, Leg 196 focused on the collection of LWD data and emplacement of a long-term ACORK hydrogeologic observatory at the site. Leg 196 sought to obtain a set of borehole logs and long-term hydrogeologic measurements that could be combined with the existing core and seismic reflection data to best define the initial state of materials incoming to the Nankai Trough along the Muroto Transect (Moore et al., 2001).

Specific Leg 196 objectives at Site 1173 included

1. Determination of density, porosity, resistivity, and sonic velocity profiles through the incoming sedimentary section;
2. Resolution of any physical properties variations across the projected stratigraphic level of the décollement zone, termed the "stratigraphic equivalent of the décollement zone" herein;
3. Deployment of the first ever ACORK observatory for (1) long-term investigation of fluid pressures and temperatures in basement, the lower Shikoku Basin sequence, and across the stratigraphic equivalent of the décollement zone and (2) eventual fluid sampling from any permeable zones;
4. Coring into basement through the ACORK; and
5. Measurement of resistivity of the sediments and underlying oceanic basement to constrain future regional electromagnetic surveys.

OPERATIONS

An operations summary of Leg 196 Site 1173 is presented in Table T1. Previous Leg 190 operations at Site 1173 are reported in Moore, Taira, Klaus, et al. (2001).

T1. Site 1173 operations, p. 84.

Keelung, Taiwan, Port Call

Leg 196 began with the first line ashore to Berth 4-E East Wharf, Keelung, Taiwan, at 0904 hr on 2 May 2001. Public relations tours were held each day with members of the press. VIP tours (including Chinese Taipei's vice president) were conducted on 4 May, and the bulk of the visitors were on board on 5 and 6 May. Major port call activities consisted of removing geochemical radioactive sources from the ship and loading a considerable amount of equipment, including ACORK casing (260 joints) and hardware, the Anadrill LWD/MWD tools, and 120 tons of sepiolite.

Immigration formalities were completed on 2 May, and the loading of 700 metric tons of fuel from 100–metric ton barges was finished at 2050 hr. Divers inspected the thrusters and main propulsion system to ensure they were not fouled by fishing lines during Leg 195. Additional inspection dives were conducted on the afternoon of 3 May.

On 3 May the vessel was shifted 40 ft astern to make room for other ships berthing at the dock; the incoming air freight and food were loaded. We then unloaded surface freight containers, placed the freight

onto the dock, and began loading it onto the ship. The Anadrill MWD/LWD tools were unloaded onto the dock, and the Anadrill engineers began dockside assembly and testing. The loading of the bulk sepiolite began, with a pneumatic truck used to transfer it onto the ship; 56 tons was loaded. Liquid helium was received, and the cryogenic magnetometer was filled.

After considerable efforts to coordinate logistics and obtain permits, the two radioactive sources for the geochemical logging tool were taken off the drillship on 4 May. Then we were allowed to load the sources for the LWD/MWD logging tools onto the ship. On 4 May the Anadrill engineers continued unloading and testing the LWD/MWD tools, and the remaining 64 short tons of bulk sepiolite was loaded. The trucks carrying the 10¾-in and 20-in casing began arriving, and we started to unload and stage it on the dock; during this process each joint was measured and labeled.

On 5 May, assembly and testing of the LWD/MWD tools continued, the casing handling and loading continued, and the off-going freight was taken off the ship. By 0830 hr on 6 May, all casing had been loaded. A total of 226 joints of 10¾-in casing was stored in the riser hold, and 36 joints of 20-in casing was stored in the riser hold, as well as on top of the riser hold hatch, as the riser hold was full. The LWD/MWD tool testing was completed, the tools were loaded, and the crew began securing the ship for departure.

Transit from Keelung to Site 1173

The last line away from Keelung was at 0900 hr on 7 May. The transit to Site 1173 began at 0930 hr, when the harbor pilot disembarked. After a transit of 784 nmi we arrived at the Global Positioning System (GPS) coordinates of Site 1173 (32°14.6634′N, 135°1.5085′E) at 0645 hr on 10 May.

During the transit, the rig crew assembled the first reentry cone; it was moved into position on the moonpool doors in preparation for deployment. Repairs were made to the underreamer used during Leg 195 (seal replacements, 22-in cutter sets changed, and jet function verified). The rig crew performed preventive rig maintenance and repairs.

The ship experienced a power interruption during the transit (at 2347 hr on 8 May) caused by a shutdown of main engine 2 due to high crankcase pressure. This resulted in a slight reduction in speed that lasted 15 min. Repairs to the piston pin and insert carrier on cylinder 7 were made, and complete preventive maintenance was performed on this engine.

In preparation for operations at Site 1173, we attached a used 18½-in tricone mill-tooth bit (Hughes X44) to the 22-in underreamer. This, in turn, was made up to an 8¼-in positive displacement mud motor (Baker-Hughes Drilex model D825MSHF), and the assembly was tested. The pressure drop at a flow rate of 275 gallons per minute (gpm) was low (75 psi) and leakage high, so we changed to a backup mud motor that had a 125-psi pressure drop at 275 gpm. The Dril-Quip cam-actuated drill-ahead (DQ CADA) casing running tool was made up to the 20-in casing hanger and a short (pup) joint of casing.

Site 1173

Hole 1173B

At 0645 hr on 10 May, we arrived on location, lowered the thrusters and hydrophones, and started making up five stands of drill collars. A positioning beacon was not immediately deployed because the scientists requested an offset of 50 m at 314° from the position of Hole 1173A, which was cored during Leg 190; the ship maintained station by using GPS. The ship was over the desired position of Hole 1173B at 0810 hr on 10 May, and a seafloor positioning beacon (Datasonics SN2031; 14.0 kHz; 214 dB) was deployed at 0835 hr.

Reentry Cone and Casing Operations

At 1200 hr on 10 May, we began rigging up to run 20-in casing by welding a casing guide shoe to the bottom joint and then adding nine more joints of casing. This casing was then added to the short (pup) joint of 20-in casing attached to the bottom of the casing hanger that was already latched to the casing running tool; the total length of this assembly was 120.6 m. This assembly was then landed and latched into the reentry cone at 1845 hr; the running tool was unlatched so that the BHA could be run into the casing.

Next, we began assembling and running the drilling BHA into the casing. The BHA consisted of the 18½-in bit, 22-in underreamer, bit sub with float, mud motor, and four stands of 8¼-in drill collars for a total length of 123.5 m. The casing running tool was attached to the top of the BHA; the BHA was lowered into and latched to the casing and reentry cone. The reentry cone, BHA, and casing were lowered through the moonpool at 2100 hr.

By 0800 hr on 11 May, we had lowered 4781.8 m of drill string and deployed the vibration-isolated television (VIT) camera in preparation for spudding Hole 1173B. A backup seafloor positioning beacon (Datasonics SN2029; 15.0 kHz; 214 dB) was deployed at 0635 hr. When the VIT camera reached the casing running tool at 1030 hr, we observed that the reentry cone was missing but that the running tool and casing hanger were still attached to the drill string. We began assembling the second reentry cone.

The VIT camera was recovered; we changed the VIT camera drill pipe guide sleeve with the larger casing guide sleeve so that we could lower the camera over the casing to inspect it. At 1515 hr, the camera was lowered over the running tool, and we began inspecting the casing. The entire casing string, bit, and underreamer appeared to be intact. We continued to the seafloor with the drill string and camera to see if we could locate the lost reentry cone. We were unable to locate the reentry cone; the search was abandoned at 1930 hr; we began tripping out of the hole so we could rig up the second reentry cone.

On 12 May, we had raised the drill pipe, secured the casing in the moonpool, removed the casing running tool, racked the drill collars in the derrick, and laid down the mud motor, underreamer, and bit. At this time we had to perform the routine slipping and cutting of the drill line, which was completed at 1100 hr. The casing was taken apart at the first collar, and the second reentry cone was moved into position over the casing collar. The top piece of casing was reattached through the reentry cone; the casing was lowered and latched into the second reentry cone. This time we welded the casing hanger to the reentry cone to prevent it from detaching. We tripped the drilling BHA back into the cas-

ing and latched the running tool; the entire assembly with the second reentry cone was lowered through the moonpool at 1830 hr.

On 13 May at 0445 hr, we experienced a VIT camera problem but continued tripping drill pipe while the camera was changed out. The drill pipe was lowered to 4781.8 meters below rig floor (mbrf), the VIT camera was deployed again at 0600 hr, and we picked up the top drive and spaced out in preparation to spud. Hole 1173B was spudded at 0717 hr. We drilled in the 20-in casing with the underreamer and mud motor to 4926.1 mbrf (124.2 mbsf). With the 20-in casing shoe depth at 4922.5 mbrf (120.6 mbsf), we released the casing running tool at 1110 hr; we started tripping out of the hole with the drill pipe and VIT camera. The bit cleared the seafloor at 1225 hr and the rig floor at 2315 hr.

A summary of Leg 196 Site 1173 operations is presented in Table **T1.** Previous coring operations at Hole 1173A conducted during Leg 190 are reported in Moore, Taira, Klaus, et al. (2001).

Logging while Drilling

As soon as the tools were laid down, we started assembling the LWD/MWD BHA at 0030 hr on 14 May. The Anadrill engineers loaded the radioactive logging sources at 0515 hr. We then picked up the top drive and tested MWD tools at 300 gpm (60 strokes per minute [spm]) and 800-psi standpipe pressure. By 0600 hr we had assembled and tested the 9⅞-in bit, LWD bit sub with float, LWD RAB tool, MWD tool, LWD ISONIC tool, LWD azimuthal neutron and density tool, and the LWD crossover sub. We added five drill collars, a tapered drill collar, and six joints of 5½-in transition drill pipe, for a total length of 139.9 m. We removed the top drive and calibrated the Anadrill drawworks encoder. At 0700 hr on 14 May, we started tripping the drill string down to the seafloor. Unfortunately, we had to stop at 0930 hr (at 1406.8 mbrf) because of an approaching tropical storm (Cimaron). We tripped out of the hole and secured for transit by 1615 hr on 14 May to avoid the approaching storm.

We continued the transit to evade Tropical Storm Cimaron until 0030 hr on 15 May, when the captain felt it was safe to return to the site. The ship arrived back on site at 1100 hr on 15 May. The total transit was 185 nmi and lasted just over 18 hr.

Once we were back on location, the LWD/MWD BHA was assembled, the radioactive sources were loaded, and the tools were tested. We began lowering the LWD/MWD tools to the seafloor at 1330 hr on 15 May. When the drill string reached 3876.1 mbrf, the VIT camera was deployed. However, the camera signal was lost when it reached 102 mbrf. The camera was retrieved, and we found that the camera cable had been damaged in the upper guide horn. Approximately 110 m of cable was cut off, and the cable was reterminated. While this was being done, the drill string was tripped to 4769.6 mbrf. The repaired VIT camera was deployed at 0330 hr on 16 May. While the camera was being lowered to the seafloor, the drill crew assembled extra drill collar stands in preparation for the next site.

The VIT camera reached the top stabilizer/sensor pad on the LWD tool at 0830 hr but could not be lowered past it. The installed VIT guide sleeve (the same one used for the drilling tools) had an internal diameter of 9½ in, and the external diameter of the stabilizer pad was 9⅞ in. The camera was retrieved, the guide sleeve was changed to the casing guide sleeve (internal diameter of 27½ in), and the camera was redeployed at 0830 hr on 16 May. The reentry cone came into view at 1002

hr and was reentered in 1.5 hr. The drill string was lowered into the casing while the VIT was retrieved.

The drill string was spaced out in preparation for drilling and the Anadrill LWD/MWD tools were tested. Drilling/logging operations began at 1500 hr on 16 May at 4922.5 mbrf (120.5 mbsf). The drillers attempted to maintain a 50 m/hr rate of penetration (ROP), as the scientists had requested. The effective ROP was lower than this due to the time required to make pipe connections. The average surface drilling parameters were a weight on bit (WOB) of 4–7 klb at 60 revolutions per minute (rpm), a torque of 150–175 A, and a flow rate of 327 gpm (67 spm) with a standpipe pressure of 1250 psi.

LWD/MWD operations continued until 1545 hr on 17 May, when Hole 1173B reached a total depth of 5539.0 mbrf (737.1 mbsf). The top drive was disconnected from the drill string and racked back in preparation to pull out of the hole. Because of deteriorating hole conditions, however, the top drive had to be reattached to provide rotation and allow circulation. The maximum overpull was 30 klb. The top drive was removed at 5346.6 mbrf. During the trip out of the hole, the LWD tools were recording the entire interval and the speed was controlled at 70 m/hr from 5221.9 to 5171.9 mbrf (420.0–370.0 mbsf) to evaluate LWD ISONIC velocity data quality. The drill bit cleared the seafloor at 2135 hr on 17 May.

Heave Compensation Experiments

Two experiments were conducted during the drilling of the hole to assess the efficacy of the shipboard active heave compensation (AHC) system. We used the MWD tool to measure downhole drilling parameters, including downhole WOB, torque, and bit bounce. These measurements are made using paired strain gauges near the base of the MWD collar, are transmitted to the surface for recording, and are not in downhole memory. Strong MWD pressure signals were recovered at the surface using MWD pulse rates of 3 bits/s at up to 5500 mbrf depth in Hole 1173B. Surface data from the rig instrumentation system (RIS), including surface rotations per minute, torque, WOB, ship heave, pitch, and roll, were recorded synchronously. Sea states up to 2 m and heave to 1.5–2 m were recorded during drilling at Site 1173.

For the first experiment six intervals were drilled with the AHC off (4955.7–4974.7, 5080–5099.3, 5224.2–5243.3, 5387.7–5406.9, 5464.6–5493.9, and 5527–5532 mbrf). During these intervals, drilling proceeded using the passive heave compensation system that was used for most ODP drilling prior to Leg 189. The approximate depths (in mbrf and mbsf), stand length, and times for each AHC-off interval are listed in Table T2. The second experiment consisted of drilling four intervals with the AHC preloaded, which allows the driller to set the surface weight prior to putting the bit in the bottom of the hole (5329–5358, 5406–5435, 5435–5464, and 5522–5527 mbrf). Whether or not this practice is effective in controlling penetration rates is debatable. The approximate depths (in mbrf and mbsf), stand length, and times for each AHC-preloaded interval are listed in Table T3.

Real-time shipboard observations suggest that the AHC damps high-frequency variations in uphole rotations per minute and torque, as well as the high-frequency variation in downhole WOB. The comparison of downhole MWD parameters with the surface information will be analyzed postcruise to evaluate the shipboard heave compensation system and drilling practices.

T2. Heave compensator experiment, AHC-off intervals, p. 85.

T3. Heave compensator experiment, AHC-preloaded intervals, p. 86.

Hole 1173C

Logging while Drilling

Hole 1173C was designed to obtain LWD/MWD logs from the uppermost section that was cased off in Hole 1173B. The ship was offset 50 m to the northwest of Hole 1173B, and Hole 1173C was spudded at 2320 hr on 17 May. The LWD/MWD drilling/logging operations were conducted from the seafloor (4801.9 mbrf) to a total depth of 4976.9 mbrf (175.0 mbsf), which was reached at 0500 hr on 18 May. The ROP was controlled at 60 m/hr, and the effective ROP (including the time required to make pipe connections, etc.) was 30.9 m/hr. The average surface drilling parameters were a WOB of 4 klb at 60 rpm, a torque of 150 A, and a flow rate of 327 gpm (67 spm) with a standpipe pressure of 1250 psi.

The drill string cleared the seafloor at 0650 hr on 18 May; the LWD/MWD BHA reached the rig floor at 1430 hr. The LWD/MWD tools were disassembled, and the drill bit cleared the rotary table at 1655 hr on 18 May. One of the two seafloor positioning beacons was retrieved, and the other was turned off and left on the seafloor for use later in the leg when we would conduct ACORK operations. The drilling equipment was then secured for the transit to the next site.

Return to Site 1173 for ACORK Installation

Following Site 808 LWD/MWD operations and the short port call in Kochi, we returned to Hole 1173B. The Kochi harbor pilot boarded the ship at 0742 hr, and the last line away was at 0800 hr on 29 May. After the pilot departed, we began the transit back to Site 1173 at 0812 hr. After traveling 104 nmi in 9.3 hr, we arrived at Hole 1173B at 1730 hr on 29 May, started lowering the thrusters, and turned the seafloor positioning beacon on.

Our first objective was to reenter Hole 1173B and open the 9⅞-in LWD hole up to 17½ in before installing the ACORK. We began by making up the BHA, which included a 9⅞-in bit sub with float valve, a 17½-in hole opener, crossover subs, and drill collars. At 1910 hr, the ship was in position over Hole 1173B. The bit was lowered to 3534.3 mbrf, where the VIT camera was deployed at 0345 hr on 30 May. The bit was lowered to 4794 mbrf, and we began to search for the reentry cone at 0645 hr. Hole 1173B was reentered at 0832 hr. While we retrieved the VIT camera, the drill string was lowered into the casing to 4926 mbrf (123.5 mbsf).

We then drilled with the hole opener to a total depth of 5537 mbrf (735.1 mbsf). The AHC was turned off because of ship heaves of 2.8–3.3 m while we drilled the interval from 5133 to 5181 mbrf. Twenty-barrel sepiolite mud sweeps were pumped to maintain good hole conditions at 177, 235, 292, 350, 388, 446, 504, 552, 590, 648, and 735 mbsf. The drill string was worked through tight spots at 379–389 and 542–552 mbsf. The average drilling parameters were a WOB of 5–10 klb, top drive rotation of 60 rpm, top drive torque of 200–400 A (maximum of 600 A), and pump pressures of 1350–1800 psi at 120–140 spm.

Before pulling out of the hole, we circulated two 60-bbl sepiolite mud sweeps while the bit was at 735.1 mbsf. The trip out of the hole started at 0800 hr on 1 June. Tight spots at 670, 650, 590, and 495.1 mbsf required rotation and circulation. After the bit cleared the seafloor at 1420 hr on 1 June, from 1515 to 1645 hr, the drill line was slipped and cut. The bit reached the rig floor at 0230 hr on 2 June, the drill collars

were racked back in the derrick, and the bit and hole opener were laid out.

While opening the hole, the moonpool area was prepared for assembling ACORK screens, packers, and casing. A working surface across the moonpool doors was created with I-beams and floor gratings. Tools and supplies were staged in the moonpool area, including the 10¾-in casing centralizers, steel banding, tie wraps, and so forth. The pneumatic umbilical cable reel was set forward of the moonpool area by the drill collar racks; jack stands were welded to I-beams to support the umbilical reel.

The ship was offset ~5 nmi west of Hole 1173B in preparation for assembling the ACORK screens, packers, and 10¾-in casing. From 0230 hr on 2 June to 1730 hr on 3 June, we assembled 54 joints of 10¾-in casing, five screen joints, and four external casing packers. The total length of the ACORK from the casing shoe to the landing joint was 727.77 m, and the weight was ~90 klb. During this operation, the umbilical cable, casing centralizers, and strapping (tie-wraps and banding material) were attached to the casing in the moonpool. A ¼-in outer diameter stainless steel tube was joined between the lowermost screen and packer. Above this the umbilical was hydraulically connected to the bottom and top of each of the screens and packers.

The casing handling equipment was removed from the rig floor by 1800 hr on 4 June. We then moved the ACORK head, ported sub assembly, and 10¾-in casing landing joint from the main deck to the drill floor. After this was attached to the ACORK casing string, the complete assembly was lowered to and hung off the moonpool doors. The casing running tool was released at 2055 hr on 3 June, and we started assembling the drilling BHA. The BHA included a 9⅞-in pilot bit, bit sub with float valve, 17-in underreamer, crossover sub, mud motor, crossover sub, six 8¼-in drill collars, crossover sub, 23 stands of 5½-in drill pipe, one short (5 ft) joint of drill pipe, crossover sub, ACORK stinger, motor-driven core barrel (MDCB) latch sub, and the casing running tool. The total length of the drilling BHA was 737.8 m. Assembly of the drilling BHA was completed at 0500 hr on 4 June.

Once the drilling BHA and ACORK assembly was completed, the final connections of the umbilical to the ACORK head were made. Lowering the ACORK assembly into water in the moonpool purged the air from the stainless steel tubing. From 0800 to 0900 hr on 4 June, the complete assembly was lowered to 1143.3 mbrf. We then deployed the VIT camera to confirm the spacing of the drill bit/underreamer in relation to the bottom of the casing and to verify the proper functioning of the underreamer and mud motor. Once the VIT camera was recovered, the drill string was lowered to 2144.5 mbrf in preparation for the transit back to Hole 1173B. Two 30-ft joints and one 20-ft joint of knobby drill pipe were included at the top of the drill string to provide additional strength to withstand the stress while returning to the site. The transit in dynamic positioning (DP) mode began at 1430 hr on 4 June.

We had begun assembling the ACORK ~5 nmi west of Hole 1173B at 0230 hr on 2 June. Because of the current, we had to allow the ship to drift while we made up the casing. By the time we had finished assembling the ACORK and had lowered it to 2144 mbrf, the ship had drifted 26 nmi east of Hole 1173B at 1430 hr on 4 June. During the transit back to Hole 1173B, we averaged 0.5 nmi/hr and were back on location at 0035 hr on 7 June.

When the drill string had been lowered to 3708.4 mbrf, the VIT camera was deployed. Once the drill string was at 4790.0 mbrf (0630 hr on 7 June), we began the search for Hole 1173B. At 0840 hr, we reentered

Hole 1173B and lowered the drill string to the bottom of the casing. We attached the top drive and began to drill in the ACORK. We continued to observe the operations with the VIT camera until it stopped working at 1320 hr on 7 June. After 35.5 hr of drilling, the ACORK was landed, and we reached the total depth of 732.7 mbsf at 1855 hr on 8 June. The lowermost 86 m drilled very slowly, taking ~19 hr to penetrate. The drilling parameters increased with depth, with drag increasing to 20–40 klb, and pump strokes per minute increasing from 70 to 130 spm as the standpipe pressure increased from 700 to 2800 psi. The WOB was 15–20 klb.

At 1900 hr on 9 June, the go-devil shifting tool was deployed to divert the flow path so we could inflate the packers. An increase in pressure at 2030 hr indicated that the ported sub assembly had been shifted. By 2200 hr, the packers had been inflated and the spool valves shifted.

Our next step was to release the casing running tool so that the drilling BHA could be removed, leaving the ACORK assembly installed. At 2030 hr on 9 June, we attempted to release the casing running tool, but unfortunately, it would not release. At 2200 hr, the VIT camera was deployed to observe the running tool. We maneuvered the ship in a 40-m circle as the drill string was worked up and down with torque to release the running tool. After 7.5 hr, the running tool finally released, and the drilling BHA was raised one joint to confirm this.

After the VIT camera was retrieved by 0715 hr on 9 June, we began assembling the remotely operated vehicle (ROV) platform on the moonpool doors. The deployment bridle and dual acoustic release mechanism were connected to the logging wireline; the entire assembly was lowered into the moonpool at 0915 hr on 9 June. The ROV platform had landed on the ACORK and was released at 1355 hr.

Once the logging wireline had been retrieved, we began tripping the drilling BHA back up to the rig floor. The bit cleared the seafloor and ACORK head at 2125 hr. When the bit was at 908 mbrf (0445 hr on 10 June), a 5-ft drill pipe joint failed at a pin connection, and the entire drilling BHA was lost. This occurred when the failed pin connection was in the lower guide horn one joint below the rig floor. The following equipment was lost: a 9⅞-in bit, six crossover subs, a 17-in underreamer, a mud motor, eight 8¼-in drill collars, 81 joints of 5½-in drill pipe, one 5½-in drill pipe pup joint, an ACORK stinger sub, an MDCB latch sub, the casing/ACORK running tool, one tapered drill collar, and nine joints of 5-in drill pipe.

The next operational step was to drill out below the end of the 10¾-in casing to allow fluid/pressure communication between basement and the deepest ACORK monitoring zone. We decided to use the RCB coring system. Eight drill collars had to be picked up from the drill collar rack, measured, and made up to replace those we had just lost. The top sub and head sub were added, and the RCB core barrel space out was checked. The remaining drill collars that were racked in the derrick were added to the RCB BHA. We started lowering the bit to the seafloor at 0545 hr on 10 June. When the bit was at 3280 mbrf, tripping of the pipe was stopped to allow the drill line to be slipped and cut. We also used this time to replenish the drill pipe available in the racker. Twenty-one joints of 5½-in drill pipe were taken from the riser hold, made into stands, and placed in the pipe racker.

At 1900 hr on 10 June, the upper guide horn was removed, the VIT camera was deployed, and the upper guide horn was reinstalled. At 1945 hr we resumed lowering the drill string to 4780.0 mbrf, where it

was spaced out for reentry. The search for the reentry cone began at 2230 hr. The 30-in-diameter ACORK head was reentered at 2328 hr (see Fig. F34).

Problems arose at 2330 hr when the RCB coring BHA encountered a tight spot in the upper part of the casing. The BHA finally passed through the tight spot at 0145 hr on 11 June. The trip continued to 5327 mbrf, where we began to retrieve the VIT camera; it was back on board at 0515 hr.

The trip continued to 5500 mbrf, where the top drive was picked up. The hole was washed and reamed to 5539 mbrf (737.1 mbsf). The drill string was spaced out, and RCB coring began (Table T4). Drilling Core 196-1173B-1R lasted from 0900 to 1300 hr on 11 June and cored the interval from 5539 mbrf to 5548 mbrf. A problem was identified with the coring wireline and the oil saver sub that required a slip and cut of the wireline. This delayed the retrieval of Core 196-1173B-1R until 1545 hr.

T4. Hole 1173B coring summary, p. 87.

Core 196-1173B-2R took 7.25 hr to cut from 5548.7 mbrf (746.8 mbsf) to 5553.6 mbrf (751.7 mbsf). Slow penetration rates and increased pump pressure suggestive of core jamming led us to pull this core before it had penetrated the full length. The core was on deck at 0030 hr on 12 June. Core 196-1173B-3R was taken from 5553.6 mbrf (751.7 mbsf) to 5558.5 mbrf (756.6 mbsf). Coring operations were stopped at 756 mbsf on 12 June at 0500 hr, as the time allotted for coring had expired. Hole 1173B reached a total depth of 5558.5 mbrf (756.6 mbsf). The top drive was used to pull out from 5558.5 mbrf (756 mbsf) to 5500 mbrf (699 mbsf); the top drive was then racked back, and the trip out of the hole continued. The bit cleared the seafloor at 0745 hr and the rig floor at 1615 hr on 12 June.

The final step in completing the Hole 1173B ACORK was to set a bridge plug at 722 mbsf inside the 10¾-in casing. The bridge plug (Weatherford model 53PBP.1001; 10¾-in, 40.5-lb/ft mechanical set cast-iron bridge plug) and 10¾-in mechanical setting tool (model 53MST.1002 with a crossover to 4½-in American Petroleum Institute regular threads) were assembled to two drill collars, one tapered drill collar, and six joints of 5½-in drill pipe. This bridge plug BHA was lowered to 3275 mbrf, where the VIT camera was deployed. The drill pipe was lowered to 4778 mbrf, where the top drive was picked up for drill string space out and reentry. The search for the reentry cone began at 0415 hr on 13 June. The 30-in-diameter ACORK head was reentered at 0610 hr.

The bridge plug was run in the hole to 5268 mbrf (466.3 mbsf). The VIT was retrieved at 0900 hr. The trip continued to 5498 mbrf (696 mbsf). The top drive was picked up, and the drill string was spaced out to set the bridge plug at 722 mbsf. The bridge plug requires 10 revolutions of right-hand rotation to set the upper slips. When right-hand rotation was applied to the drill string, the torque built to ~600 A in only eight revolutions. Numerous unsuccessful attempts were made from 1030 to 1200 hr to achieve the required 10 revolutions. While holding torque in the string, the crew worked the string up and down 15 m with no drag or overpull.

We then started pulling the pipe up the hole while trying to set the bridge plug at every stand; it was a wet trip. When the bridge plug reached 466.3 mbsf and the connection was made, the drill pipe at the rig floor had no water in it. Immediately upon pulling up on the next stand, overpull was observed, and then the sequence of actions to set the packer was initiated. Forty thousand pounds of overpull was held for 5 min to set the packer. Then 5 klb of weight was set down on the

packer. A second overpull of 40 klb was applied and then bled off to neutral weight. The drill string was rotated to the right to release the running tool from the bridge plug. The torque climbed to 250 A with three rotations and then fell to 150 A, indicating that the bridge plug was set.

The drill string was then raised to 437 mbsf. After removing the top drive, tripping operations continued. The driller observed that the drill string weight appeared to be ~30 klb too low. The trip continued until the bottom of the pipe should have been at 471.0 mbrf when a failed 5-ft drill pipe joint cleared the rotary table at 2400 hr. Five joints of 5-in drill pipe were removed from service: four had been bent and one had parted in the tube body. The following equipment was lost: a bridge plug running tool, a bit sub, two 8¼-in drill collars, one tapered drill collar, six joints of 5½-in drill pipe, three crossover subs, and 40 joints of 5-in drill pipe. The 41st joint of drill pipe above the BHA parted as a result of compression bending ~8.4 m from the tool joint shoulder. Analysis of the drilling data suggests that the bridge plug had set at 466 mbsf. The 471-m length of lost equipment suggests that the parted drill pipe is at the top of the ACORK head assembly. Since the bridge plug had set, we determined there was nothing more that could be done at Hole 1173B and began the transit to Hole 808I at 0000 hr on 14 June. We were unable to recover the seafloor positioning beacon once it reached the surface.

After finishing operations at Site 808, we returned to Hole 1173B to conduct a camera survey of the Hole 1173B ACORK. After a 9.25-hr DP transit, the ship arrived at Hole 1173B at 0420 hr on 29 June. The drill string was lowered to 4795 mbrf, and the seafloor search for the reentry cone and ACORK began at 0600 hr. The reentry cone was located at 0618 hr and was observed until 0630 hr (see Fig. **F35**). The parted end of the drill pipe was inside the ACORK minicone and did not appear to stick out above it. Other than the fact that the inner bore of the ACORK is unusable, the Hole 1173B ACORK installation appeared to be intact. We began recovering the drill string and the VIT camera at 0630 hr on 29 June. The VIT camera was retrieved at 1200 hr. When the bit cleared the rig floor (2215 hr), we observed that the underreamer arms had broken off the underreamer that was used at Site 808. This may have been one of the problems contributing to our inability to penetrate to the total depth while installing the ACORK in Hole 808I. The BHA containing the underreamer used to install the ACORK in Hole 1173B was lost after installation as described above. It is conceivable that similar problems with those underreamers contributed to the difficulties in completing the final 100 m of ACORK penetration in Hole 1173B. The transit to Yokohama began at 2215 hr. Leg 196 ended with the first line ashore at 0830 hr on 1 July 2001 in Yokohama.

QUALITY OF LWD LOGS

Figures **F4** and **F5** show the quality control logs for Holes 1173B and 1173C. Target ROPs of 50 m/hr in the interval 120–350 mbsf, 35 m/hr in the interval 350–450 mbsf, and 50 m/hr in the interval 450 mbsf to total depth (TD) were chosen in Hole 1173B. A target ROP of 60 m/hr was chosen in Hole 1173C. To record one sample per 15 cm, the ROP must be maintained at 65 m/hr or lower. This was achieved for 96% of the total section in Hole 1173B and 76% of the total section in Hole 1173C (Figs. **F4, F5**). Although RAB image resolution would improve

F4. Quality-control logs, Hole 1173B, p. 42.

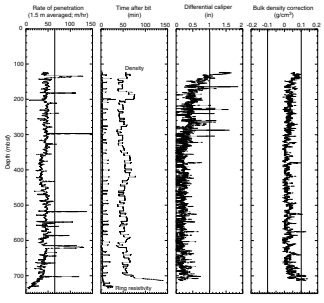

F5. Quality-control logs, Hole 1173C, p. 43.

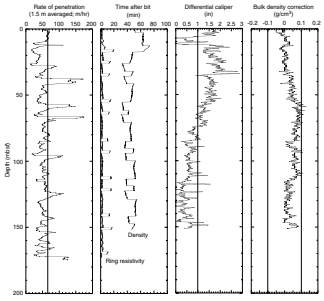

with even slower drilling rates, the quality of RAB images is high (~3-cm pixel) and no significant resolution loss is observed between the higher and lower ROP intervals in Hole 1173B.

The differential caliper (DCAL) is the best indicator of borehole conditions. The bulk density correction (DRHO), calculated from the difference between the short- and long-spaced density measurements, varies from 0 to 0.1 g/cm³ (Figs. F4, F5), which shows the good quality of the density measurements in Holes 1173B and 1173C. A standoff of <1 in between the tool and borehole wall indicates high-quality density measurements with an accuracy of ±0.015 g/cm³. The differential caliper values are <1 in over 98% of the total section in Hole 1173B. Only the uppermost 20 m of the hole and several small intervals through the section show minor washouts. The differential caliper values are <1 in over 52% of the total section in Hole 1173C (Fig. F5). The uppermost 75 m was washed out to 1–2 in because of soft sediments, and the bulk density measurements in this interval are not accurate.

Time-after-bit (TAB) measurements are 10–20 min for resistivity and gamma ray logs and 30–70 min for density and neutron porosity logs. TAB values as long as 140 min from 710 mbsf to TD coincide with low ROP while drilling in basement rocks. However, the low values of the DCAL and DRHO logs indicate that the borehole condition was not significantly deteriorated in this interval.

ISONIC Data Processing and Data Quality

Preliminary waveform processing and evaluation were carried out by Anadrill-Schlumberger in Houston, Texas, during and immediately after Leg 196. Raw waveforms from the four receivers of the ISONIC tool are shown for two depths (262.15 and 397.58 mbsf) in Figure F6. They show, in order of arrival, drilling "noise" phases and a dispersive wavetrain of a leaky *P*-wave mode traveling in the borehole and along the formation/borehole wall interface.

The formation *P*-wave velocity may be estimated from the leaky mode wavetrain; at the two depths, the arrival of the leaky mode changes. The contour plots of coherence vs. slowness and time show peaks corresponding to the leaky *P*-wave arrivals. For the shallow depth (Fig. F6C) the coherence shows a single broad peak at a slowness of 180–190 µs/ft (velocity of 1604–1693 m/s), where it may be difficult to extract the *P*-wave velocity because of the frequency and slowness of these phases in Holes 1173B and 1173C. For the deeper depth (Fig. F6D), arrivals are more clearly separated, with the earliest one corresponding to a coherence peak at a slowness of ~160 µs/ft (velocity of 1905 m/s). Such separation may improve subsequent analyses by bandpass and wavenumber domain filtering. Processing of the ISONIC waveforms will be conducted postcruise to attempt to extract the *P*-wave velocity. Preliminary velocity values (Fig. F32) are probably largely unreliable and should be used with a great deal of caution (see "Logs and Physical Properties," p. 23).

Hole-to-Hole Correlation

Figure F7 shows a correlation diagram for the overlapping interval between Holes 1173B and 1173C, using the ring and deep resistivity logs. The curves have similar shapes, including three significant peaks that can be correlated between 120 and 175 mbsf. Peak A at 135.25 mbsf, Peak B at 147.59 mbsf, and Peak C at 164.82 mbsf in Hole 1173B

F6. ISONIC waveforms and plots of coherence against slowness and time, p. 44.

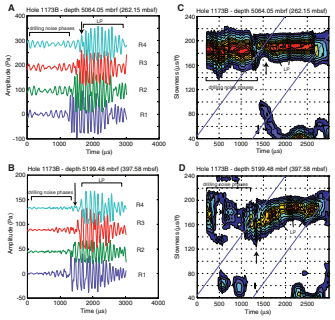

F7. Resistivity correlation for Holes 1173B and 1173C, p. 45.

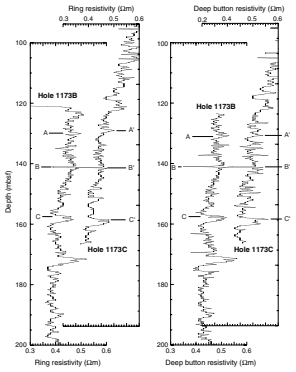

correlate to Peak A′ at 130.07 mbsf, Peak B′ at 141.04 mbsf, and Peak C′ at 157.50 mbsf in Hole 1173C, respectively. This suggests Hole 1173C is ~7 m deeper and ~2 m longer than the equivalent section in Hole 1173B. The depth measurement of Hole 1173B is reliable with <0.5 m uncertainty as indicated by the physical depth of the casing pipe (120.9 mbsf) being close to the measured depth of the casing shoe (120.6 mbsf) and the close correlation of the wireline log depth recorded in Hole 1173A with the LWD logs in Hole 1173B. Possible reasons for the depth shift in Hole 1173C include (1) hole deviation, (2) poor drilling control in shallow soft sediment, and (3) depth errors in identifying the seafloor in Hole 1173C.

Construction of Composite Logs

Based on the correlation of the overlapping interval between Holes 1173B and 1173C, a composite log is generated using the following method:

1. Because the depth recorded in Hole 1173B is reliable, the logs in Hole 1173C are depth shifted and spliced to the logs in Hole 1173B.
2. For bulk density and neutron logs the section below Peak B in Hole 1173B is used in its entirety. In Hole 1173C, these logs are not recorded below Peak B′.
3. In Hole 1173C, the logs from the seafloor to Peak B′ are compressed proportionally to 95.6% of their original depth and spliced in the section from the seafloor to Peak B in Hole 1173B.

DEFINITION OF LOG UNITS AND LITHOLOGIC INTERPRETATION

For the following descriptions of LWD data, Hole 1173C was used for the upper 150 m and Hole 1173B for below 150 mbsf.

Definition of Log Units

An overview of log data with log units is shown in Figure **F8.** Five first-order log units and two second-order units were defined through a combination of visual interpretation and multivariate statistical analysis (see **"Identification of Log Units,"** p. 9, in the "Explanatory Notes" chapter). For the multivariate statistical analysis, factor logs were calculated from gamma ray, photoelectric effect, bulk density, ring resistivity, differential caliper, and neutron porosity logs. The *P*-wave velocity LWD log was not used because of the delay in processing it. The first two factor logs account for 76% of the total variance in the selected data. Cluster analysis of these two factor logs identified four clusters, each with a specific and distinct set of log properties. The distribution of log units is shown in Figure **F9,** together with the log units and LWD gamma ray, density, and resistivity curves. Mean and standard deviation values of the log properties for each log unit are summarized in Table **T5** and graphically shown in Figure **F10.** Additionally, a good overall differentiation of the five log units according to their physical properties can be observed in the crossplots (Fig. **F11**).

F8. Visual interpretation of log units, p. 46.

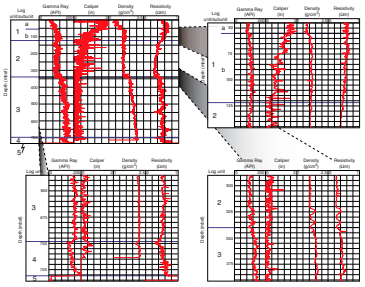

F9. Definition of log units based on statistical analysis, p. 47.

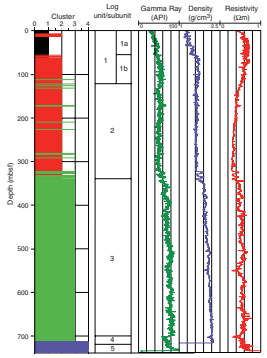

T5. Log unit properties, p. 88.

F10. Statistical data for each log unit, p. 48.

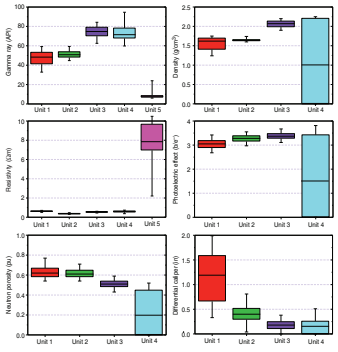

F11. Crossplot of log properties, p. 49

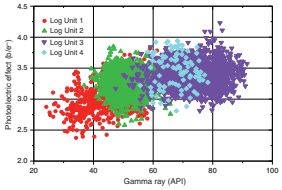

Log Unit 1 (0–122 mbsf) shows a high mean value of neutron porosity (0.63 porosity units [pu]), a low mean value of density (1.55 g/cm³), and a relatively high standard deviation of density (0.176 g/cm³) (Fig. F10; Table T5). A high variability in the differential caliper log (standard deviation of 0.55 in) and a large number of values >1 in, which reflect bad borehole conditions, characterize log Unit 1. Log Unit 1 is subdivided into Subunits 1a and 1b. Log Subunit 1a is characterized by high variability in resistivity (Fig. F8). The base of Subunit 1a (0–55 mbsf) has a positive shift in gamma ray (from 35 to 65 API), density (from 1.5 to 1.7 g/cm³), and resistivity (from 0.5 to 0.7 Ωm). The base of log Subunit 1b (55–122 mbsf) is defined by an abrupt decrease in gamma ray (from 60 to 45 API), density (from 1.75 to 1.65 g/cm³), and resistivity (from 0.54 to 0.46 Ωm) values.

Log Unit 2 (122–340 mbsf) is identified by a decrease in resistivity of 0.3 Ωm, in density of 0.1 g/cm³, and in gamma ray of 10 API with depth. The decrease in resistivity and density reflects an abnormal compaction trend. The base of log Unit 2 is clearly marked by a positive shift in the mean values of resistivity (from 0.37 to 0.53 Ωm), density (from 1.65 to 2.06 g/cm³), neutron porosity (from 0.62 to 0.51 pu), and gamma ray (from 51.27 to 74.32 API) (Table T5).

Log Unit 3 (340–698 mbsf) is characterized by high mean values of gamma ray (74.32 API), density (2.06 g/cm³), and photoelectric effect (3.38 b/e⁻). Density and gamma ray values increase continuously with depth (from 1.6 to 2.2 g/cm³ and from 60 to 90 API). Log Unit 3 also has a significant cyclicity in resistivity. The base of this log unit is defined by an abrupt decrease in gamma ray (by 30 API), density (by 0.15 g/cm³), resistivity (by 0.2 Ωm), and photoelectric effect (by 0.6 b/e⁻).

Log Unit 4 (698–731 mbsf) is characterized by a high variation of values that is reflected in its high standard deviation values (Table T5). The mean values of neutron porosity (0.20 pu), density (1.03 g/cm³), and photoelectric effect (1.62 b/e⁻) are very low.

The top of log Unit 5 (731–735 mbsf) is characterized by an abrupt increase in resistivity (from 2.5 to 11 Ωm) and a decrease in gamma ray (from 100 to 10 API), the only logs that are available for this depth.

Logs and Lithology

Holes 1173B and 1173C are located ~52 and ~98 m, respectively, from Hole 1173A, which is sufficiently close to correlate the logged sections with recovered sediments. Lithologies based on core descriptions from Hole 1173A are summarized below, along with bulk mineralogy from shipboard X-ray diffraction (XRD) analyses. A detailed description of the sedimentary units, depositional environments, and core photographs are given in the Leg 190 *Initial Reports* volume (Moore, Taira, Klaus, et al., 2001).

Sediments from Hole 1173A were divided into five lithologic units. Unit I is characterized by sandy and silty turbidites. Units II and III are composed of hemipelagic silty clay/claystone with and without volcanic ash layers, respectively. Units IV and V consist of volcaniclastics and basalt. Sedimentation rates based on biostratigraphic age assignments indicate high accumulation rates for Units I and II and low accumulation rates for Units III and IV.

Lithologic Unit I (0–102 mbsf)

Lithologic Unit I comprises Quaternary sandy to muddy turbidites of the outer Nankai trench–wedge facies. Unit I is divided into two subunits. Subunit IA (outer trench–wedge facies) consists of 83.37 m of silty clay interbedded with silt, sandy silt, silty sand, and rare beds of volcanic ash. The dominant lithology is greenish gray silty clay to clayey silt. Hemipelagic settling and fine-grained (muddy) turbidity currents probably deposited the silty clay to clayey silt of Subunit IA.

The base of Subunit IB (trench–basin transition facies) is defined by the deepest occurrence of medium-bedded silty sand. The top of this subunit is defined by the uppermost interval containing multiple ash layers. Subunit IB is 18.77 m thick and contains silty clay with scattered interbeds of silt- to clay-sized volcanic ash and rare volcanic lapilli. Subunit IB is stratigraphically transitional between upper Shikoku Basin and outer trench–wedge sediments.

Lithologic Unit II (102–344 mbsf)

The transition to lithologic Unit II is marked by the deepest occurrence of turbidites. The silty claystone of Unit II appears to be finer grained than equivalent lithologies of Unit I and contains fewer siliceous microfossils.

Unit II is Pliocene to Quaternary in age and consists of hemipelagic mud with abundant interbeds of volcanic ash probably derived from the Kyushu and/or Honshu volcanic arcs (upper Shikoku Basin facies). The most common lithology ranges in texture from silty clay to clayey silt and changes with increasing compaction to silty claystone and clayey siltstone. Interbeds of volcanic ash and tuff are common. The deepest unequivocal ash bed defines the base of Unit II (343.77 mbsf). Unit II represents the upper part of the Shikoku Basin succession.

Lithologic Unit III (344–688 mbsf)

The Unit II/III boundary is controlled by the last ash bed and, in part, by silica diagenesis. There is an abrupt loss of unequivocal ash beds and replacement by siliceous claystone, most of which may be altered tephra beds.

Bioturbated silty claystone and a minor amount of calcareous and siliceous claystone characterize lithologic Unit III. Unit III is of Pliocene to middle Miocene age (lower Shikoku Basin facies). The dominant lithology of silty claystone in Unit III is gray to greenish gray with local faint laminae.

Lithologic Unit IV (688–725 mbsf)

The sediments consist of variegated siliceous claystone and silty claystone (volcaniclastic facies). The probable sediment age is middle Miocene. The silty claystone of Unit IV is probably a hemipelagic deposit, whereas the light gray siliceous intervals appear to be altered volcaniclastic deposits.

Lithologic Unit V (725 mbsf)

Lithologic Unit V consists of a single piece of middle Miocene (13–15 Ma) basalt. It is unclear whether or not this fragment was part of a basaltic breccia or lava flow.

Bulk Mineralogy

The trends observed in the bulk mineralogy column of Figure F12 can generally be related to the changing influence of hemipelagic sedimentation vs. lateral influxes of terrigenous and calcareous sediment, with intermittent deposition of volcanic ash layers. The percentage of total clay minerals varies between 40% and 50% in the upper 330 m. Below 330 mbsf, the percentage of total clay increases to 45%–60%. The increase in clay content corresponds to the log Unit 2/3 transition.

The calcite content varies significantly. The intervals 0–125 and 360–615 mbsf are characterized by low calcite content (0%–5%). The intervals 125–360 and 515–680 mbsf have higher calcite contents of up to 25% and 70%, respectively. Even the carbonate-rich intervals are interbedded with noncalcareous claystone layers. The plagioclase content decreases continuously with depth from 15%–20% at the top to 5%–10% at the bottom.

The high quartz content reflects the influence of terrigenous silts and sands. Below 570 mbsf the quartz content varies between 15% and 40%. Most samples contain ~35% quartz.

Correlation with Log Units

Log Unit 1 (0–122 mbsf) does not exactly coincide with lithologic Unit I (0–102 mbsf), which comprises Quaternary sandy to muddy turbidites of the outer trench–wedge facies (Fig. F12). Thus, log Subunit 1a (0–55 mbsf) correlates with the upper part of lithologic Subunit IA (0–83 mbsf), which consists of silty clay with interbedded coarser sediments such as silt, sandy silt, and volcanic ash. The spiky variability in gamma ray, density, resistivity, and photoelectric effect logs in log Subunit 1a is attributed, at least in part, to borehole washouts. Given the presence of less cohesive lithologies in the vicinity of washouts and absence of change in drilling parameters, it seems likely that the enlargement might be lithologically influenced. The difference between log and lithologic unit boundaries might be explained by high values of differential caliper that influence the log quality (e.g., gamma ray and density) significantly. A marked increase in the photoelectric effect log at the bottom of log Subunit 1b (55–122 mbsf) correlates with an abrupt increase in carbonate content. But there is no decrease in the observed gamma ray as expected for calcareous-rich sediment. Additionally, there is no evidence in the logs (such as resistivity peaks) of high ash content in the cores that define lithologic Unit I.

Log Unit 2 (122–340 mbsf), reflecting the upper Shikoku Basin facies, is characterized by low values in the density, resistivity, and gamma ray logs. This log unit correlates with lithologic Unit II (102–344 mbsf), which consists of hemipelagic mud (silty clay to clayey silt) with abundant interbeds of volcanic ash. The high neutron porosity and low resistivity logs indicate a high and uniform porosity. The low density could be related to a cementation effect caused by the formation of cristobalite.

Log Unit 3 (340–698 mbsf) correlates with lithologic Unit III (344–688 mbsf), the lower Shikoku Basin facies, and includes the upper part of lithologic Unit IV (688–725 mbsf). Log Unit 3 is characterized by a normal compaction trend where density and resistivity logs increase continuously with depth. Also, resistivity and, less obviously, gamma ray logs show a characteristic cyclicity of values that may reflect

F12. Summary of Site 1173 log and lithologic data, p. 50.

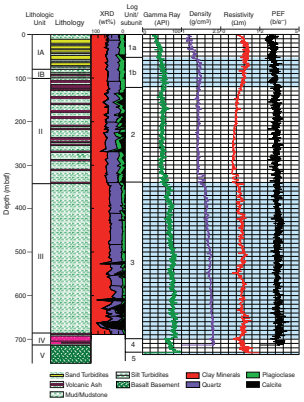

changes in lithology, which may in turn reflect an interbedding of coarser and finer grained sediments (e.g., silty clay and clayey silt).

Log Unit 4 (698–735 mbsf) is characterized by broad variations in photoelectric effect, resistivity, neutron porosity, and gamma ray logs that correlate well with the presence of the volcaniclastic facies (see "Log Interpretation," p. 21). The difference in depth of the volcaniclastic facies might be caused by low core recovery (~12%).

Log Unit 5 (731–735 mbsf) can be correlated with lithologic Unit V (725–735 mbsf), although the upper boundary is significantly lower. Lithologic Unit V consists of middle Miocene basalt. Low gamma ray (10 API) and high resistivity (10 Ωm) values differ significantly from the units above and characterize Log Unit 5. The very low core recovery (~3%) and the poor definition of the top of the lithologic unit (based on a single small piece of basalt) might explain the depth difference of basement between log and lithologic units.

Lithology and Log Comparison

The crossplot of gamma ray vs. photoelectric effect reflects changes in lithology based on log units (Fig. F11). These two logs were used because of lesser sensitivity to sediment compaction than the density and resistivity logs. Overall a positive correlation between gamma ray and photoelectric effect is observed. From log Unit 1 to Unit 3 a continuous increase in gamma ray and photoelectric effect is observed. This may reflect an increase in clay and calcareous content. The data of log Units 2 and 3 overlap significantly, because of the similarity of the sediment composition (silty clay and clayey silt). This observation of higher clay content and lower content of sand and silt fits quite well with lithologic descriptions. Log Unit 4 (volcaniclastic facies) is an exception, because gamma ray and photoelectric effect values overlap with log Units 2 and 3. This might be caused by its lithologic composition, a mixture of siliceous claystone, silty claystone, and sand.

Lithology and RAB Images

Resistivity variations between lithologic units are well illustrated by 360° RAB images, which can be displayed as "unwrapped" planar images with Schlumberger's Geoframe software. Figure F13 illustrates contrasts between the resistivity images of the thinly bedded, sandy to muddy turbidites of lithologic Unit I and log Unit 1 (trench-wedge facies) and the hemipelagic mud with interbedded volcanic ash layers of lithologic Unit II and log Unit 2 (upper Shikoku Basin facies). Figure F13A shows conductive (dark color in RAB image) probable coarser grained basal turbidite layers overlain by resistive (light color) probable finer grained sediments. Average turbidite bed thicknesses are 20–80 cm and are dominated by high-resistivity sediments (interpreted to be finer grained clays and silts). The resolution of the RAB images does not allow the identification of grading patterns or erosive vs. gradational boundaries. Average resistivity decreases in lithologic Unit II and log Unit 2 and contains highly resistive thin interbeds (Fig. F13C), which correlate with ash beds interpreted from Hole 1173A cores and Formation MicroScanner (FMS) images. This unit is characterized by more homogeneous RAB images compared with the well-stratified turbidites of lithologic Unit I and log Unit 1. Resistive (dark color) spots, corresponding with poorly stratified sections, are more common (Fig. F13B) and

F13. RAB images of different units, p. 51.

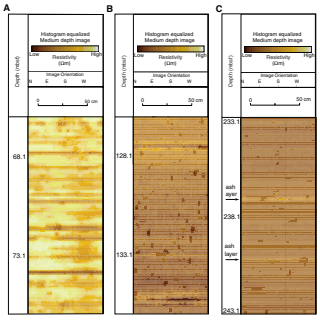

are inferred to represent bioturbation-related reduction spots (based on a correlation with Hole 1173A core data).

Log Interpretation

Turbidite Zone

The trench-wedge zone (log Unit 1; 0–122 mbsf) consists of silty and sandy turbidites in the uppermost 100 m (Moore, Taira, Klaus, et al., 2001) (Fig. F14). The upper 75 m is characterized by >1 in caving of the borehole, which makes further log interpretation difficult. Below 75 m the caliper values stabilize, and so do the gamma ray, resistivity, and density logs, which show values that are typical for a clayey siltstone.

On the density log on Figure F14, several log trends have been marked with small arrows that show fining-upward trends, which are typical in turbidite zones (Rider, 1996). The same trends are seen in the resistivity log. On the other hand, the gamma ray log shows opposite trends in the intervals 20–35 and 55–90 mbsf. The explanation for this is bad borehole conditions, which are seen in the differential caliper values and the RAB image logs.

F14. Logs and RAB image of a turbidite section, p. 52.

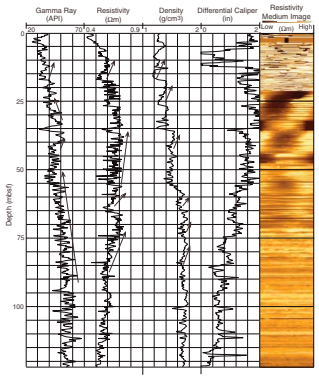

Unit 2–3 Transition Zone

The transition zone comprises the log boundary between log Units 2 and 3 (340 mbsf) and the lithologic boundary between lithologic Units II (upper Shikoku Basin facies) and III (lower Shikoku Basin facies) (Fig. F15). Lithologic Unit II ranges in texture from silty clay/claystone to clayey silt/siltstone. Interbeds of volcanic ash and tuff are common (Moore, Taira, Klaus, et al., 2001). The section between 310 and 322 mbsf is interpreted as a clayey siltstone on the basis of low gamma ray (~50 API) and resistivity (~0.3 Ωm) values. The transition zone is placed in the section between 322 and 340 mbsf on the basis of two high density and resistivity peaks at 324–327 and 333–337 mbsf. The log Unit 2/3 boundary is defined at the base of this transition zone where gamma ray, resistivity, and density logs show low values.

The lithologic Unit II/III boundary is located at the base of the deepest unequivocal ash bed (~344 mbsf). This ash layer is clearly indicated by the low gamma ray (50 API) and density (2.0 g/cm³) values and the high resistivity (0.6 Ωm) values. This is confirmed by the RAB image log as a thin band with very low resistivity.

F15. Logs and RAB image of the log Unit 2–3 transition, p. 53.

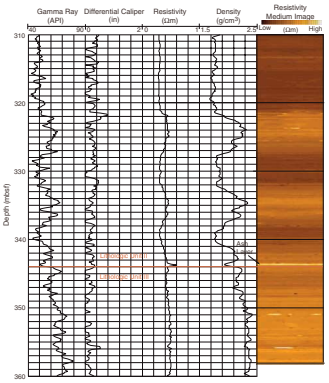

Volcaniclastic Facies

LWD measurements were made in the depth interval between 680 and 735 mbsf, where the core recovery of Hole 1173A is very low (~12%) (Fig. F16). The volcaniclastic facies (lithologic Unit IV; 688–725 mbsf) consists of variegated siliceous claystone and silty claystone, calcareous claystone, and sand. Between 698 and 702 mbsf the logs are characterized by significantly low gamma ray (<70 API), photoelectric effect (<3 b/e⁻), resistivity (<0.4 Ωm), and density (<2.1 g/cm³). This layer may be coarser grained material such as sand and is recognized in the RAB images by its dark color that reflects low resistivity. Between 702 and 708 mbsf gamma ray is still characterized by low values (<70 API), but resistivity (0.4–0.6 Ωm), density (>2.2 g/cm³), and photoelectric effect (>3.5 b/e⁻) values are much higher. This may be a carbonate-cemented, highly compacted sandy material.

F16. Logs and RAB image of the volcaniclastic facies section, p. 54.

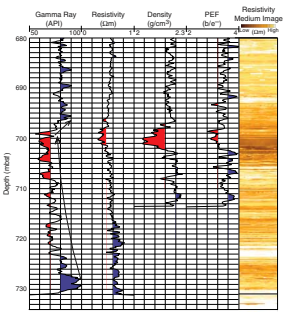

LOGS AND STRUCTURAL GEOLOGY

Structural data were determined from RAB images using Schlumberger's Geoframe software (see "Interpreting Structure from RAB Images," p. 9, in the "Explanatory Notes" chapter). All structural interpretations were made using RAB images of medium-focused button resistivity, which images at a penetration depth of 3 in (7.6 cm). Data were taken from Hole 1173B for the overlapping region of Holes 1173B and 1173C.

Deformation is sparse at Site 1173, as was observed in the cores and wireline data of Hole 1173A (Shipboard Scientific Party, 2001). Apparent bedding dips are low throughout the hole and range from ~0° to 35°, with the majority <~5° (Fig. F17). Based on calculations of maximum resolution of RAB data and hole width, minimum resolvable dip is ~4°–7°. Bedding dips exceeding ~5° occur at 50–200, 280–560, and 600–720 mbsf (above basaltic basement). Bedding dip is subhorizontal between these regions (200–280 and 560–600 mbsf). An increase in average bedding dips is observed below ~370 mbsf, but subhorizontal bedding is still common below this depth (Fig. F17). An abrupt increase in bedding dip was observed at the same depth in cores from Leg 190 Hole 1173A (Shipboard Scientific Party, 2001). Direct comparison of Leg 190 and 196 data (Fig. F17) suggests greater bedding dips for the former. However, if dips <5° (approximate minimum resolvable dip for both Leg 190 core data and Leg 196 RAB image data) are removed and the remaining data are replotted, moving averages are very similar. The apparent discrepancy is therefore thought to be a result of the sampling and recording methods of these two types of subhorizontal data. The nonsystematic variability of bedding dips with depth at Holes 1173B and 1173C may reflect a slump rather than tectonic origin.

Fractures (including faults) are rare but fairly evenly distributed throughout Holes 1173B and 1173C (Fig. F18). Fracturing was identified between 80 and 200 mbsf, 320 and 570 mbsf, and 660 and 700 mbsf, with the majority of deformation concentrated between 380 and 520 mbsf. This zone correlates with increases in bedding dip (Fig. F17). Specific concentrations of fractures within this interval occur at 378–384 and 410–417 mbsf. Fracture dip is high (40°–80°), with the majority dipping 50°–70°. This is inconsistent with low-angle thrust faulting as observed within the accretionary wedge (not expected at the reference site seaward of the deformation front), but consistent with normal or reverse faulting. Where offset of stratigraphic markers was observed in the RAB images, displacement was normal (e.g., Fig. F19) and of the order of 10–20 cm. Conjugate faults are observed locally. Fracture strike shows random orientation (Figs. F18, F20). A second example of a high-angle fault cutting a high-resistivity ash layer is shown in Figure F19B. Fractures are both resistive and conductive with nonsystematic variation with depth in the hole. Resistive fractures dominate and many fractures show a change from high to low resistivity along the fault plane (across the RAB image). High conductivity would suggest open fractures with high porosity whereas high resistivity might reflect nonconductive clay gouge, mineralization, or porosity collapse due to compaction. However, mineralization and veins were rare in cores recovered from Hole 1173A (Shipboard Scientific Party, 2001) with a few exceptions in lower cores (~600 mbsf). High-angle fractures (68°–73°; south trending) are also observed within the basaltic basement at ~730 mbsf.

F17. Comparison of bedding dips from RAB and core data, p. 55.

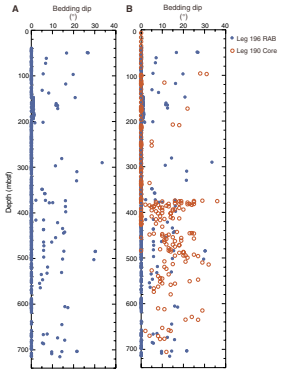

F18. Fracture dip and strike, p. 56.

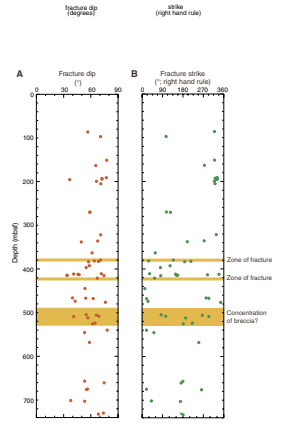

F19. RAB images of fractures, p. 57.

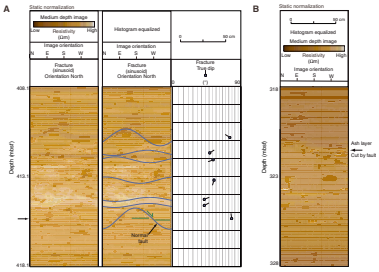

F20. Stereographic plot of poles to fault planes, p. 58.

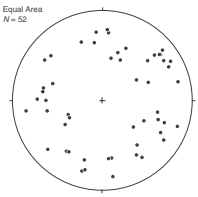

These fractures cut a highly conductive near-vertical feature, which is interpreted as a borehole breakout induced by drilling (Fig. F21).

At 500 mbsf, bands of increased and heterogeneous ("mottled") resistivity are observed, with poorly defined bedding. More fractures are observed within these zones but identifying individual planar fractures is hindered by the heterogeneity of resistivity within the RAB image. These zones may indicate brecciation, intensive fracturing filled with high-resistivity sediments, or partial porosity collapse due to compaction. Sediment-filled fractures were noted at this depth in Hole 1173A (Shipboard Scientific Party, 2001).

In general, structural data from RAB images at Holes 1173B and 1173C show good correspondence with seismic data (i.e., where visible in data, subhorizontal bedding from ~0 to 300 mbsf followed by increased stratigraphic dip below this level). Deformation at Site 1173 (including high-angle faulting, conjugate faults, random orientation, and normal displacement) is consistent with a model of extensional faulting related to compaction and burial. Extensional faulting is also observed in seismic sections crossing Site 1173 (Figs. F3, F4). Extensional deformation may also be related to basement structures (ridge related) or flexure of the incoming subducting plate.

F21. RAB image of basaltic basement, p. 59.

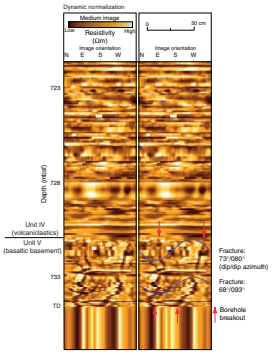

LOGS AND PHYSICAL PROPERTIES

Density

The LWD density (RHOB) log shows a good fit to the core bulk density (Fig. F22), generally overpredicting the core values by as much as ~0.1 g/cm³. The density log (Fig. F22) shows a large deviation from core values between 0 and 55 mbsf corresponding to the zone of poor LWD data quality (see "Quality of LWD Logs," p. 14). Below 55 mbsf the density log shows two overall trends, near constant density from 55 to 321 mbsf and a gradual increase in density from 321 to 713.46 mbsf. In detail (Table T6) density is nearly constant at an average of 1.69 g/cm³ from 55 to 122 mbsf (log Subunit 1b), decreasing to ~1.64 g/cm³ at 130 mbsf. Density shows only a small deviation of ±0.06 around a mean of 1.64 g/cm³ from 130 to 321 mbsf. The interval from 321 to 340 mbsf exhibits large-amplitude fluctuations in density, with oscillation between two peak values of 1.64 and 1.9 g/cm³, associated with the transition from upper to lower Shikoku Basin facies. Density increases steadily from 1.84 g/cm³ at 340 mbsf to 2.05 g/cm³ at 468 mbsf, below which there is a step decrease to 1.99 g/cm³. Density increases rapidly to 2.15 g/cm³ at 503 mbsf and decreases to 2.06 g/cm³ at 558 mbsf. Following a step increase to 2.11 g/cm³ at 565 mbsf, density increases less steeply than between 340 and 468 mbsf to 2.2 g/cm³ at 698 mbsf, where a large negative peak marks the transition from the base of the lower Shikoku Basin facies to the underlying volcaniclastic sequence, in which the density log terminates.

F22. Comparison of LWD and core densities, p. 60.

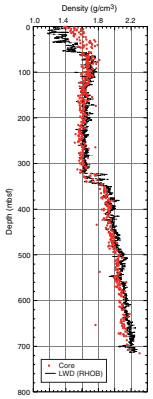

T6. LWD density trends with depth, p. 89.

F23. Least-squares fits of core grain densities, p. 61.

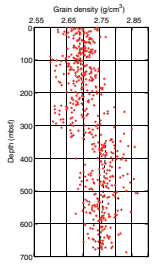

Porosity Calculations from LWD Density Logs

Core grain density measurements from Hole 1173A (Fig. F23) indicate changes with depth associated with lithologic variations. The grain density data were used to calibrate a density to porosity transform for the LWD density logs. Although small-scale trends are observed in the grain density with depth, the data follow two general trends divided by

an abrupt change in grain and bulk density corresponding to the transition from upper to lower Shikoku Basin facies at ~344 mbsf. Least-squares regression, after manual removal of low and high density spikes (Fig. F23), was used to evaluate these trends in grain density (ρ_g). For 0 to 344 mbsf,

$$\rho_g = 2.6882 + (4.7753 \times 10^{-5} \times z),$$

and for 344 to 687 mbsf,

$$\rho_g = 2.7901 + (5.5909 \times 10^{-5} \times z),$$

where z is the depth in meters.

Porosity (ϕ) was calculated from the LWD density log

$$\phi = (\rho_b - \rho_g)/(\rho_w - \rho_g),$$

where ρ_b is the log value (bulk density), and assuming a water density (ρ_w) of 1.035 g/cm³. This porosity (Fig. F24) shows an overall improved fit to core porosity data between 60 and 687 mbsf compared to the use of constant grain densities, with the LWD porosity underpredicting the core data by ~0.02 g/cm³ below 340 mbsf. Porosity is quite well predicted in the interval 315–344 mbsf, which corresponds to a region of high-amplitude variations in core porosity above the transition from upper to lower Shikoku Basin facies. Laboratory measurements tend to overestimate porosity (Brown and Ransom, 1996) due to clay-bound water and the removal of samples from in situ temperature and pressure conditions (Hamilton, 1971).

Quality Assessment and Implications for Physical Properties

As indicated in "Quality of LWD Logs," p. 14, a differential caliper (DCAL) value of <1 in indicates good borehole conditions, for which the density log values are considered to be accurate to ±0.015 g/cm³. The uppermost 70 m of Hole 1173C (Fig. F25) is characterized by highly variable differential caliper values between 0.2 and 3 in. Differential caliper values average 1.8 in between 13 and 35 mbsf and 1.6 in between 35 and 55 mbsf. Between 55 and 70 mbsf, differential caliper values are reduced to 1.1 in. A closer examination of density and differential caliper values over these intervals shows that the highest differential caliper values correspond to low bulk density values. A good example of this inverse correlation can be seen in two peaks at 31 and 33 mbsf. Accordingly, most bulk density values down to ~55 mbsf appear to be anomalously low compared to those observed in similar depositional environments (Brückmann, 1989).

As reliable bulk density data are an essential prerequisite for modeling purposes and generating synthetic seismic profiles, Hole 1173A core-derived data were used to define a bulk density profile for the uppermost 60 m. A logarithmic curve that provides a more realistic approximation of bulk density was fitted to the Hole 1173C core bulk densities (Fig. F26):

$$\rho_b(z) = 1.384 + 0.158 \times \log(z).$$

F24. Comparison of LWD density–derived and core porosities, p. 62.

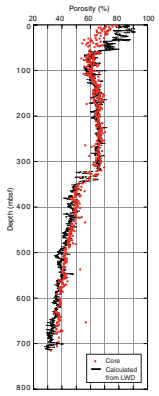

F25. Comparison of differential caliper and LWD density, p. 63.

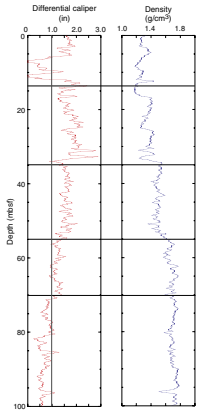

F26. Comparison of LWD and core densities and porosities, p. 64.

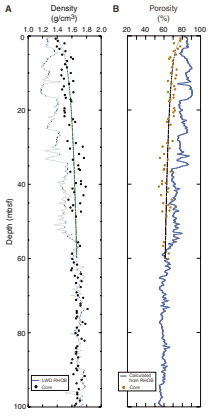

Using this density vs. depth function, a corrected porosity profile was calculated which yields a ϕ_0 value of 87.8% (Fig. F26).

Resistivity

Figure F27 shows the five resistivity logs (see "Logging while Drilling," p. 1, in the "Explanatory Notes" chapter for details about differences in acquisition, resolution, and depth of investigation). The borehole fluid was seawater although periodic mud sweeps (sepiolite) were used. The five logs show a similar overall resistivity trend. The bit resistivity log is smoother than the others because the bit electrode spans a larger vertical interval (2.7 m) (see "Logging while Drilling," p. 1, in the "Explanatory Notes" chapter). The previously defined log units are well expressed in the resistivity logs. Following is a description of each unit as observed on the ring resistivity log. Unit 1 has an average resistivity of ~0.6 Ωm. However, the quality of the logs in this unit may be degraded as suggested by the high value of the differential caliper signal (see "Quality of LWD Logs," p. 14). This unit is divided into two parts: Subunit 1a, where the resistivity increases from 0.4 to 0.7 Ωm with depth, and Subunit 1b, in which resistivity decreases from 0.6 to 0.4 Ωm with depth. The rate of decrease changes sharply at 122 mbsf, corresponding to the boundary between Subunit 1b and Unit 2. In Unit 2, resistivity decreases from 0.5 Ωm at 122 mbsf to 0.3 Ωm at the Unit 2/3 boundary (~340 mbsf). Two peaks, both ~10 m in thickness, mark the base of this unit. Unit 3 is characterized by a higher average resistivity (~0.55 Ωm) and a greater variability superimposed on a gradual increase with depth. The Unit 3/4 boundary (698 mbsf) is characterized by a peak of low resistivity (~0.3 Ωm). Resistivity in Unit 4, which corresponds to the volcaniclastic facies, increases rapidly with depth, reaching 0.75 Ωm at the boundary with Unit 5 (735 mbsf). Resistivities in Unit 5 are shown in detail in Figure F28. This unit is characterized by resistivities between 2.5 and 11 Ωm, and probably corresponds to basaltic basement.

A comparison of the five logs (Fig. F29) shows differences between resistivity values obtained from different measurement methods. The deep- and medium-focused resistivities give similar values, which can be seen in a correlation diagram where both resistivities fit very well (Fig. F30A). There are two intervals where the curves differ (550–554 and 612–630 mbsf). An unexplained feature is the inverse correlation of the different resistivity measurements. The shallow resistivity is systematically higher than both the deep and medium resistivity, which is opposite to the trend expected for this environment. This causes the correlation cloud to plot above the line of unit slope on the correlation diagram (Fig. F30B). The ring and bit resistivity logs similarly show differences in some regions of the log: bit resistivity is systematically higher in nearly all of Unit 2, whereas ring resistivity is higher in some zones of Unit 3. The correlation diagram (Fig. F30C) of these two sets of measurements accordingly presents an asymmetrical cloud. Finally, Figure F30D is a correlation diagram between deep and ring resistivity. It shows good agreement between those two measurements, with slightly lower values of deep resistivity.

The wireline resistivity log (dual induction tool [DIT]) measured during Leg 190 is plotted on Figure F29 for comparison. The correlation of signal peaks between Leg 190 and 196 measurements is very good, but the Leg 196 LWD resistivity values are ~0.1 Ωm lower than the wireline resistivity values. It should be noted that the DIT is an induction tool

F27. RAB resistivity logs from log Units 1–4, p. 65.

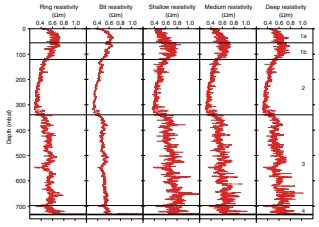

F28. RAB resistivity logs from log Unit 5, p. 66.

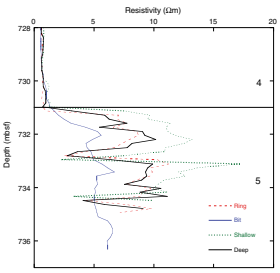

F29. Comparison of ring, bit, button, and wireline resistivities, p. 67.

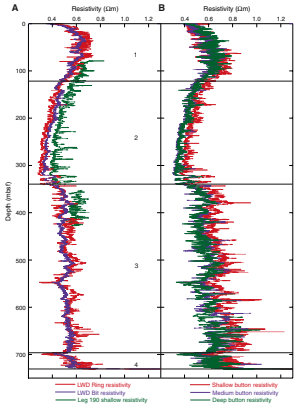

F30. Resistivity correlation diagrams, p. 68.

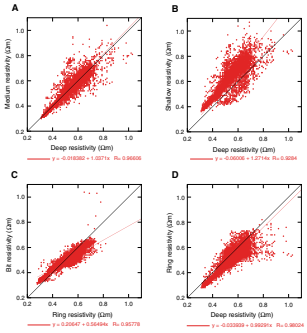

better adapted to measure low resistivity formations than the RAB tool used in Hole 1173B.

Neutron Porosity

The neutron porosity profile broadly mimics trends observed in other LWD logs (Fig. F31A), but with a larger degree of scatter. In log Unit 1 neutron porosity and core-derived porosity are in good agreement, whereas RHOB-derived porosity is consistently higher in log Unit 2 and increasingly lower in Units 3 and 4. Although the difference between neutron and RHOB-derived porosity in Unit 2 (differential porosity) is constant within ±10%, in Unit 3 the difference progressively increases downhole by about 5% to 15% (Fig. F31B). The increased separation between the two types of porosity is attributed to the lithologic change from upper to lower Shikoku Basin sediments that have higher clay mineral content. The neutron porosity is biased toward higher values by the bound water in clay minerals.

F31. Neutron, core, and RHOB-derived porosities, p. 69.

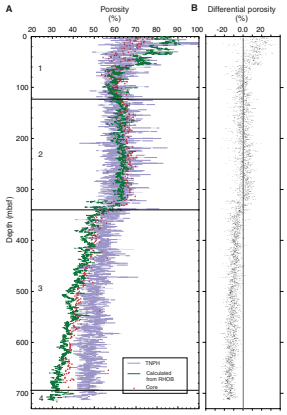

ISONIC *P*-wave Velocity

The ISONIC data returned to the ship after Schlumberger processing consisted of *P*-wave slowness at ~10-cm depth intervals and coherence of the stacked waveforms as a function of slowness and traveltime at the points where formation *P*-wave arrivals were picked (see "Quality of LWD Logs," p. 14). Identification and picking of the *P*-wave arrival from coherence analysis in ISONIC data is not straightforward. The preliminary ISONIC *P*-wave velocity values (Fig. F32) deviate substantially from core and wireline values, which correlate well with each other. Therefore we have low confidence in the quality of the preliminary waveform correlation picking of the formation *P*-wave phase and resulting calculated velocities. Further postcruise processing and analysis of ISONIC waveform data will be required to produce a log of formation *P*-wave velocity in which we have a high level of confidence.

F32. Comparison of ISONIC, wireline, and core *P*-wave velocities, p. 70.

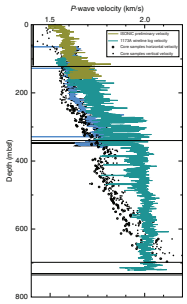

Summary

1. LWD density data in Holes 1173B and 1173C closely match core physical properties data from Hole 1173A, except for the uppermost 60 m where differential caliper values exceeded 1 in.
2. LWD densities are nearly constant in log Subunit 1b (55–122 mbsf) and Unit 2 (122–340 mbsf), with the notable exception of two high-amplitude variations near the transition from lithologic Unit II (upper Shikoku Basin facies) to Unit III (lower Shikoku Basin facies). Log Unit 3 (340–698 mbsf) is characterized by a steady increase in density consistent with a normal compaction trend.
3. All LWD resistivity logs show similar overall resistivity trends, in good agreement with Hole 1173A wireline logs. An unusual feature are shallow-focused resistivities that are consistently higher than medium- and deep-focused resistivities.
4. LWD ISONIC waveforms were successfully recorded, but picked velocities may contain substantial misidentification of the formation *P*-wave arrival. A final velocity log awaits postcruise research.

LOGS AND SEISMIC DATA

Synthetic Seismogram

We generated a synthetic seismogram from Site 1173 data using the most reliable density and velocity curves available and a source wavelet extracted from the seismic reflection data as described in "Core-Log Seismic Correlation and Seismic Resolution" p. 10, in the "Explanatory Notes" chapter (Fig. F33). For densities, we constructed logs from various sources for three intervals. An exponential curve through the core densities from Leg 190 Hole 1173A defined density from 0 to 60 mbsf, the LWD densities (RHOB) from Hole 1173C were used from 60 to 150 mbsf, and the LWD densities from Hole 1173B were used from 150 mbsf to total depth. LWD data in the 0- to 60-mbsf interval are unreliable due to excessive hole diameter as inferred from the differential caliper. For velocities, *P*-wave velocity core data from Leg 190 Hole 1173A defined the velocities for 0–81 mbsf, using a linear fit through the data, and 350 mbsf to TD, using the data directly. The wireline velocities from Leg 190 Hole 1173A were used for 81–350 mbsf. The water column was set at a density of 1.1 g/cm³ and a velocity of 1500 m/s. These logs result in a reasonable reflection coefficient at the seafloor of ~0.1–0.15.

Figure F33 shows the fit of the synthetic seismogram with 10 traces on either side of Hole 1173B. In addition to the good match at the seafloor in both waveform and amplitude, the synthetic seismogram matches well with the reflectivity in the seismic data from the seafloor to 340–350 mbsf. There are events in the synthetic seismograms that match the seismic data well at ~80–100, ~175, ~265–270, and ~300–350 mbsf (Fig. F33). At ~80–100 mbsf there is a compound reflection present in the synthetic and real seismic data beneath a relatively transparent upper layer. This upper layer has been defined lithologically as the outer trench–wedge unit and is underlain by the 19-m-thick outer trench–basin transition facies (Moore, Taira, Klaus, et al., 2001). The compound reflection observed at ~80–100 mbsf may be the result of a thin-layer interference effect from this unit. The boundary between log Units 1 and 2 is at 122 mbsf; so, the trench–basin transition, based on the interpretation of the synthetic seismogram, lies within log Unit 1 at ~80 to 100 mbsf. This apparent conflict may be resolved with more accurate velocities for time-to-depth conversion, or other interpretations of these reflections. At ~175 mbsf a distinctive reflection in the seismic data is reconstructed in the synthetic section due to a small coincident decrease in density and velocity. At ~265–270 mbsf a large velocity increase causes a reflection in the synthetic seismogram that correlates to an event observed in the three-dimensional (3-D) seismic traces. The boundary between the upper and lower Shikoku Basin units (log Units 2 and 3) near 340 mbsf in the 3-D seismic data is characterized by a zone of high reflectivity that is reasonably well matched in the synthetic seismogram. In the synthetic seismogram, this zone begins at ~300 mbsf, ends abruptly at ~350 mbsf, and lies 20–30 m above the corresponding zone in the 3-D seismic data. These reflections in the synthetic seismogram are attributed to a ~0.2 g/cm³ increase in density at ~300 mbsf, a zone of higher velocities by ~50 m/s between 340 and 350 mbsf, and a zone of lower velocities by ~50 m/s between 350 and 360 mbsf.

F33. Summary of synthetic seismogram analyses, p. 71.

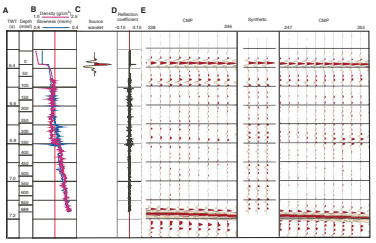

Below ~350 mbsf, the synthetic seismogram shows a number of strong reflections not seen in the 3-D seismic data intersecting Site 1173 on line 215. The mismatch correlates with variations in velocities measured on the cores and with variations in the LWD densities. The unmatched reflections in the synthetic seismogram below ~350 mbsf illustrate potential problems with core velocity measurements, such as sampling bias or disruption from in situ conditions, as they infer seismic reflections that are not observed in the 3-D data. The diminished reflectivity from Unit II to III is consistent with diagenetic changes in and increased homogeneity of Unit III.

In summary, correlations between the synthetic seismogram and seismic reflection data at ~80–100 and ~300–350 mbsf are consistent with core-defined lithologic boundaries and are regionally significant. Additional good correlations between the log and seismic data at ~175 and 265–270 mbsf and poor correlation beneath ~350 mbsf bear further investigation.

ACORK INSTALLATION

The LWD data collected in Hole 1173B essentially reconfirmed the scientific rationale for the planned distribution of four packers and five screens in the ACORK. These were configured in a 728-m-long ACORK string (Fig. **F1;** Table **T7**), to emphasize long-term observations of pressures in three principal zones, as follows:

T7. ACORK components and their depths, p. 90.

1. Oceanic basement below 731 mbsf, to determine permeability and pressures in the young oceanic crust being subducted, and thereby assess the role of oceanic crust in the overall hydrogeology at Nankai Trough. A screen was installed immediately above the ACORK shoe, centered at 722 mbsf, with a packer immediately above. As described in **"Operations,"** p. 5, the hole opening run successfully penetrated several meters into basement, and coring through the ACORK after its installation penetrated another 19.5 m. This assured that the signals of basement hydrogeologic processes would be transmitted to this deepest screen.
2. Lower Shikoku Basin deposits, well below the stratigraphic projection of the décollement zone, to assess the hydrological properties of a reference section of the lower Shikoku Basin deposits and test for fluid pressure propagation from basement or possibly higher in the section. A packer was centered at 495 mbsf to isolate a screen centered at 563 mbsf.
3. The stratigraphic projection of the décollement zone in the upper part of the lower Shikoku Basin deposits seaward from Sites 1174 and 808. The Leg 190 cores and wireline logs and Leg 196 LWD data showed only the slightest physical properties variations across this zone at ~390 to 420 mbsf, ~50–80 m below the boundary between the upper and lower Shikoku Basin deposits. A symmetric array ~100 m long, comprising three screens separated by two packers, was built into the ACORK string such that the three screens were centered at 439, 396, and 353 mbsf. Objectives of this array include (1) documenting the variation of hydrogeologic properties across and away from this zone as a reference for the state of the formation before the décollement zone actually develops closer to the trench axis and (2) detecting the possibility of fluid flow along the stratigraphic projection of

the décollement zone. In addition, the central screen in this array (i.e., the screen that spans the stratigraphic equivalent of the décollement zone) includes a second small-diameter line for eventual sampling of formation fluids from the wellhead.

After installation of the ACORK casing string, the RCB coring BHA was successfully deployed through it (Fig. F34), with the principal objective of deepening the hole into basement to assure that the signal of basement hydrogeologic processes will be transmitted to the deepest screen. A total of 19.5 m into basement was cored, with a recovery of 5.2 m (27% recovery). The core comprises basaltic basement overlain by a thin veneer of volcaniclastics. These cores were left on board for description by members of the Leg 197 Shipboard Scientific Party (see "Igneous Petrology and Volcanology," p. 30).

Following the basement coring, the final step in the ACORK installation at Hole 1173B was deployment of a bridge plug to seal the bore of the casing and isolate the basement section to be monitored by the deepest screen. We intended to set the bridge plug very near the bottom of the ACORK string, allowing future deployment of other sensor strings within the central bore. However, as is described in "Operations," p. 5, the bridge plug apparently set prematurely at 466 mbsf; this was not sensed at the rig floor and ensuing operations resulted in breaking the pipe off at the ACORK head. Nevertheless, detailed analysis suggested that the bridge plug was indeed set and there should be no broken pipe outside the ACORK head to inhibit future data recovery operations. Hence, we proceeded directly to Site 808 for the second planned ACORK installation; once that was completed we returned to Hole 1173B for an inspection that confirmed that the ACORK was undamaged and that the bridge plug was set (Fig. F35).

F34. Video of ACORK reentry, p. 72.

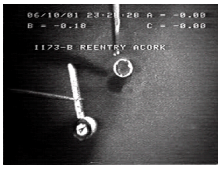

F35. Video of completed ACORK installation, p. 73.

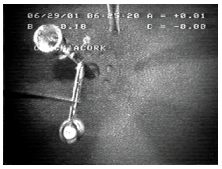

CORE PHYSICAL PROPERTIES

During Leg 196, 5.19 m of sediment and basalt was recovered from Hole 1173B between 737.1 and 756.6 mbsf. Physical properties data at this site provide important information about the shallowest oceanic basement before it experiences any potential deformation due to subduction.

Whole-round core sections were run on the multisensor track to collect magnetic susceptibility, gamma ray attenuation density, and natural gamma radiation measurements at 2- to 10-cm intervals. However, the data are considered unreliable because these measurements are sensitive to sample volume and the core pieces were relatively small and highly variable in diameter. Thus the results are not presented in this report.

Nine basalt minicores and two sediment samples were taken. The minicores were taken from unfractured parts without veins to avoid breaking. The minicores were then passed through the parallel saw blades to allow velocity to be measured on all three directions. Moisture and density (MAD) properties were measured on all samples and *P*-wave velocity was measured on the minicore samples.

MAD properties are shown in Table T8 and Figure F36. Porosities are 31% and 38% for the two sediment samples and 2.6% to 6.2% for the basalt samples. Bulk density for the sediment samples is 2.13 g/cm³, ~0.5 g/cm³ lower than for basalt. Although this difference in bulk density is primarily due to the porosity contrast, the difference in mineral

T8. *P*-wave velocity and MAD properties of core samples, p. 91.

F36. Core physical properties, p. 74.

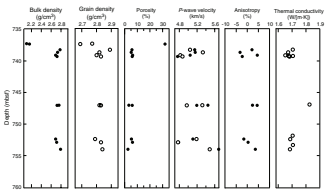

composition is also significant because the grain densities of sediment and basalt are 2.73 and 2.83 g/cm^3, respectively.

P-wave velocities were measured on basalt samples using the *P*-wave sensor 3 (PWS3) contact probe system. Velocities range between ~4.7 and ~5.5 km/s (Table T8; Fig. F36). No significant anisotropies are observed. Velocity shows a negative correlation to porosity. Moderately plagioclase-olivine-phyric basalt samples (Samples 196-1173B-2R-1, 21–24 cm, and 3R-2, 80–82 cm) show high velocities and low porosities, whereas sparsely plagioclase-phyric basalts, which tend to be significantly altered, show lower velocities and higher porosities.

Thermal conductivities were measured on archive half-rounds (Table T9; Fig. F36). Nine of the measurements show quite uniform values (1.69 ± 0.02 W/[m·K]). The tenth sample (Sample 196-1173B-2R-1 [Piece 4]) has higher conductivity (1.83 W/[m·K]). This sample has a very low porosity (3.3%) as compared with other basalts (5%–6%). Although we do not have enough porosity and conductivity data to apply a geometrical mean model to calculate the grain thermal conductivity, the large conductivity values could in part be explained by the small porosity of the sample.

T9. Thermal conductivity of core samples, p. 92.

IGNEOUS PETROLOGY AND VOLCANOLOGY[3]

Volcanic basement was encountered at Hole 1173B at 737.1 mbsf. No contact with the overlying sediment was recovered. We recognized two lava units within the recovered portion (5.19 m) of the 19.5 m of igneous basement drilled at Hole 1173B (27% recovery). In this section we describe the lithology, volcanic architecture, petrography, alteration features, and geochemistry of these units.

Lithology and Physical Volcanology

The volcanic basement section recovered at Site 1173 consists of two basalt lava units distinguished on the basis of differences in their phenocryst abundance.

Unit 1 (737.1–747.49 mbsf) is a sparsely vesicular plagioclase–phyric basalt with rare olivine phenocrysts. Equant plagioclase is the dominant phenocryst phase, typically 1–3 mm in size (range = 0.3–5 mm), comprising 3%–7% of the rock. The olivine content is typically <1%, and the phenocrysts range from 0.3 to 2 mm in size. The olivine phenocrysts are partly or completely pseudomorphed and are identified by their distinctive crystal habits and "ghost" fracture patterns.

Unit 2 (751.7–754.14 mbsf) is characterized by the same phenocryst assemblage as Unit 1, but the phenocryst abundance is markedly higher, the plagioclase content being typically ~10% and olivine content 2%–4%. As in Unit 1, olivine phenocrysts are partially to completely replaced by secondary minerals.

Both lava units contain small (<2 mm in diameter) spherical vesicles typically comprising <2% of the rock but rarely up to 6%. A few of the vesicles contain secondary sulfide (pyrite), and in one example (Sample 196-1173B–1R–1 [Piece 1]) spherical to elongate segregation vesicles are lined with a black cryptocrystalline segregation material with calcite filling the central void.

The groundmass is typically microcrystalline to fine grained with crystallinity ranging from holocrystalline through hypocrystalline to hypohyaline. The fine-grained holocrystalline lava is characterized by

[3]This section was written during Leg 197. See Leg 197 Contributors for addresses.

an intergranular texture, where dendritic feathery clinopyroxene and minute iron oxides occupy the void spaces, in a framework of plagioclase laths. The microcrystalline lava is typically hypocrystalline and exhibits a distinctive variolitic texture characterized by spherical domains of fanning intergrowths of skeletal plagioclase and dendritic clinopyroxene. In several places the variolitic portion of the lava grades into a 3- to 5-mm-thick horizon of silicified glass containing isolated submillimeter domains of ghost varioles. These relict glassy rinds are found only at the margins of rock pieces.

Hole 1173B lavas are characterized by cyclic variations in grain size and crystallinity, alternating between domains of fine-grained and microcrystalline lava (Table T10). The observed variations in groundmass textures, grain size, and crystallinity, along with the presence of relict glassy selvages/rinds, indicate that the lavas of Units 1 and 2 consist of multiple lobes, as indicated on the visual core descriptions (see "Site 1173 Visual Core Descriptions," p. 1). Furthermore, high cooling rates are implied by the skeletal and dendritic habits of crystals in the groundmass, along with the occurrence of variolitic texture (e.g., Lofgren et al., 1974). This evidence is consistent with the notion that each lava unit is made up of several thin, water-cooled lobes, and thus we interpret the sequence as pillow lavas.

T10. Summary of volcanic textures, p. 93.

Petrography

Plagioclase phenocrysts are readily distinguished from quenched groundmass plagioclase by their more equant, as opposed to lathlike, morphology and by slight resorption along the margins. Although plagioclase morphology is similar in the two units, plagioclase phenocrysts in Unit 2 exhibit optical zonation and occur either as single crystals or glomerocrysts. The olivine phenocrysts are partly or completely pseudomorphed by serpentine or talc (after serpentine), and/or red brown amorphous material (iron oxyhydroxide), but are readily identified by their distinctive crystal habits and ghost fracture patterns (Fig. F37).

F37. Large olivine phenocryst, p. 75.

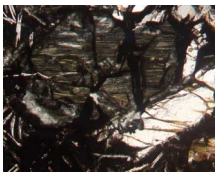

In most thin sections groundmass consists of a framework of skeletal plagioclase (40%–45%) with interstitial dendritic, sometimes branching, clinopyroxene (~40%) and subordinate amounts of interstitial titanomagnetite (2%–7%) (Fig. F38). Relict glass, indicated by interstitial patches of green-brown clay, is present in variable abundance. In one thin section (Sample 196-1173B-1R-2, 18–20 cm), the groundmass is characterized by variolitic texture with fanning domains of skeletal plagioclase needles intergrown with dendritic clinopyroxene (Fig. F39).

F38. Fine-grained groundmass surrounding a microscopic amygdale, p. 76.

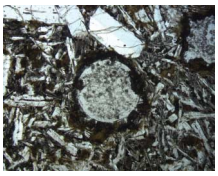

Alteration

Fluid/rock interaction after emplacement has slightly to moderately altered all volcanic rocks encountered at Hole 1173B. Secondary minerals fill veins and vesicles and partly or completely replace mesostasis and primary phases, such as olivine. Alteration consists mostly of red-brown (iron oxyhydroxide) alteration halos, 3 to 5 mm wide. Small (<2 mm wide) fractures and veins are randomly oriented and are filled with several successive stages of alteration minerals, usually calcite and green and brown clay minerals. In Section 196-1173-2R-1, veins are further lined by secondary sulfides, which are identified as pyrite in the thin section of Sample 196-1173-3R-2, 83–85 cm.

F39. Variolitic texture, p. 77.

Geochemistry

Two samples of the igneous basement were analyzed using inductively coupled plasma–atomic emission spectrometry (ICP-AES). Analytical techniques are described in "Igneous Petrology and Volcanology," p. 21, in the "Explanatory Notes" chapter. To compare the compositions of the units, samples were taken from near the top (Unit 1, next to thin section Sample 196-1173B-1R-1, 99–101 cm) and bottom of the core (Unit 2, next to thin section Sample 196-1173B-3R-2, 83–85 cm). Each sample was analyzed twice (Table T11).

On the basis of SiO_2, Na_2O, and K_2O contents, both samples are tholeiitic basalts. They are evolved basalts with moderate MgO (5.95 and 6.19 wt%) and Ni contents (76 and 88 ppm). There are significant compositional differences between the two samples. Compared to the Unit 2 sample, the Unit 1 sample has higher TiO_2, P_2O_5, Zr, and Y contents. These elements are relatively immobile during seafloor alteration; thus, the differences between the samples are unlikely to be the result of variable alteration in different parts of the core. These samples have compositions similar to average N-type mid-ocean-ridge basalt but have higher Sr and Ba concentrations.

T11. Chemical compositions of basalt, p. 96.

PALEOMAGNETISM AND ROCK MAGNETISM[4]

Discrete samples from Hole 1173B were demagnetized during Leg 197 using an alternating field (AF) of 0 to 80 mT, at 5-mT steps for the first 50 mT and at 10-mT steps for the remaining treatments, to isolate stable remanence components in the samples. Characteristic remanent magnetizations (ChRMs) were obtained using principal component analysis (Kirschvink, 1980), and the stability of remanence was determined using Zidjerveld (1967) plots and equal-area projections.

All samples showed a relatively strong magnetic overprint, which was likely imparted by the drill string and/or Earth's present-day magnetic field. AF demagnetization spectra (Fig. F40) show that the samples have a rather low bulk coercivity, with median destructive fields ranging between 5 and 12 mT. In five of the six samples analyzed, the overprint appeared to be removed after demagnetization to 15–35 mT (Fig. F40A, F40B, F40D, F40E, F40F). For these samples, a stable reversed-polarity ChRM could be fit by principal component analysis. However, departures of linear fits to the data from the origins of orthogonal vector plots indicate the presence of high-coercivity magnetic phases that were not demagnetized by the applied AF treatments. For Sample 196-1173B-1R-1, 61–63 cm, the AF demagnetization applied was insufficient to remove the overprint and a ChRM could not be isolated (Fig. F40C). In Sample 196-1173B-3R-2, 14–16 cm, the definition of the ChRM declination after removal of the overprint was scattered, resulting in a fit with a very large median angular deviation (Table T12).

The three stratigraphically highest samples yielding ChRMs have inclinations between –18° and –23°. The two stratigraphically deepest samples analyzed have ChRM inclinations of –38°. Because of this stratigraphic relationship, the magnetizations suggest that the recovered core might record two polarity intervals. However, because the linear fits deviate from the origin of orthogonal vector plots, the paleomagnetic inclination differences might instead arise from the differential presence of small amounts of high-coercivity magnetic minerals and/or the variable effectiveness of AF demagnetization in remov-

F40. Zidjerveld diagrams of AF-demagnetized samples, p. 78.

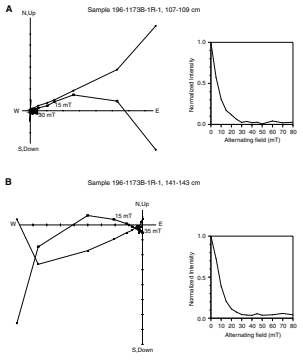

T12. Characteristic remanent magnetization inclinations, p. 97.

[4]This section was written during Leg 197. See Leg 197 Contributors for addresses.

ing magnetic overprints. Because of these possibilities, the uncertainties of the reported ChRM directions (the median angular deviation; Table T12) should be considered to be minimum values. Detailed shore-based paleomagnetic and rock magnetic analyses employing thermal demagnetization are needed to further evaluate these issues.

The average inclination of the two groups of ChRM directions, following the inclination averaging technique of McFadden and Reid (1982), is –30.2°. (The small number of paleomagnetic units prevents the application of formal uncertainty analyses, which are valid when the number of units is three or greater.) The average inclination value can be used to calculate a nominal paleolatitude using the geocentric dipole relationship:

$$\tan I = 2 \tan l,$$

where I is the mean ChRM inclination and l is the paleolatitude. This is a nominal value because the recovered basalt does not contain enough time-independent inclination units to adequately average geomagnetic secular variation (see discussion in Tarduno and Sager, 1995). Nevertheless, the nominal paleolatitude (16.2°N) is useful for discussing the potential meaning of the measured magnetic data.

Hole 1173B is located at 32°14.66′N, 135°01.51′E. The present-day geocentric axial dipole (GAD) inclination at this site is 51.6°. The ChRM inclinations are substantially shallower than the present-day GAD value. The age of the basalt sampled at Site 1173 is thought to be 15.6 Ma (Siena et al., 1993) and therefore plate motion might explain part of the difference between the measured data and the present-day GAD value. However, inadequacies of the demagnetization to isolate ChRM directions, insufficient averaging of secular variation, and tectonic complexity (tilting) offer sufficient explanations of the preliminary data available from the limited penetration and core recovery.

The magnetic polarity of the basalt is a stronger interpretation that can be made from the preliminary shipboard data. The reversed polarity is consistent with a number of reversed-polarity chrons between 15 and 20 Ma (Cande and Kent, 1995; Fig. F41).

F41. Site 1173 age and geomagnetic polarity timescale, p. 81.

DISCUSSION AND SYNTHESIS

The major feature at Site 1173 is the Shikoku Basin section that extends from ~100 to 698 mbsf and is divided into an upper and lower facies (lithologic Units II and III). The two units are differentiated at least in part by a diagenetic front rather than purely depositional features. The log response is dominated by the relatively homogenous properties of this predominantly hemipelagic silty clay section.

LWD Comparison with Core and Wireline Data

LWD data collection at Site 1173 confirmed Hole 1173A wireline and coring results and extended them to greater depths and higher resolution, respectively. Comparison of LWD logging results with Leg 190 core-based physical properties and wireline data (Fig. F1) generally shows excellent agreement among the various measured parameters. The log units defined on the basis of visual inspection and statistical analysis coincide well for the most part with the lithologically defined units. Log Unit 1, the outer trench wedge, has a lower boundary that

differs by ~20 m in depth from the equivalent boundary of lithologic Unit I. However, this boundary is gradational in the cores and defined on the basis of the deepest occurrence of clearly identified but volumetrically minor silty turbidites. Hence the log unit definition probably only differs in the placement of a sharp line through a gradational boundary. The Unit 2/3 boundary coincides within a few meters; it is chosen at 340 mbsf in the log units and 343.8 mbsf in the lithostratigraphic units on the basis of slightly different selection criteria (trough of deepest excursion vs. deepest unambiguous ash with unaltered glass). The Unit 4 boundary also coincides well (688 and 698 mbsf in cores and logs, respectively), with the difference being attributed to poor core recovery.

Structural features identified in the interpretation of the RAB images are consistent with those identified in cores in their nature, depth distribution, and orientation. Intervals of subhorizontal vs. significantly inclined bedding correspond between both data sets. Both also indicate steeply dipping fractures or minor faults, probably associated with compaction and/or the normal faulting imaged in the seismic reflection data. RAB imaging has certain trade-offs in comparison to FMS images collected during Leg 190: whereas FMS data have much higher spatial resolution, RAB images provide full 360° coverage of the borehole wall. Ash layers identified in Hole 1173A FMS images can be correlated to features imaged with the RAB tool, providing a sense of the relative response and resolution of the two instruments (Fig. F42). Maximum resolution within RAB images is thought to be ~3 cm, whereas resolution for FMS images is ~0.5 cm (Moore, Taira, Klaus, et al., 2001). Thinner ash layers can be clearly identified in the FMS images (e.g., at 336 and 338–339 mbsf) but are not easily distinguished in RAB images. Further correlation between RAB images, FMS images, and core descriptions indicates a discrepancy between visible ash thickness and extent of resistivity signature. For example, the ash layer that defines the base of Unit II is 3 cm thick in the recovered core but produces a significant resistivity anomaly over tens of centimeters in both RAB and FMS images (Fig. F42). The broader resistivity signature may in part result from reworking caused by bioturbation. Larger scale variations in resistivity (5–10 m scale) are easily correlated between the RAB and FMS images and can often be correlated with other physical properties. The high-resistivity interval at 333–338 mbsf (RAB and FMS; Fig. F42) corresponds to a peak in density (Fig. F29). The FMS image indicates a high frequency of thin ash layers, whereas the more homogeneous resistivity high in the RAB image suggests reworking of high-resistivity beds (ash layers) over this interval.

F42. Comparison of FMS and RAB resistivity images, Unit 2/3 boundary, p. 82.

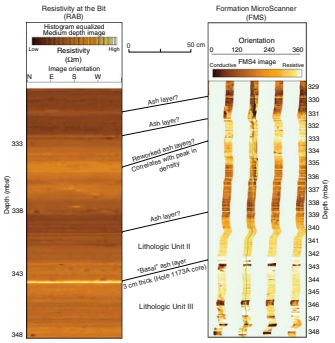

Important Intervals

Here, we highlight the interpretation of several zones of special interest identified at Site 1173. These include the apparently diagenetically controlled boundary between log Units 2 and 3 and lithostratigraphic Units II and III, respectively; the reverse porosity vs. depth trend within log Unit 2; and the projected stratigraphic equivalent of the décollement zone at Sites 1174 and 808.

Upper/Lower Shikoku Basin Facies Boundary

The boundary between the upper and lower Shikoku Basin facies was defined in Leg 190 Hole 1173A at the deepest occurrence of a fresh vol-

canic ash bed containing glass shards seen in smear slides, although this was chosen within a gradational change from ash to siliceous claystone. This boundary occurs at a mineral phase transition from cristobalite to quartz and where the pore water SiO_2 content drops sharply (Moore, Taira, Klaus, et al., 2001). An added complexity is that clay content also increases at this boundary.

This transition also strongly affects the sediment physical properties. In core measurements, density increases, porosity decreases, and formation factor increases sharply across the boundary but *P*-wave velocity varies only weakly (Shipboard Scientific Party, 2001). The LWD data exhibit corresponding trends across the depth-equivalent log Unit 2/3 boundary. Resistivity and density exhibit a baseline shift to higher values below the boundary, as well as two excursions to similarly high values over an ~20-m-thick transitional zone between 320 and 344 mbsf. Porosity mirrors the density trend. The gamma ray log shows a pronounced increase across the transition, matching the clay mineral content (Fig. F1), and fluctuations in the transition zone are also observed in this log.

Taken together, these data are consistent with the previous interpretation of a largely diagenetically controlled boundary, with the cristobalite to quartz transition dominating the changes in physical properties (Moore, Taira, Klaus, et al., 2001). The sudden increase in density and resistivity associated with a porosity loss may indicate a loss of matrix strength due to cement dissolution (Isaacs et al., 1983). This alteration is variably developed over the ~20-m-thick transition interval, perhaps because of variations in silica content of the sediments over this range. The coincidental downhole transition to slightly higher clay content at this boundary may represent either a change in clay deposition or clay diagenesis, presumably also because of ash alteration. The temperature-controlled nature of this diagenetic front suggests that identification of the equivalent lithologic Unit II/III boundary at more landward sites must be approached with caution.

Compaction Trend

Above the lithologic Unit II/III boundary, the log trends deviate sharply from typical profiles of compacted deepwater sediments. Density and porosity exhibit normal compaction trends to ~60–80 mbsf but remain nearly constant below this depth to ~320 mbsf, actually reversing direction from the expected compaction trend (i.e., density decreases and porosity increases slightly). Resistivity wireline and LWD logs trend to lower values through this interval, paralleling the density. Because resistivity is primarily sensitive to saline pore fluid, we attribute this trend to the downhole increase in porosity over the same interval. As was interpreted on Leg 190 (Moore, Taira, Klaus, et al., 2001), these anomalies taken together are tentatively attributed to some combination of (1) the gradual downward transition from more terrigenous, coarser grained sediments of the trench–basin facies (Subunit 1b) to the more clay-rich sediments of the upper Shikoku Basin facies and (2) subtle cementation effects of silica diagenesis.

Stratigraphic Equivalent of the Décollement Zone

During Leg 190, a correlation was made via core magnetic susceptibility data of the known positions of the décollement zone at Sites 808 and 1174 to the equivalent interval at Site 1173; this interval can also

be identified in the magnetic susceptibility data of reference Sites 1173 and 1177. The resulting projected equivalent of the Site 1174 décollement zone (Shipboard Scientific Party, 2001) is shown in Figures **F1** and **F43.** Whereas there are excursions in several of the logs over this interval, it does not substantially stand out from the over- and underlying formation in any of the measured logs. There is an abrupt resistivity excursion to lower values at ~384 mbsf and back to higher values at ~412 mbsf, although the amplitude does not stand out strongly from other variations above and below. The same excursion can be weakly identified in the density and computed porosity logs. Overall, the specific interval projected as the stratigraphic equivalent of the décollement zone does not exhibit obviously unusual properties relative to the surrounding sediments.

F43. Log properties of the stratigraphic equivalent of the décollement zone, p. 83.

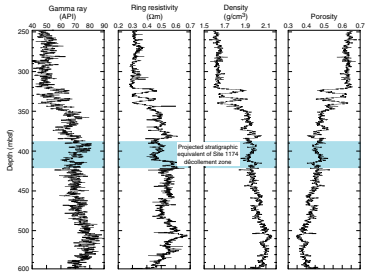

REFERENCES

Brown, K.M., and Ransom, B., 1996. Porosity corrections for smectite-rich sediments: impact on studies of compaction, fluid generation, and tectonic history. *Geology,* 24:43–84.

Brückmann, W., 1989. Typische kompaktionsmuster mariner sedimente und ihre modifikation in einem rezenten akkretionskeil (Barbados Ridge). *Beitr. Geol. Inst. Univ. Tuebingen, Rh. A,* 5:1–135.

Cande, S.C., and Kent, D.V., 1995. Revised calibration of the geomagnetic polarity timescale for the Late Cretaceous and Cenozoic. *J. Geophys. Res.,* 100:6093–6095.

Hamilton, E.L., 1971. Prediction of in-situ acoustic and elastic properties of marine sediments. *Geophysics,* 36:266–284.

Isaacs, C.M., Pisciotto, K.A., and Garrison, R.E., 1983. Facies and diagenesis of the Miocene Monterey Formation, California: a summary. *In* Iijima, A., Hein, J.R., and Siever, R. (Eds.), *Siliceous Deposits in the Pacific Region*. Dev. Sedimentol. Ser., U.S. Geol. Surv., 36:247–282.

Kirschvink, J.L., 1980. The least-squares line and plane and the analysis of palaeomagnetic data. *Geophys. J. R. Astron. Soc.,* 62:699–718.

Lofgren, G.E., Donaldson, C.H., Williams, R.J., Mullins, O., and Usselman, T.M., 1974. Experimentally reproduced textures and mineral chemistry of Apollo 15 quartz normative basalts. *Proc. Lunar Sci. Conf.,* 5:549–567.

McFadden, P.L., and Reid, A.B, 1982. Analysis of palaeomagnetic inclination data. *Geophys. J. R. Astron. Soc.,* 69:307–319.

Moore, G.F., Taira, A., Klaus, A., et al., 2001. *Proc. ODP, Init. Repts.,* 190 [CD-ROM]. Available from: Ocean Drilling Program, Texas A&M University, College Station TX 77845-9547, USA.

Moore, G.F., Taira, A., Klaus, A., Becker, L., Boeckel, B., Cragg, A., Dean, A., Fergusson, C.L., Henry, P., Hirano, S., Hisamitsu, T., Hunze, S., Kastner, M., Maltman, A.J., Morgan, J.K., Murakami, Y., Saffer, D.M., Sánchez-Gómez, M., Screaton, E.J., Smith, D.C., Spivack, A.J., Steurer, J., Tobin, H.J., Ujiie, K., Underwood, M.B., and Wilson, M., 2001. New insights into deformation and fluid flow processes in the Nankai Trough accretionary prism: results of Ocean Drilling Program Leg 190. *Geochem. Geophys. Geosyst.,* 2:10.129/2001GC000166.

Rider, M.H., 1996. *The Geological Interpretation of Well Logs* (2nd ed.): Caithness (Whittles Publishing).

Shipboard Scientific Party, 2001. Site 1173. *In* Moore, G.F., Taira, A., Klaus, A., et al., *Proc. ODP, Init. Repts.,* 190, 1–147 [CD-ROM]. Available from: Ocean Drilling Program, Texas A&M University, College Station TX 77845-9547, USA.

Siena, F., Coltorti, M., Saccani, E., and Vaccaro, C., 1993. Petrology of the basaltic rocks of the Nankai Trough basement. *In* Hill, I.A., Taira, A., Firth, J.V., et al., *Proc. ODP, Sci. Results,* 131: College Station, TX (Ocean Drilling Program), 197–207.

Tarduno, J.A., and Sager, W.W., 1995. Polar standstill of the mid-Cretaceous Pacific plate and its geodynamic implications. *Science,* 269:956–959.

Zidjerveld, J.D.A., 1967. A. C. demagnetization of rocks: analysis of results. *In* Collinson, D.W., Creer, K.N., and Runcorn, S.K. (Eds.), *Methods in Paleomagnetism:* Amsterdam (Elsevier), 254–286.

Figure F1. Site 1173 summary diagram showing combined results of Legs 190 and 196. From left to right: depth-converted seismic reflection data, core recovery, core-based lithology and facies interpretation, bedding dip, pore water geochemistry, temperature-depth gradient, wireline and log resistivity, clay mineral content (solid circles) and gamma ray log, core and log density, core and log porosity (computed from the density log using core grain density values), log units, and a schematic diagram of the Advanced CORK (ACORK). CDP = common depth point, RAB = resistivity at the bit, SFLU = spherically focused resistivity, XRD = X-ray diffraction. (See Fig. F6, p. 22, in the "Leg 196 Summary" chapter for an oversized version.) (Continued on next page.)

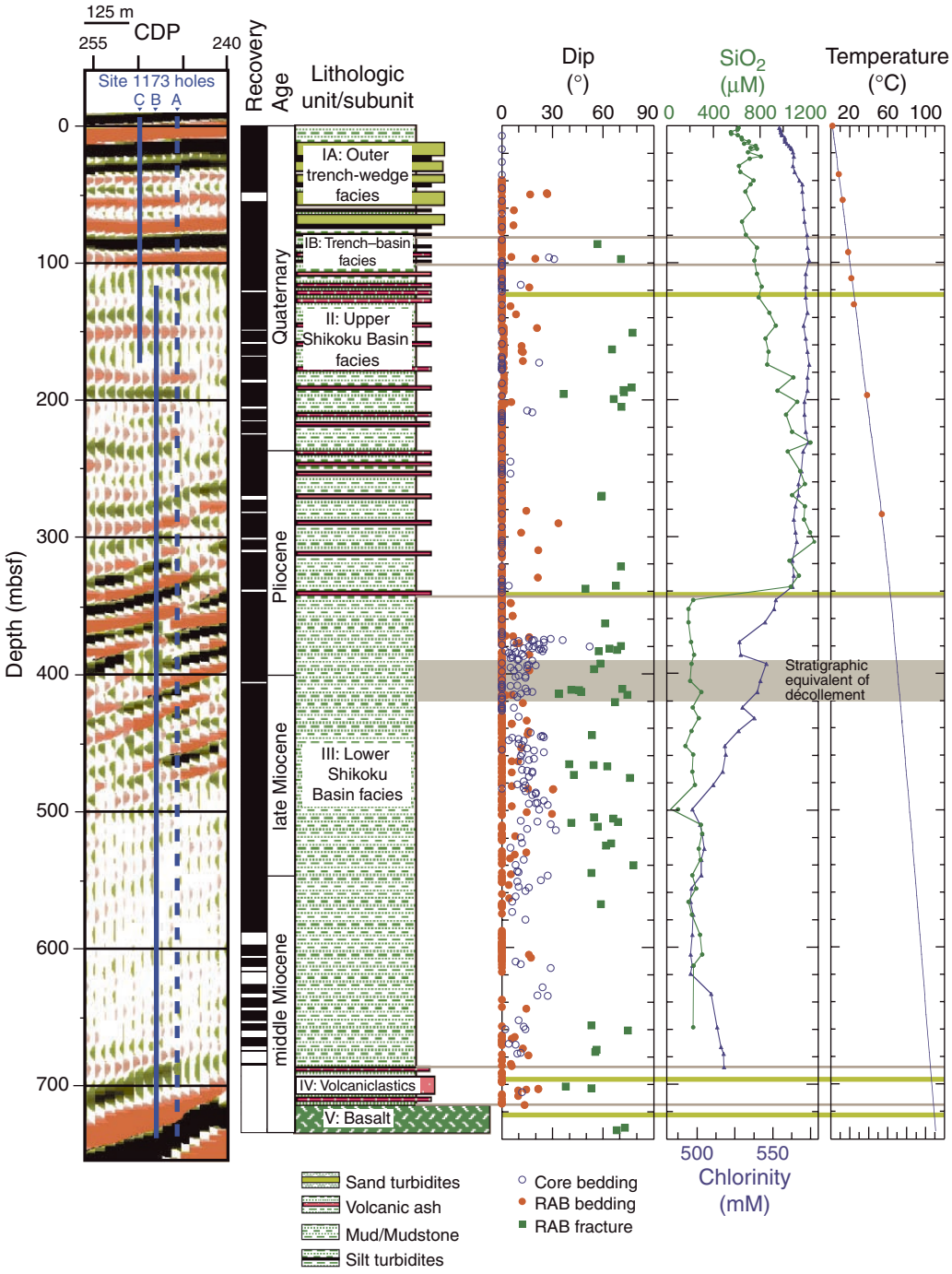

Figure F1 (continued).

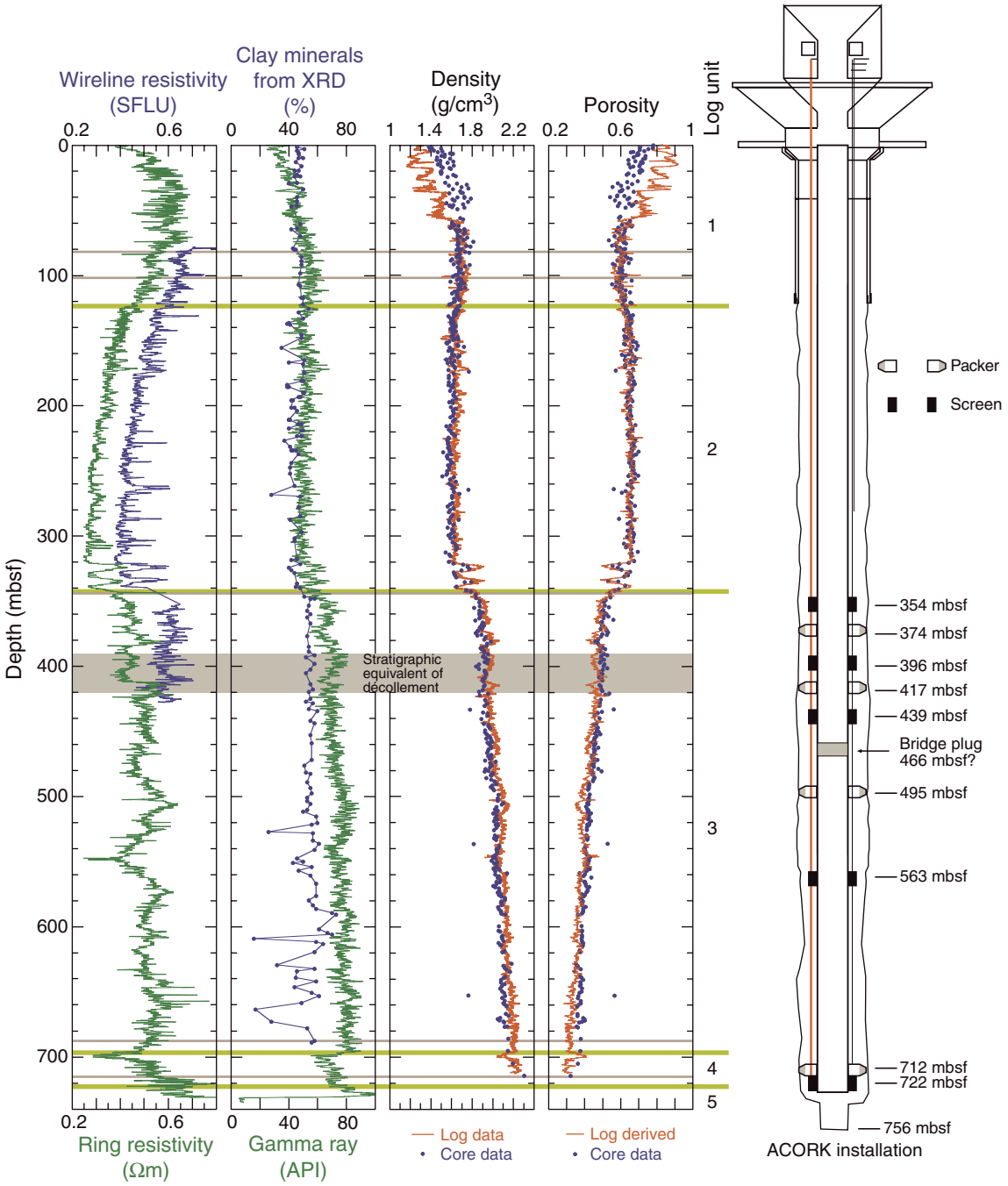

Figure F2. Locations of Leg 196 drill sites (yellow circles with black outlines). Site 1173 is ~11 km southeast (seaward) of the deformation front of the accretionary prism, which is shown by the northeasterly oriented ridges northwest of Site 1174. The line passing through Site 1173 shows the location of the seismic profile shown in Figure F3, p. 41. The outlined area shows the extent of the three-dimensional seismic data coverage. Depth contours are in kilometers.

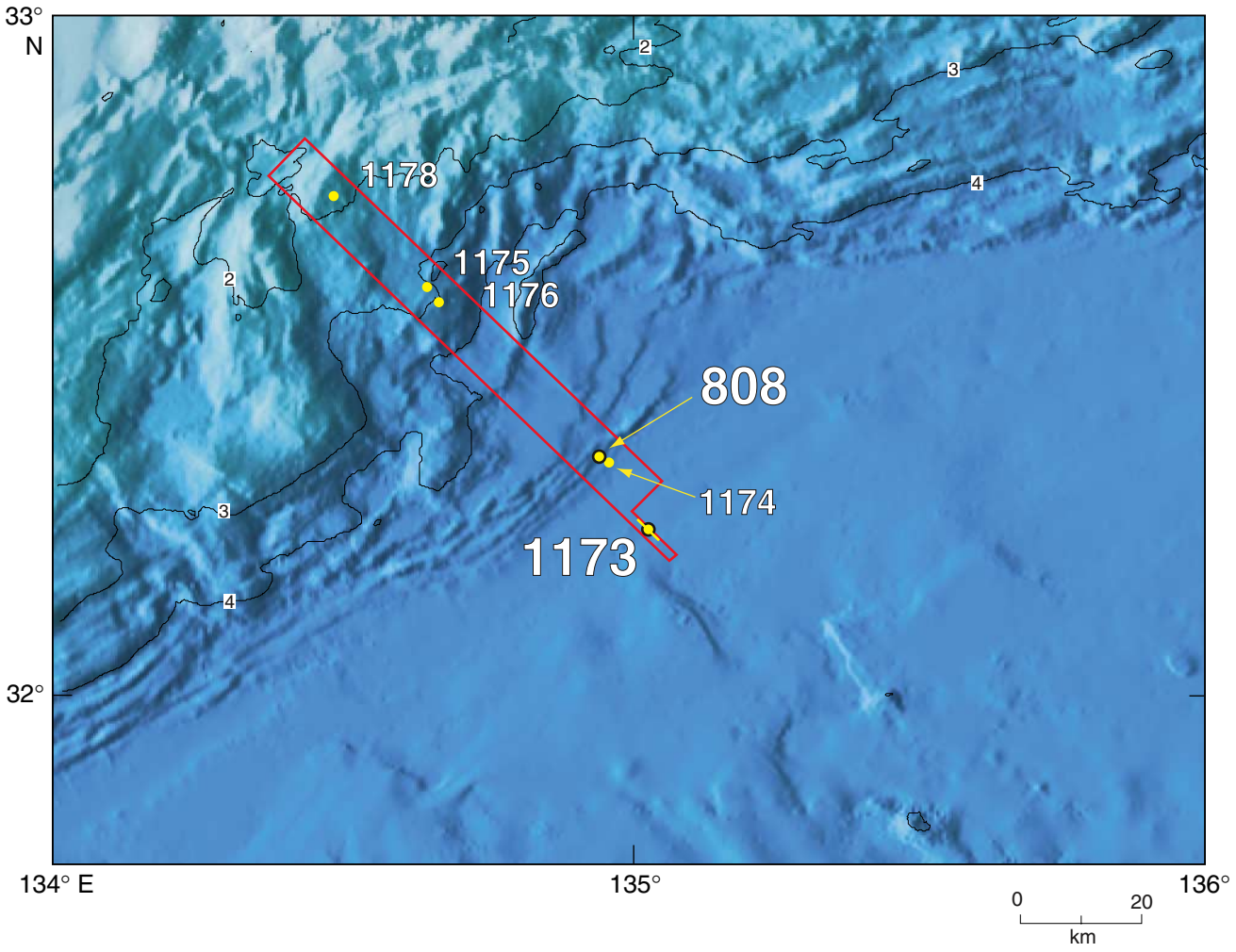

Figure F3. Seismic line crossing Site 1173. Location of seismic profile is shown in Figure F2, p. 40. CDP = common depth point, VE = vertical exaggeration.

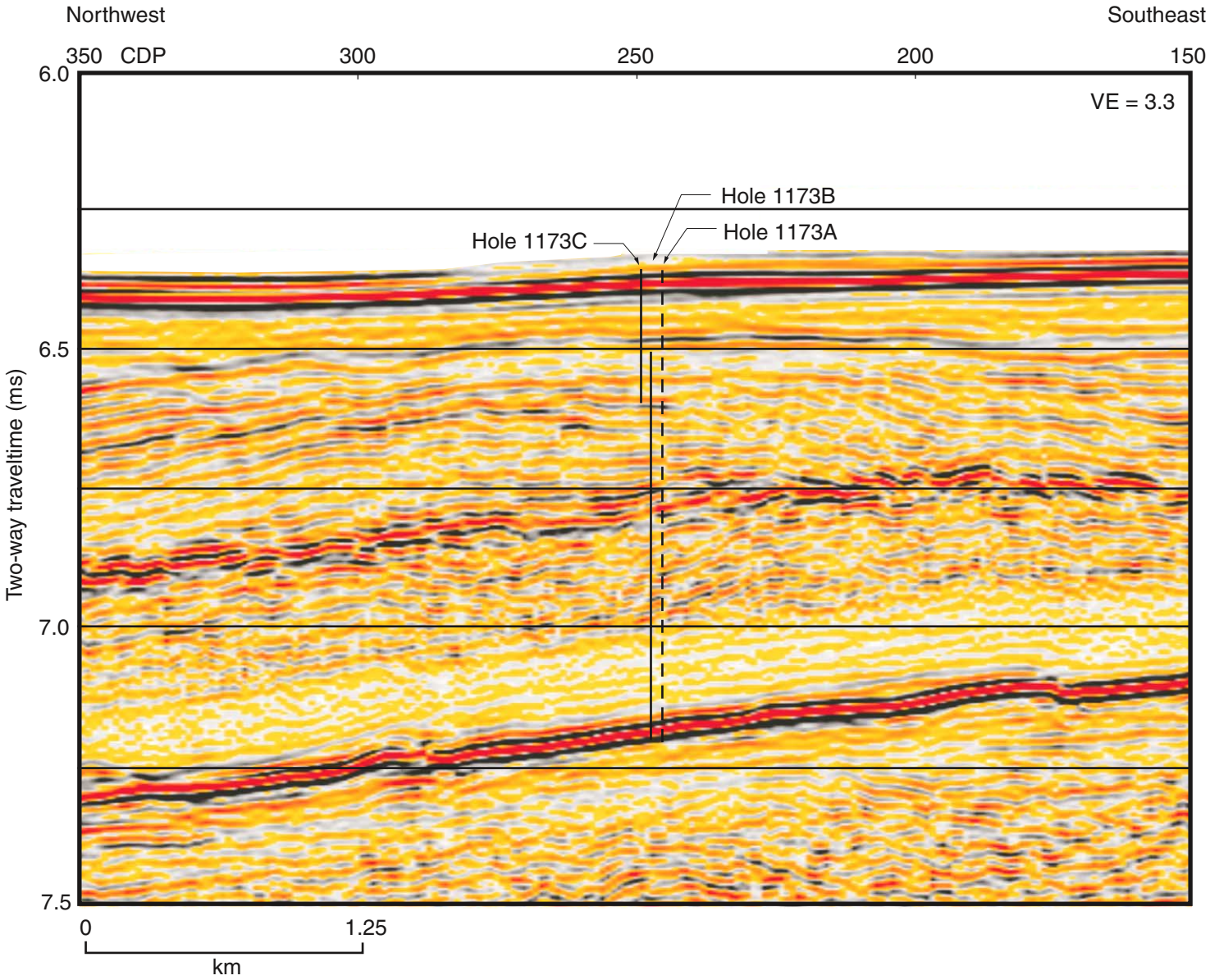

Figure F4. Summary of the quality-control logs, Hole 1173B.

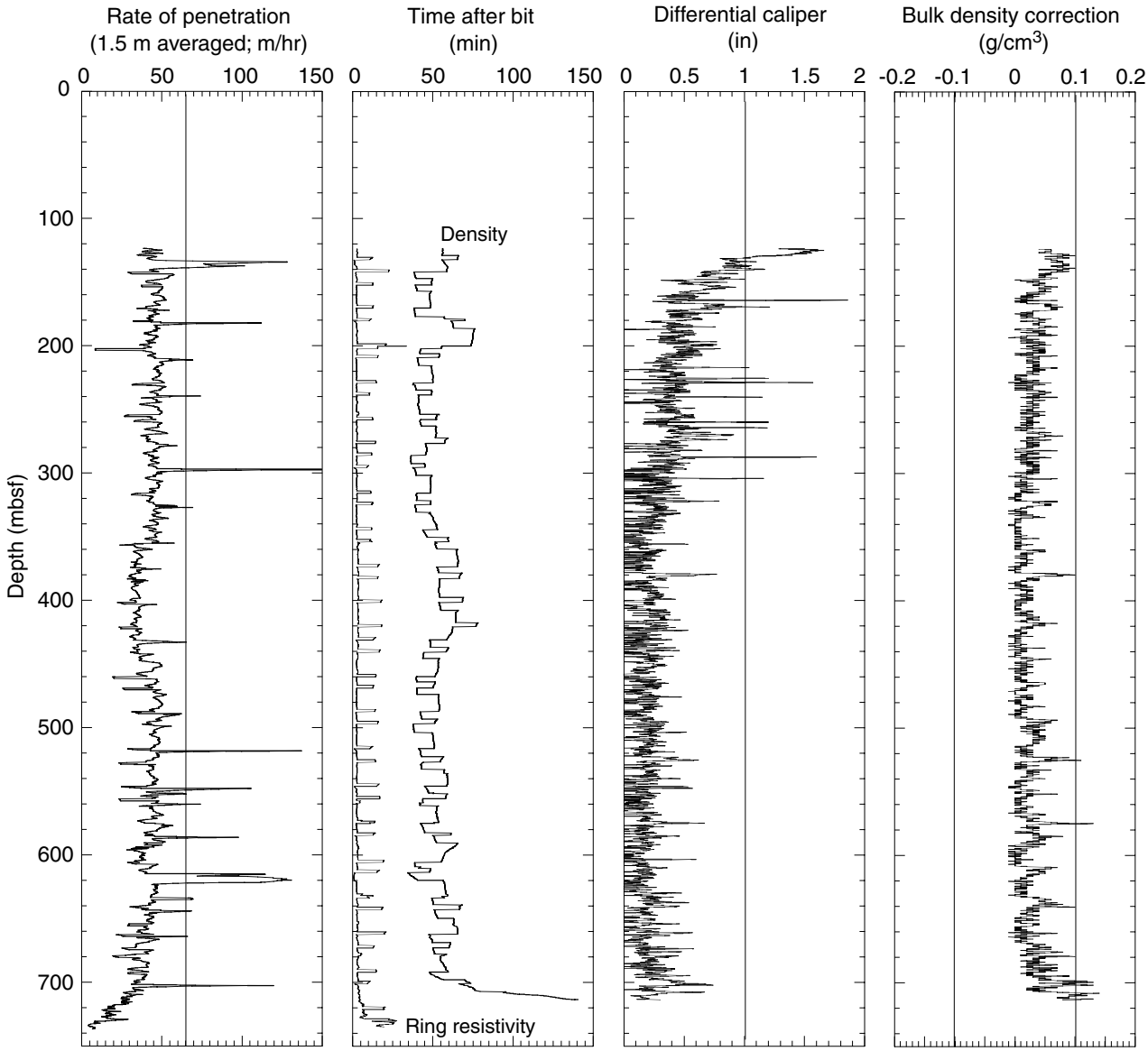

Figure F5. Summary of the quality-control logs, Hole 1173C.

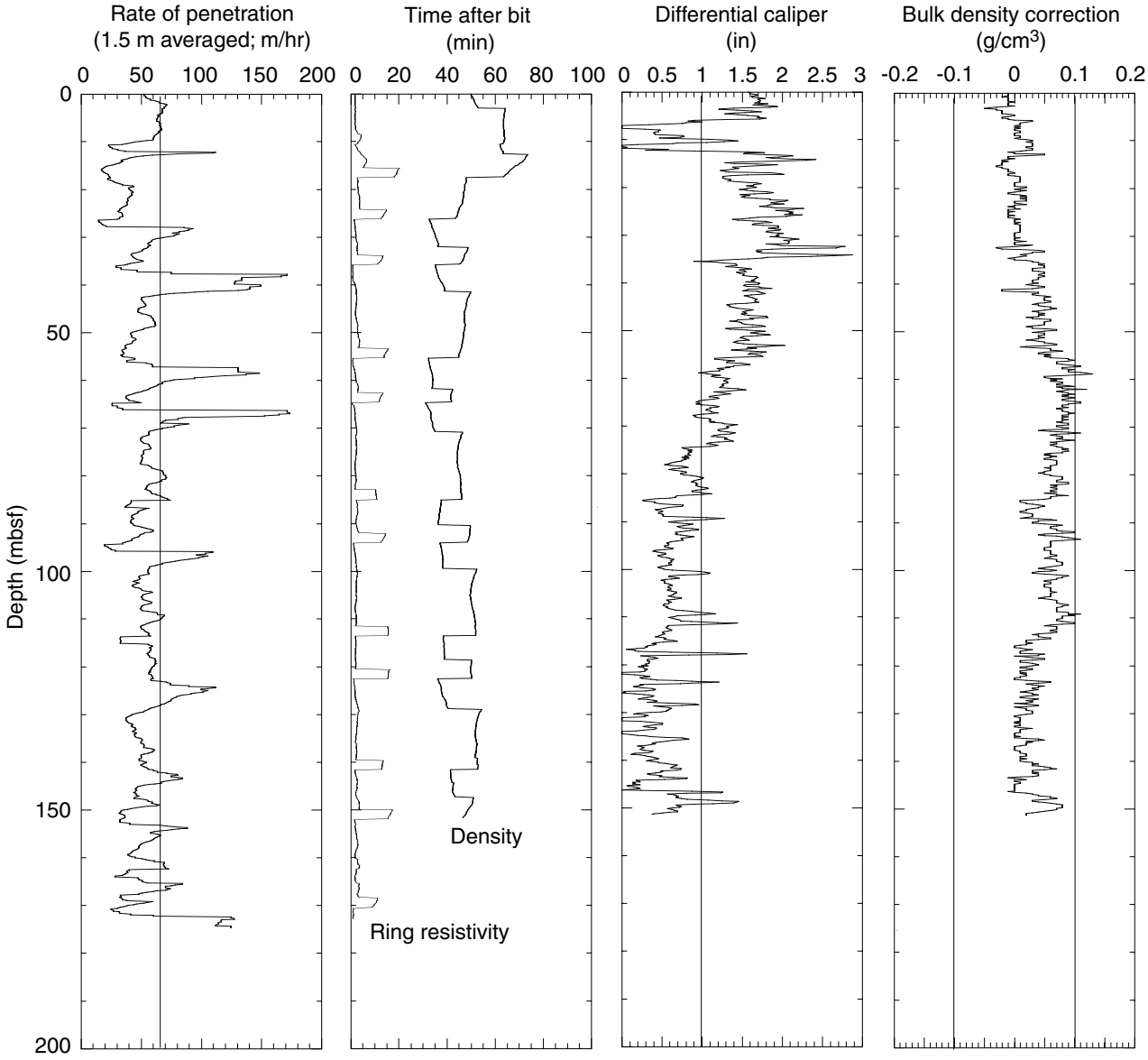

Figure F6. Example waveforms from the IDEAL sonic-while-drilling tool, showing the main arrivals at the four receivers (receiver distances above the source are 3.04 m for R1, 3.25 m for R2, 3.45 m for R3, and 3.66 m for R4) at depths (**A**) 262.15 mbsf (5064.05 mbrf) and (**B**) 397.58 mbsf (5199.48 mbrf; depths are measured to midway between R2 and R3) in Hole 1173B. Arrows indicate the first arrival of a leaky *P*-wave (LP) mode. **C, D.** Contour plots of coherence against slowness and arrival time for the wavetrains in (A) and (B). The diagonal lines show the limits within which real arrivals are expected; peaks outside these limits are likely to be noise or aliased signal. Peaks due to the leaky *P*-wave mode are indicated by LP. Diagram courtesy of V. Pistre, Schlumberger.

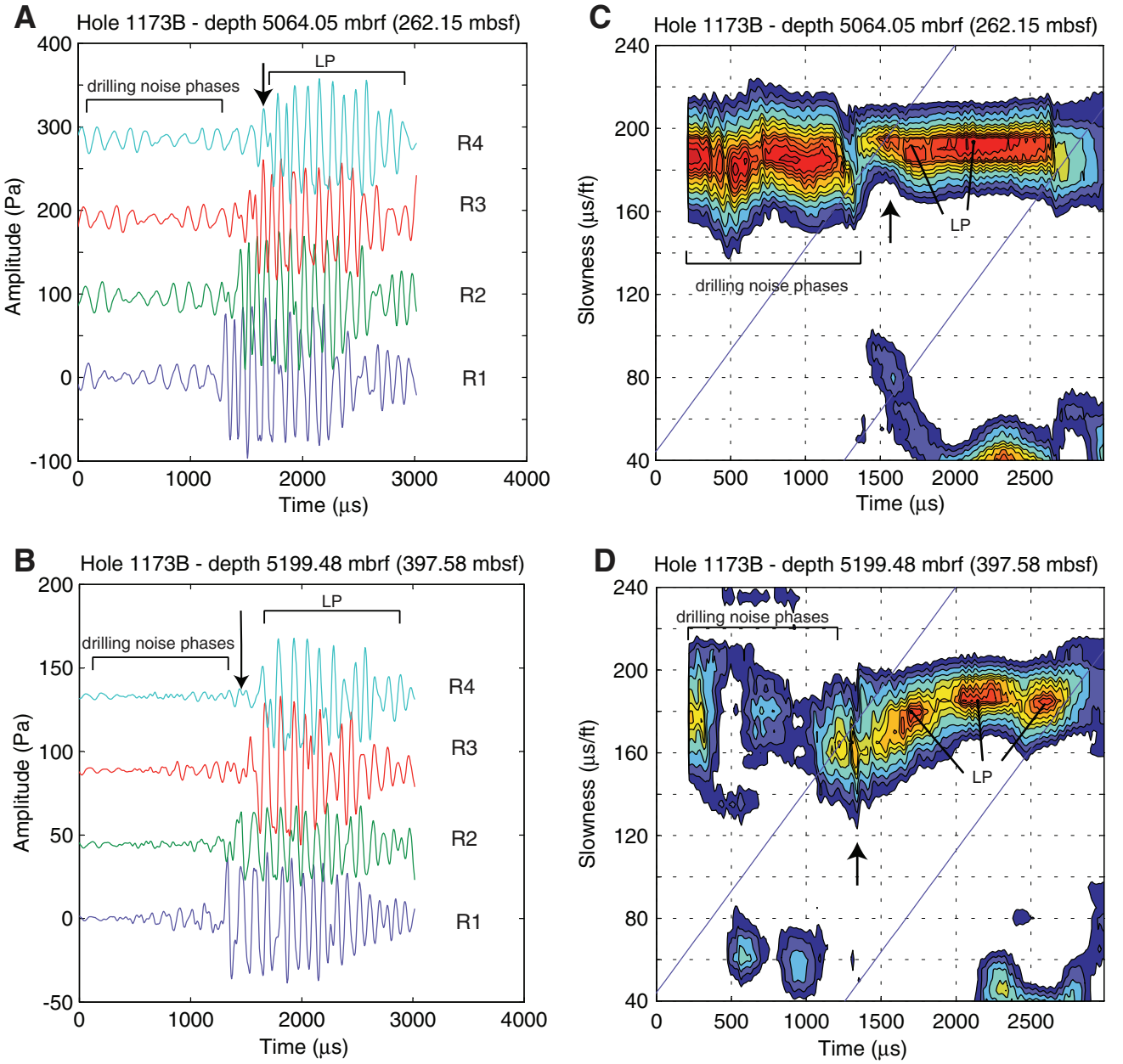

Figure F7. Resistivity correlation diagram for the overlapping interval in Holes 1173B and 1173C. Letters denote significant peaks that can be correlated in the resistivity logs.

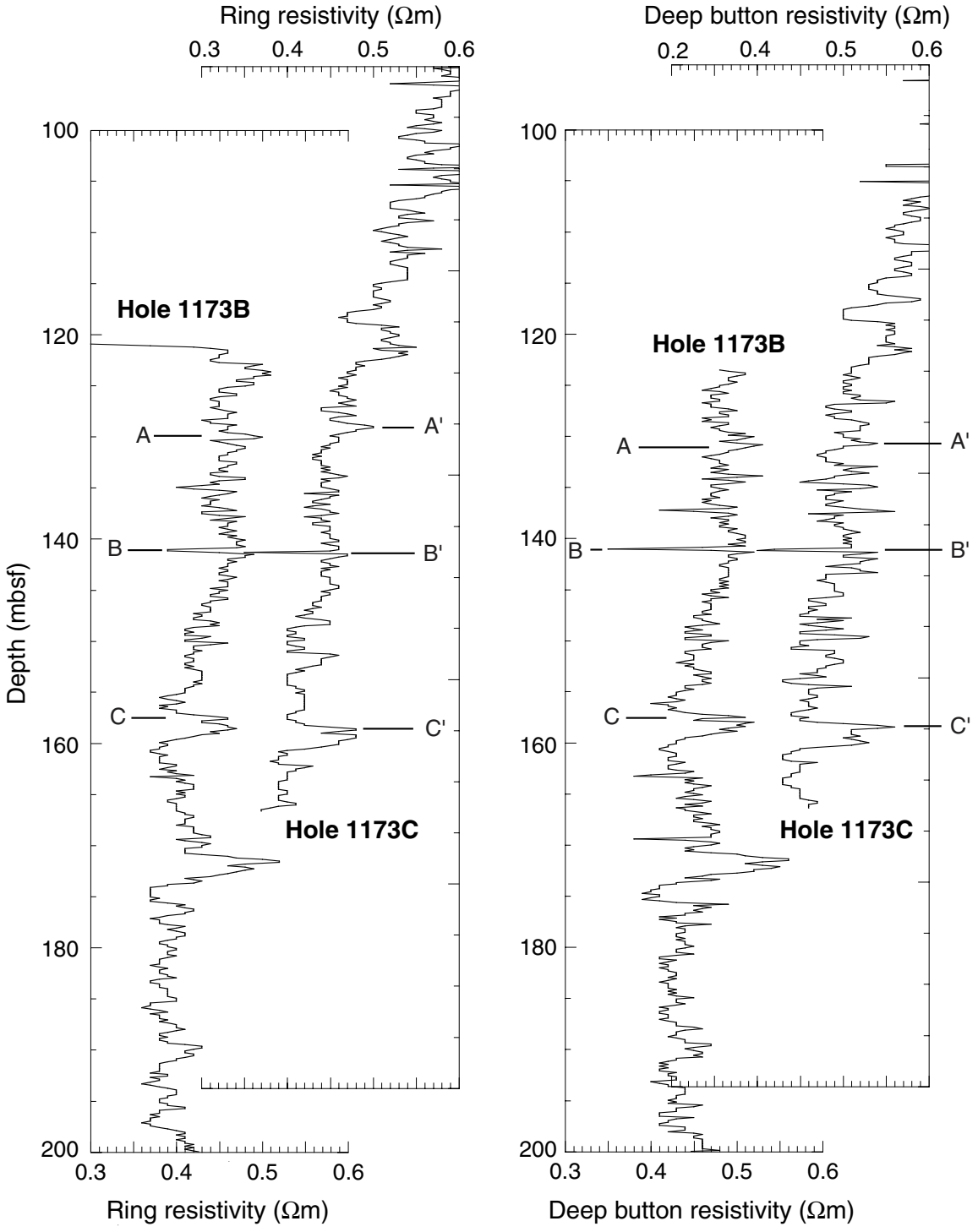

Figure F8. Visual interpretation of log units. Expanded-depth panels show changes in log trends in more detail.

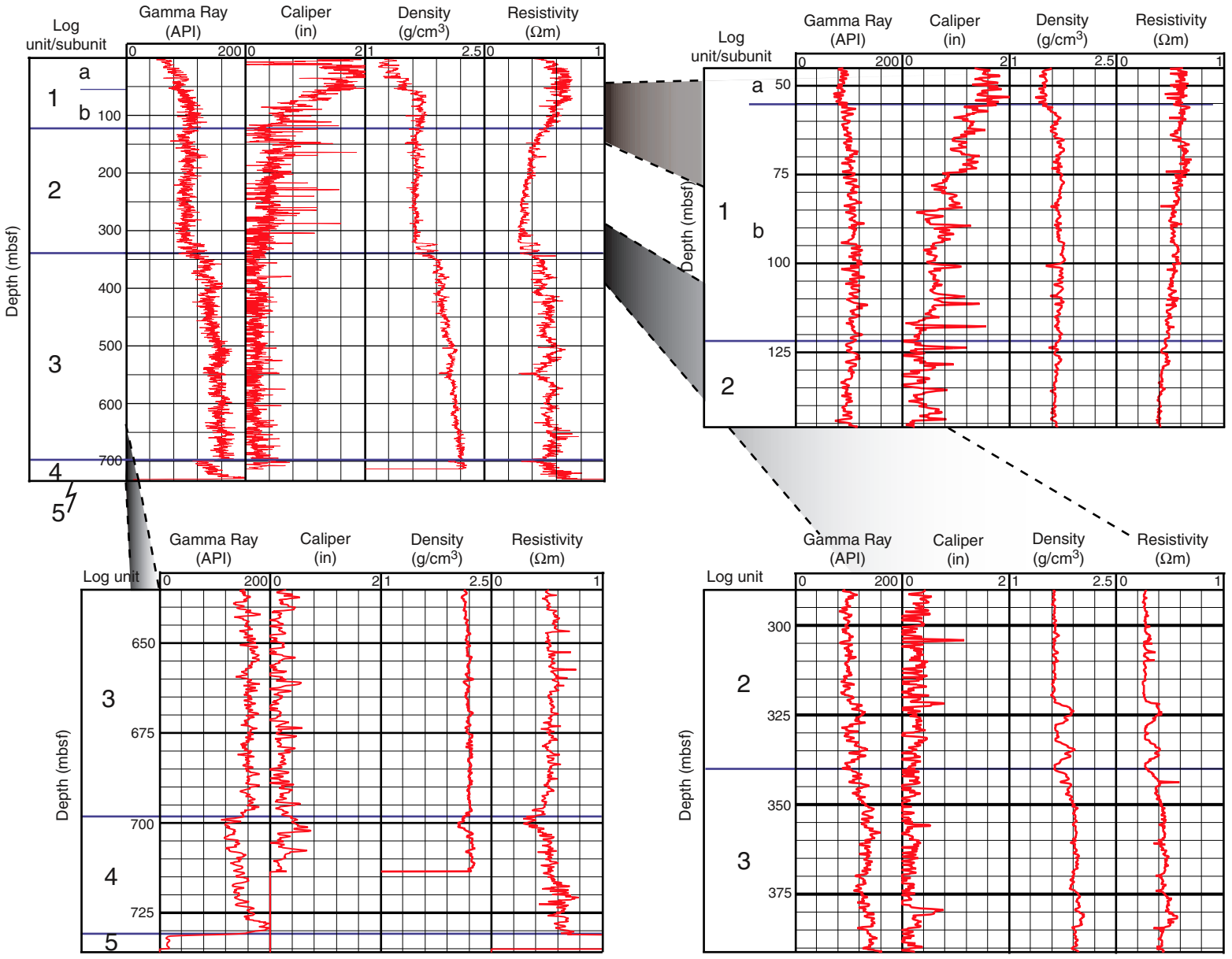

Figure F9. Definition of log units based on statistical analysis, Site 1173. Four clusters were derived from two factor logs, accounting for 76% of the total variance observed in the data. Each cluster describes a group with its specific physical properties. Boundaries between first-order log units correspond to changes in log character related primarily to lithology that are visible on the gamma ray, density, and resistivity logs. Second-order units represent subtle changes in log character.

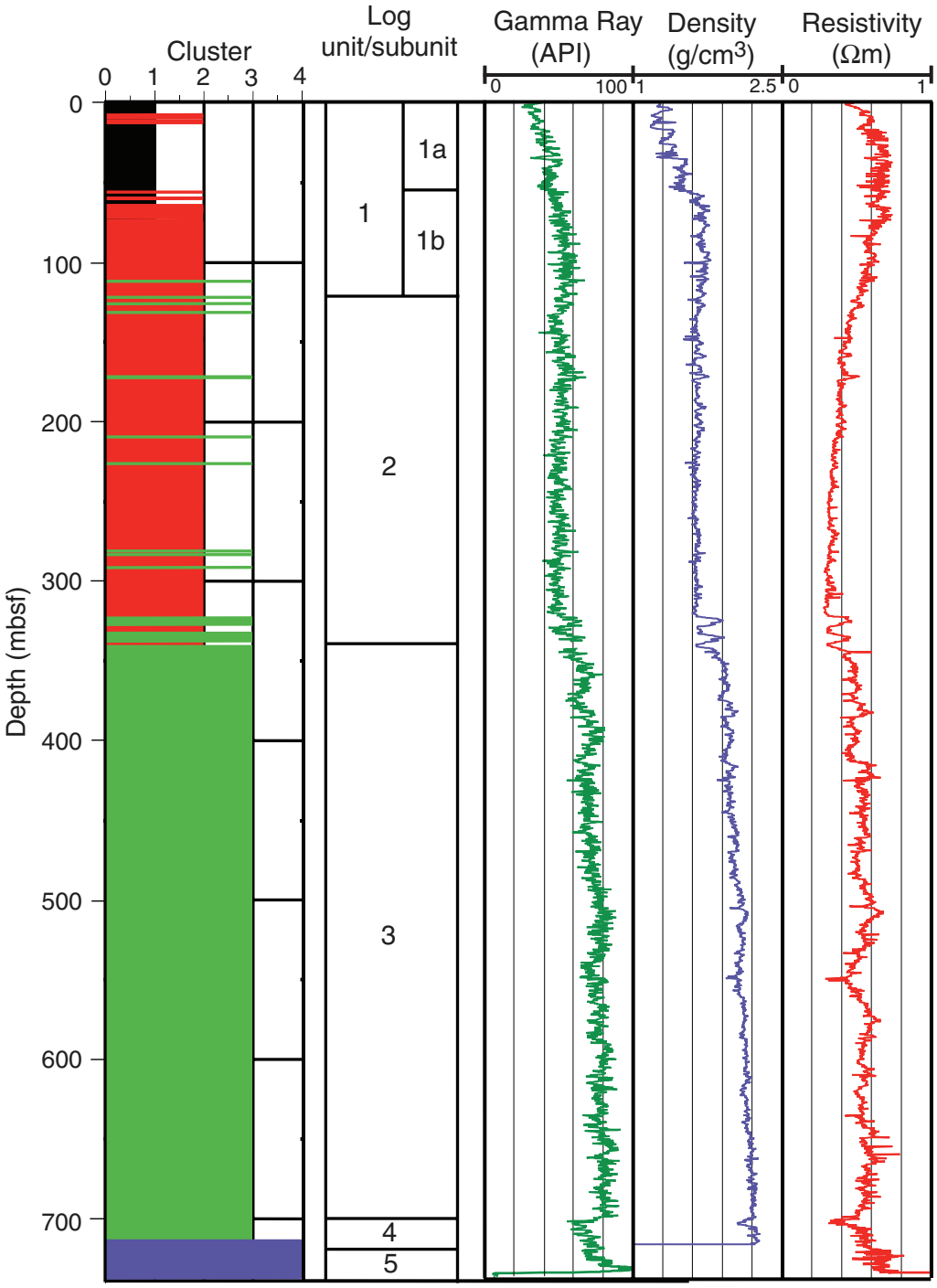

Figure F10. Statistical data for gamma ray, bulk density, resistivity, photoelectric effect, neutron porosity, and differential caliper logs for each log unit, Site 1173. The horizontal line within each box shows the median value of each parameter. The box boundaries are equivalent to the 25th and 75th percentiles of values. The error bars mark the 5th and 95th percentiles.

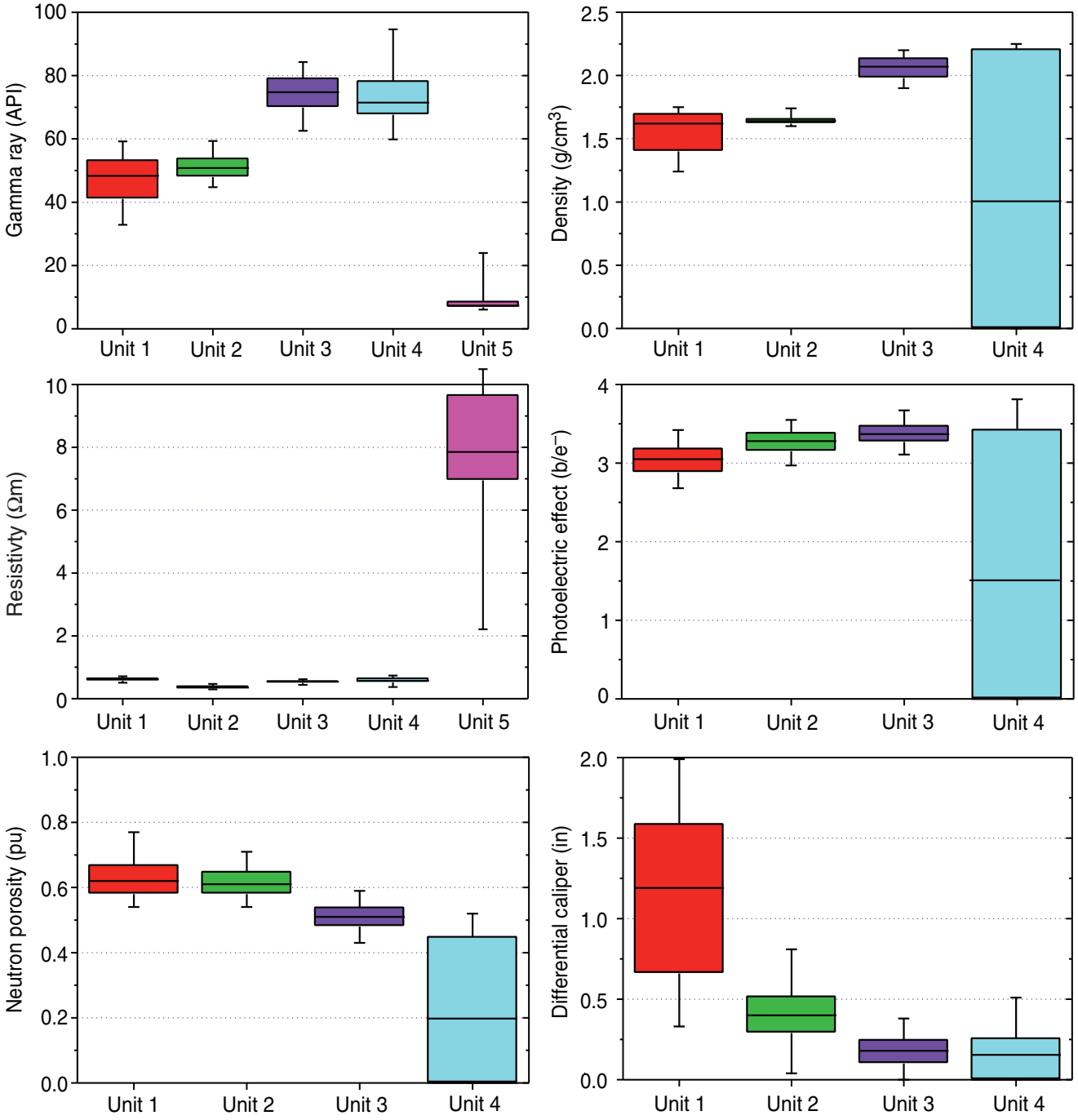

Figure F11. Crossplot of gamma ray vs. photoelectric effect. The colors for each log unit correspond to those used in Figure F10, p. 48.

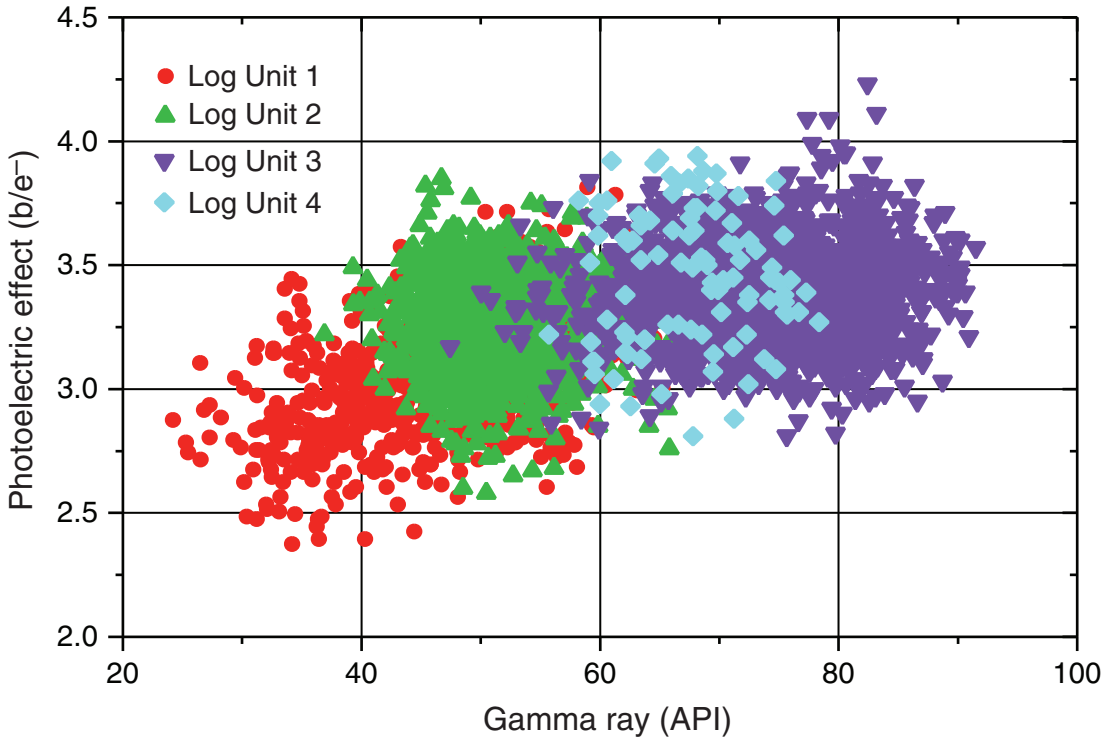

Figure F12. Summary of log and lithologic data, Site 1173. The lithology and X-ray diffraction (XRD) mineralogy columns reflect the major lithologic units of Hole 1173A (Moore, Taira, Klaus, et al., 2001). Blue and white marked areas in the log summary plot highlight the log units. PEF = photoelectric effect.

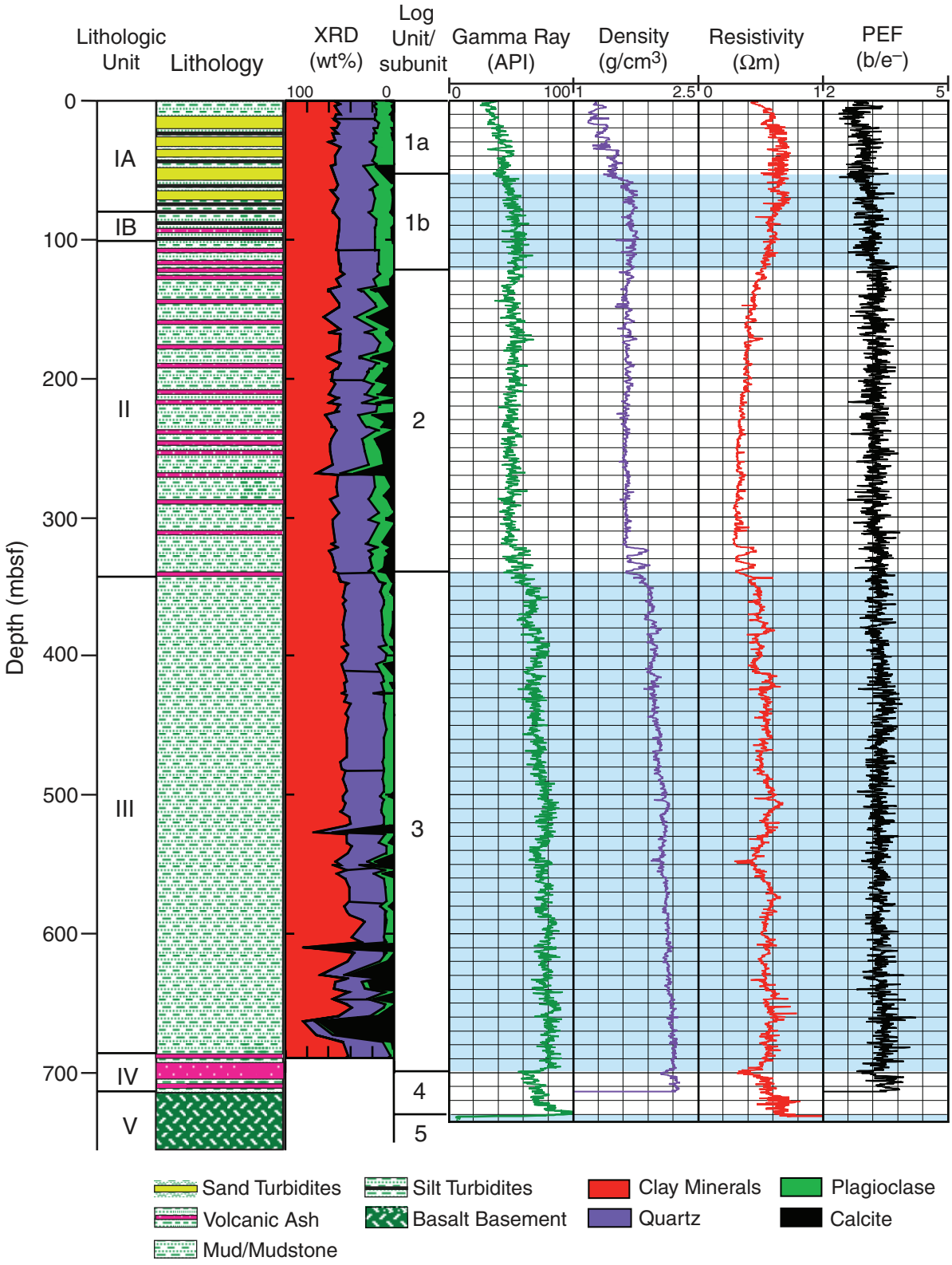

Figure F13. Examples of resistivity-at-the-bit images of different units, Site 1173. Images were processed using an equalized histogram over the entire hole. **A.** Image of well-stratified thinly bedded turbidites within lithologic Unit I (trench-wedge facies). Resistive (light) bands represent finer grained sediments (clays, silts), whereas conductive (dark) bands represent coarser grained sediments (sands, silts) at the base of turbidite beds. **B.** Image of hemipelagic muds of lithologic Unit II (upper Shikoku Basin facies) with conductive reduction spots indicative of bioturbation. **C.** Image of resistive volcanic ash layers within lithologic Unit II (upper Shikoku Basin facies). Vertical scale = 1:60, horizontal scale = 1:12.4.

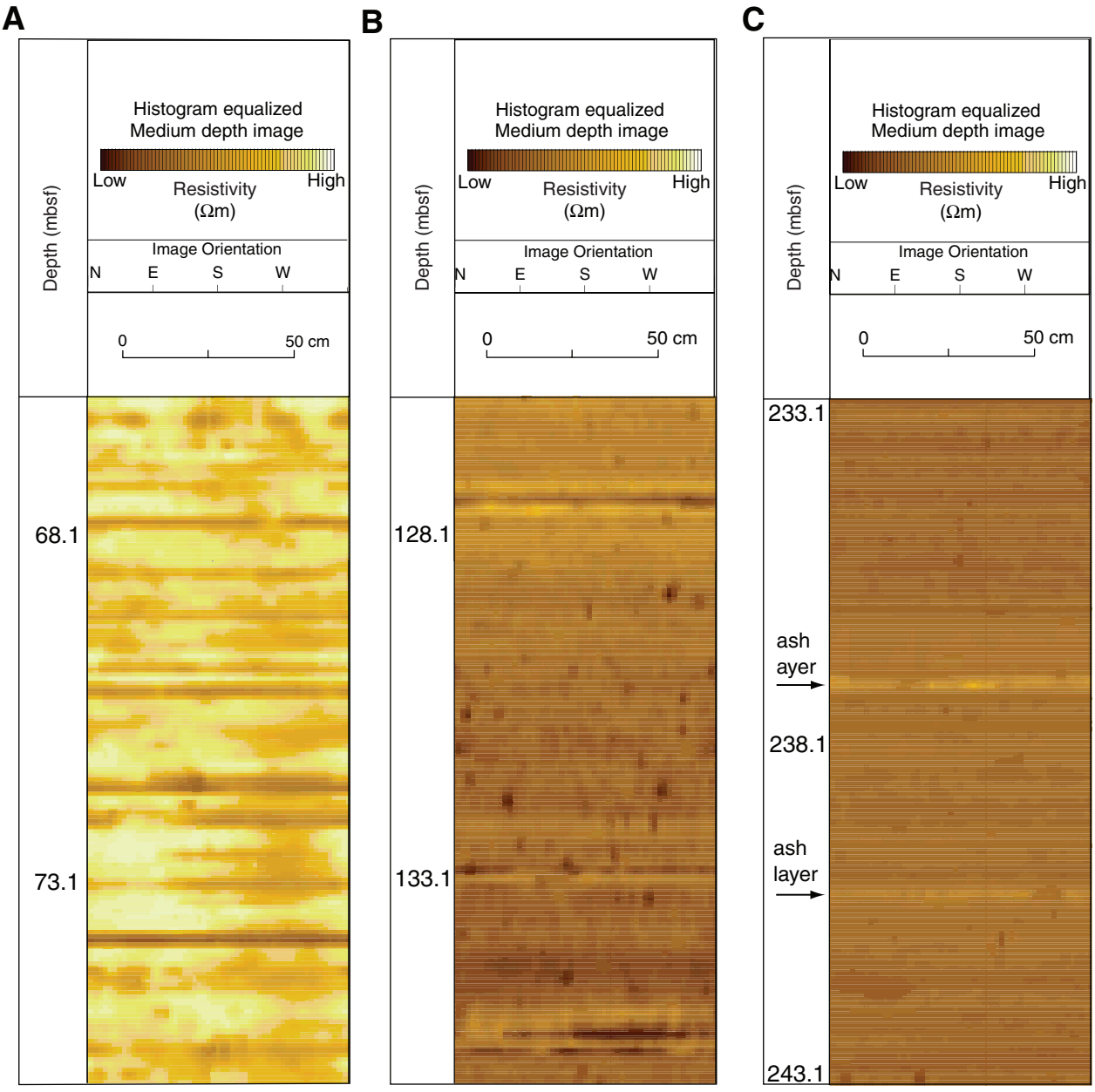

Figure F14. Composite figure of gamma ray, differential caliper, resistivity, and density logs and a resistivity-at-the-bit image of a turbidite section (0–125 mbsf).

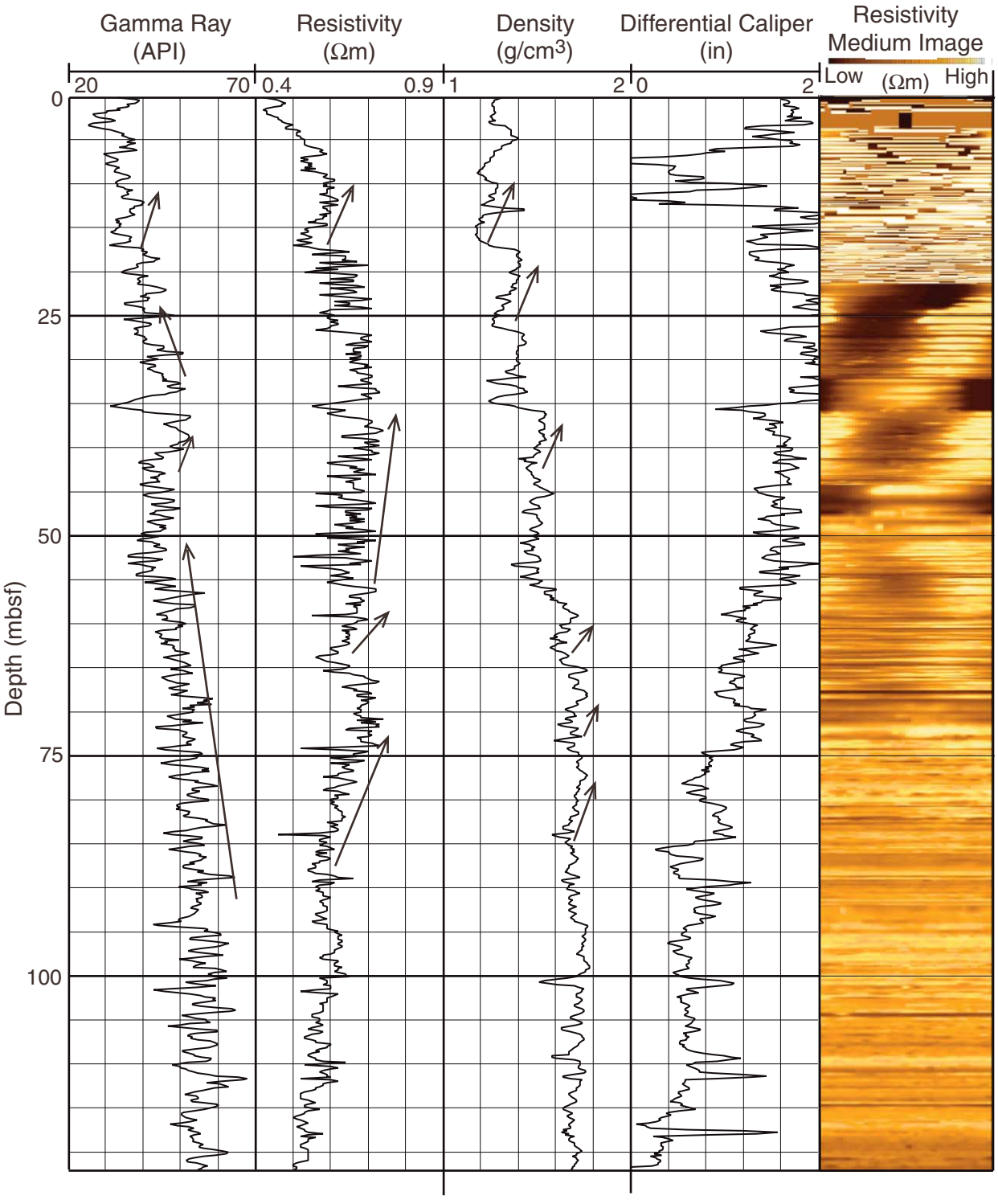

Figure F15. Composite figure of gamma ray, differential caliper, resistivity, and density logs and a resistivity-at-the-bit (RAB) image of the log Unit 2–3 transition (310–360 mbsf). The RAB image was added to show the thickness of sediment packages. The boundary between lithologic Units II and III is marked.

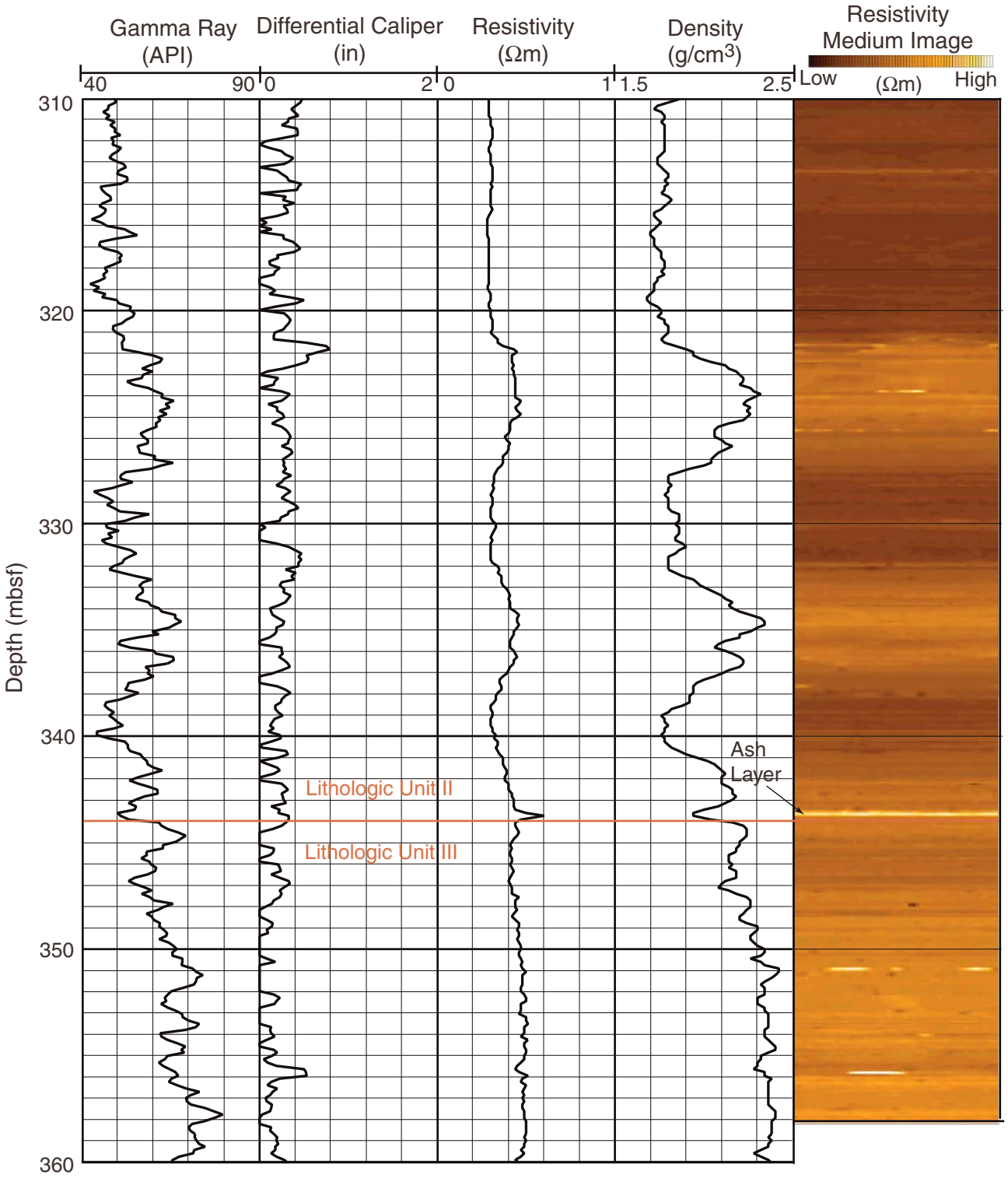

Figure F16. Composite figure of gamma ray, resistivity, density, photoelectric effect (PEF) logs and a resistivity-at-the-bit image of the volcaniclastic facies section (680–735 mbsf). The arrows show an upward coarsening trend of sediments between 700 and 728 mbsf and a fining-upward trend between 696 and 700 mbsf.

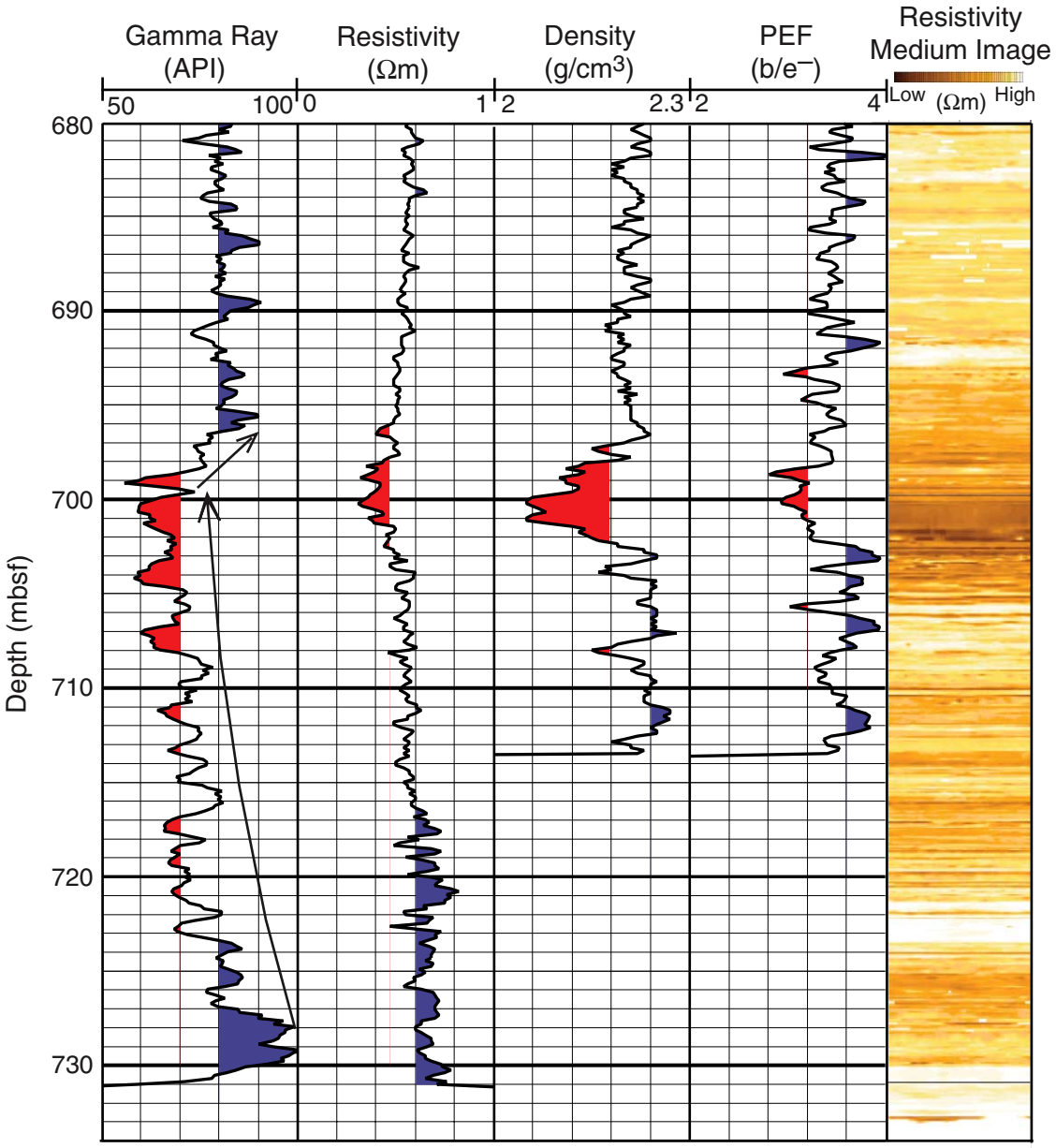

Figure F17. A. Bedding dips measured from resistivity-at-the-bit (RAB) data. Bedding dips are predominantly subhorizontal (0°–5°) with a slight increase in average dip below 370 mbsf. **B.** Comparison of bedding dip from Leg 190 core data (open circles) and Leg 196 logging-while-drilling RAB data (solid circles). Leg 196 apparent bedding dips are on average slightly lower, but changes in average dip are common to both data sets and any discrepancy may be a function of differences in resolution and methods.

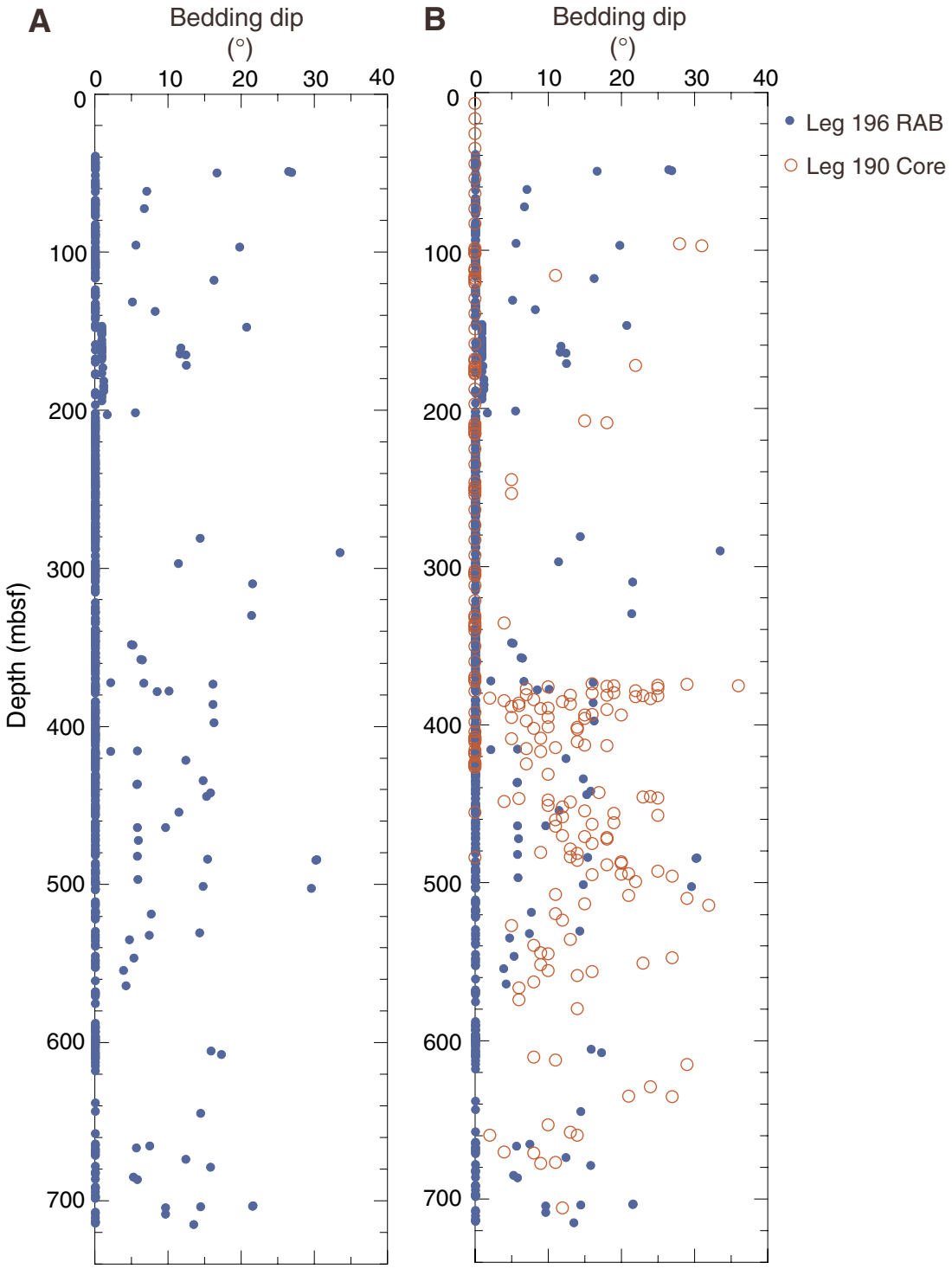

Figure F18. Fracture (**A**) dip and (**B**) strike from resistivity-at-the-bit image interpretation. Fracture strike is plotted so that the dip direction is 90° counterclockwise from the strike. An increase in fractures occurs between 380 and 520 mbsf. Orientations appear to be randomly distributed. Note the two zones of fracturing (378–384 and 410–417 mbsf) and the zone of high-resistivity bands (~500 mbsf) associated with intensive deformation, possibly brecciation. The shallower zone of fracturing (378–384 mbsf) may correlate with a fractured zone recorded in the cores of Leg 190 Hole 1173A (382–384 mbsf) but the deeper zone has no such correlation. A steeply dipping fracture would not be expected to correlate at the same depth between two holes spaced 50 m apart, unless it represented part of a subhorizontal zone of high-angle fractures.

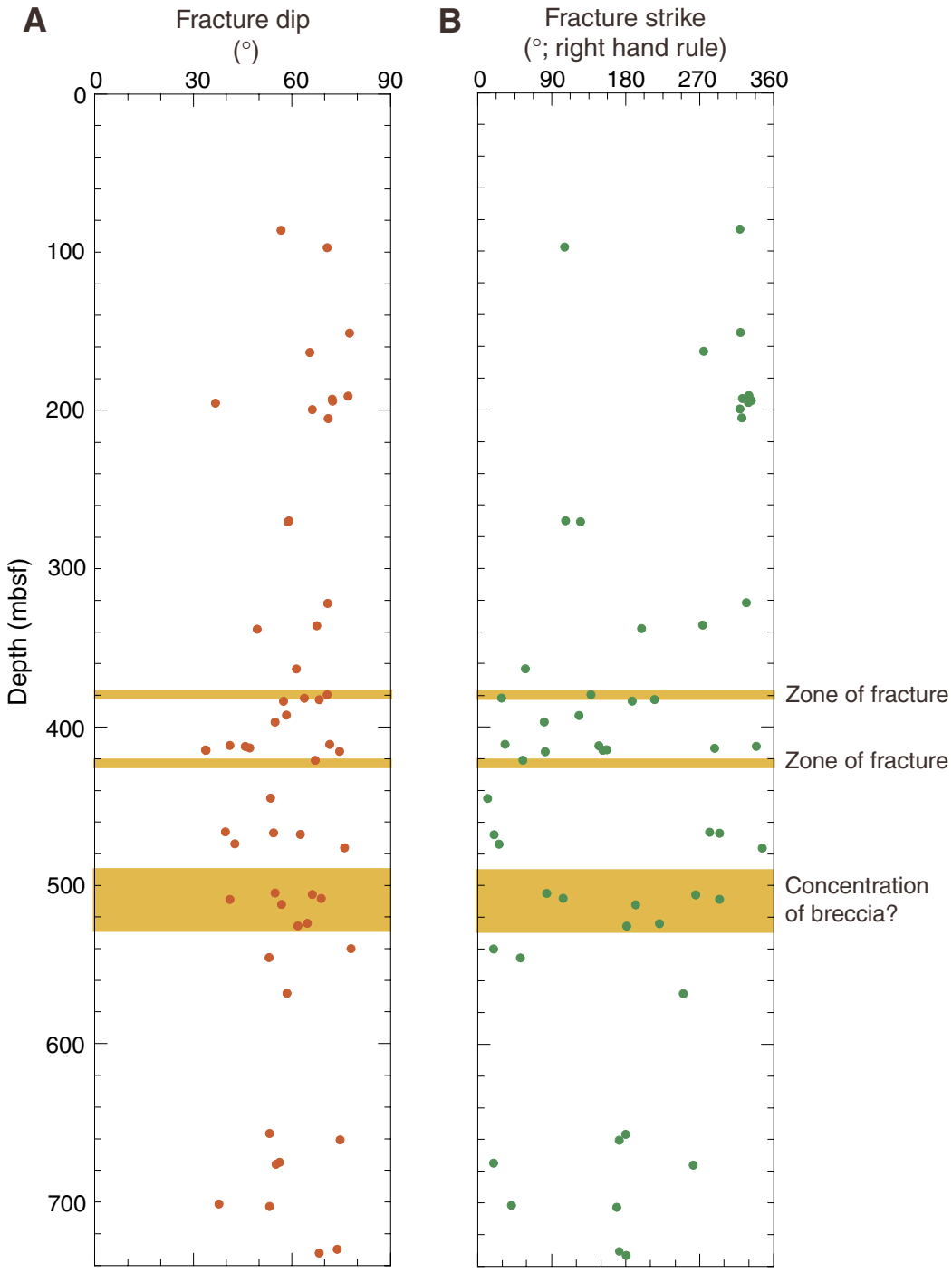

Figure F19. A. Resistivity-at-the-bit (RAB) image of fractures at ~410 mbsf (Hole 1173B) cutting subhorizontal stratigraphy. Figure shows uninterpreted RAB image (left), interpreted RAB image (center), and fracture dip and orientation data (right). The fractured zone is generally more resistive than overlying and underlying sediments. The fracture at 415 mbsf (indicated by arrow) displaces a subhorizontal conductive (dark) bed with normal offset. **B.** RAB image of fracture at 321 mbsf cutting subhorizontal high-resistivity ash layer. Resolution of original RAB image data far exceeds output resolution shown here. Images processed with equalized histogram over the entire hole (static normalization).

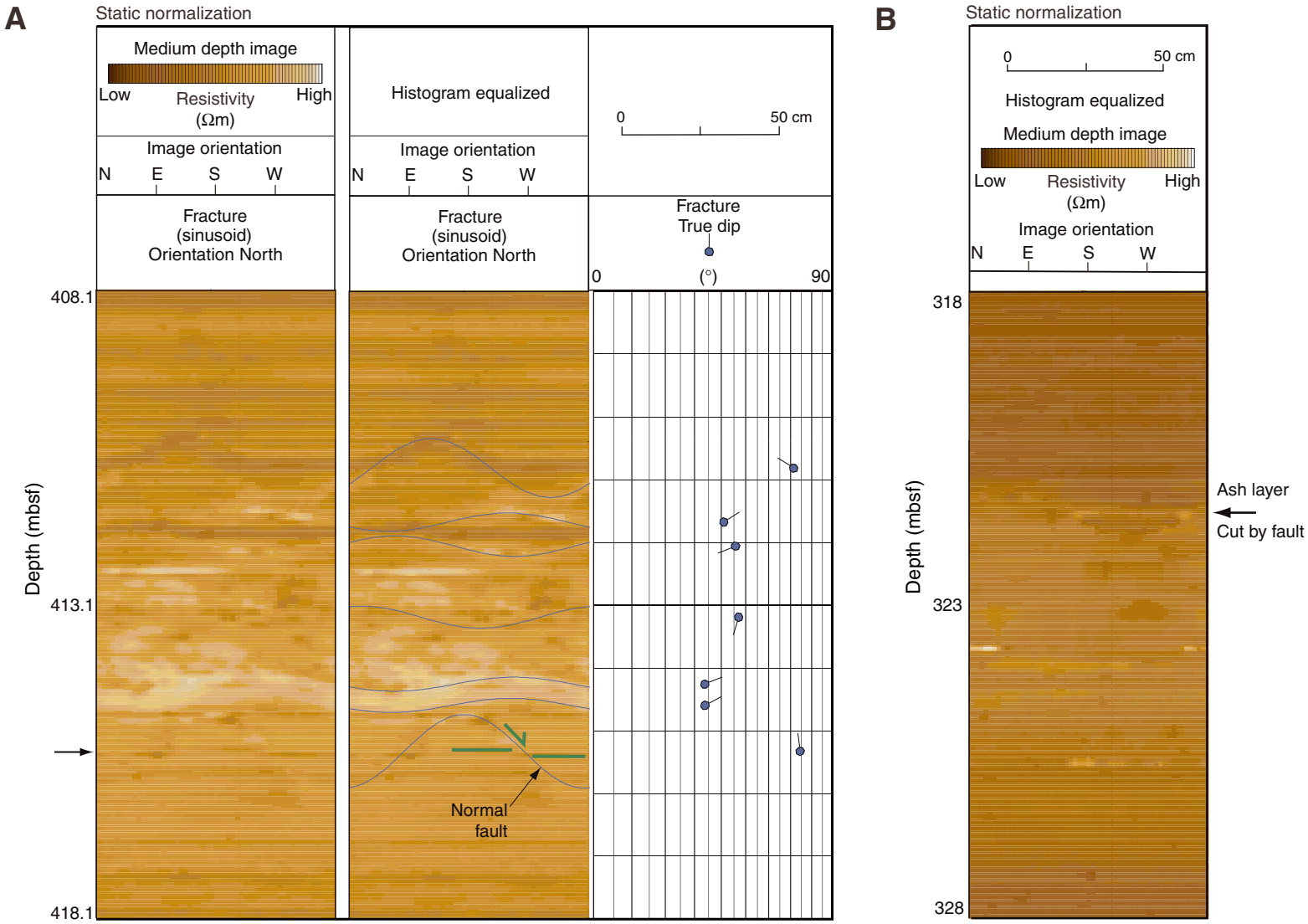

Figure F20. Stereographic plot of poles to fault planes (equal-area lower-hemisphere projection), Site 1173. No apparent trend in strike is observed.

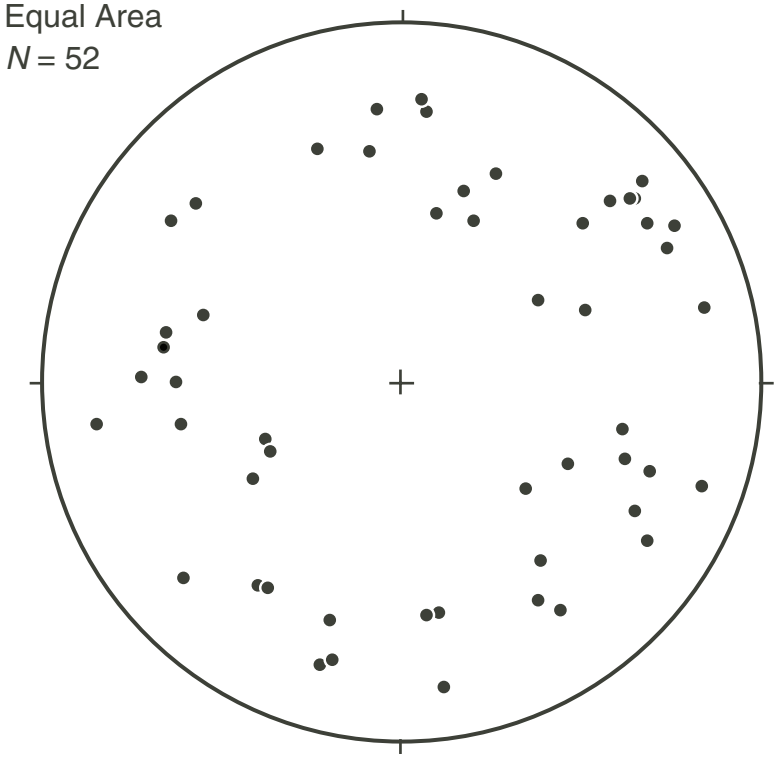

Figure F21. Resistivity-at-the-bit image (dynamic scaling) of basaltic basement at the base of Hole 1173B. Image shows a near-vertical conductive contact (indicated by green arrows) just below the contact between volcaniclastics and basalt. The conductive feature is interpreted as a drilling-induced borehole breakout. This feature is cut by two high-angle fractures (73° and 68° dips; blue sinusoids). Fracture information is given as dip and dip azimuth.

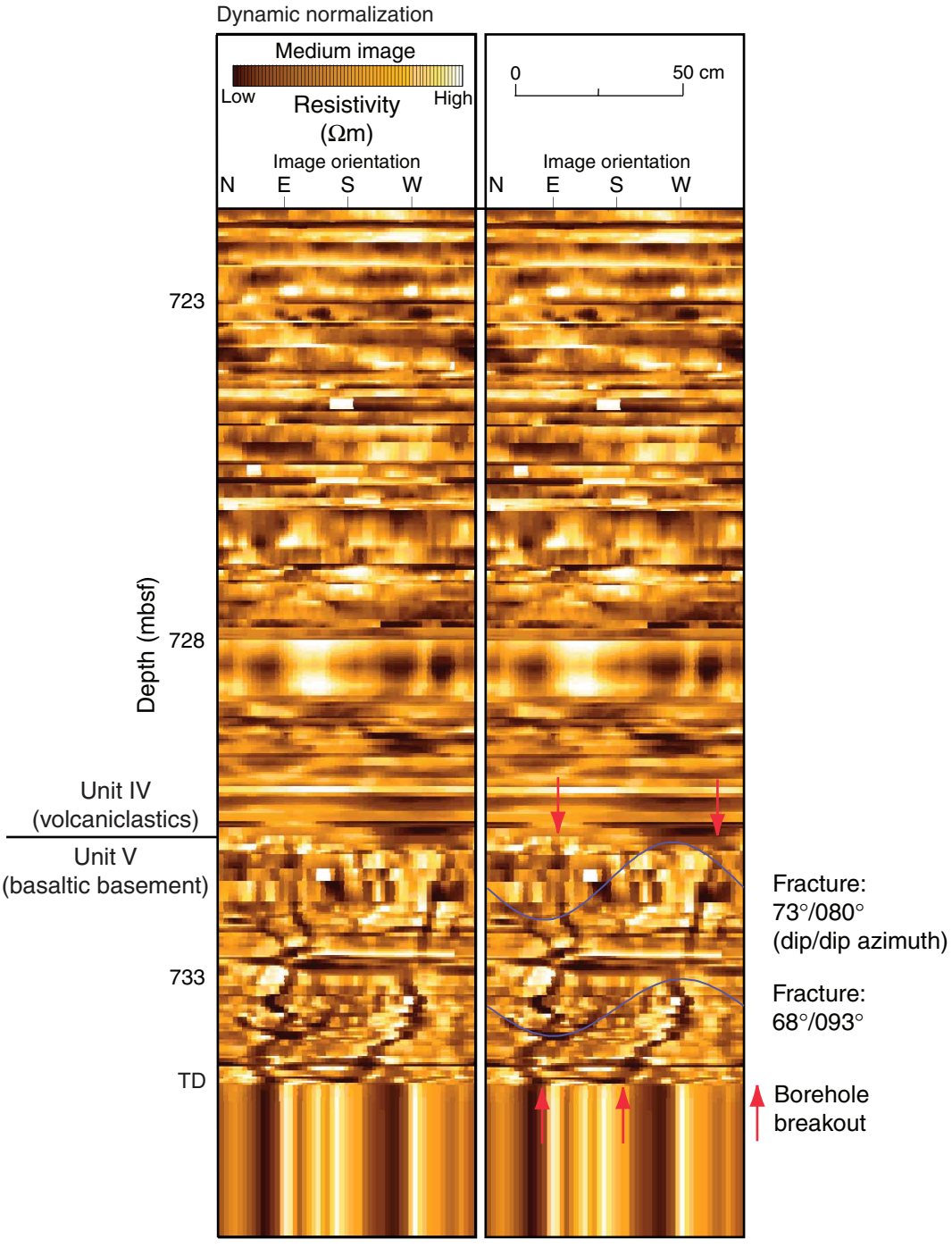

Figure F22. Logging-while-drilling (LWD) density (RHOB) profile from Holes 1173B and 1173C compared to bulk density values from Hole 1173A cores.

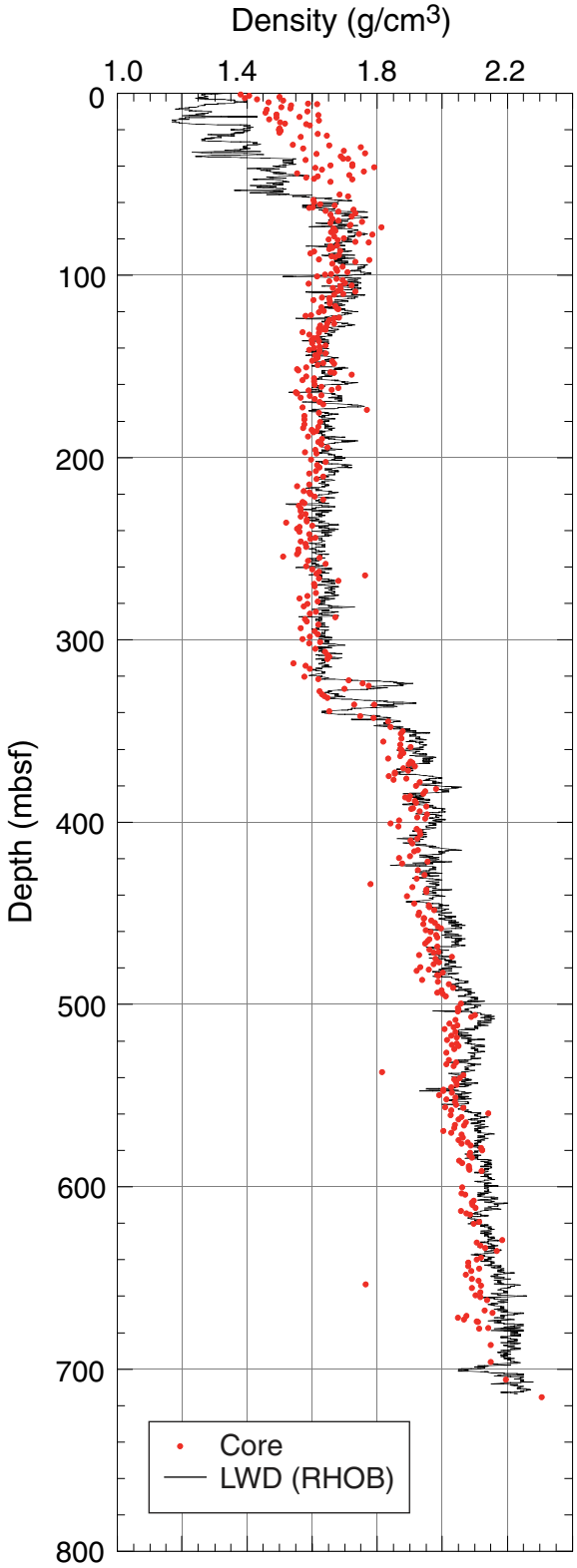

Figure F23. Least-squares regression fits (dashed lines) of grain density values from Hole 1173A cores. The upper to lower Shikoku Basin facies transition is at 344 mbsf.

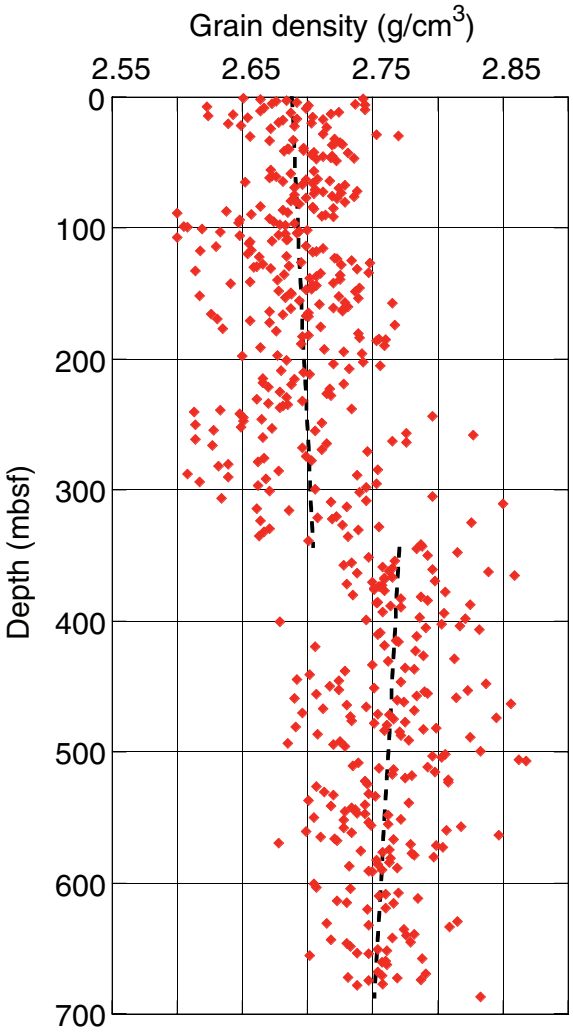

Figure F24. Porosity calculated from the Hole 1173B and 1173C logging-while-drilling (LWD) density (RHOB) log using the least-squares regression fit of grain density values from Hole 1173A (see Fig. F23, p. 61), compared to porosity measurements from Hole 1173A cores.

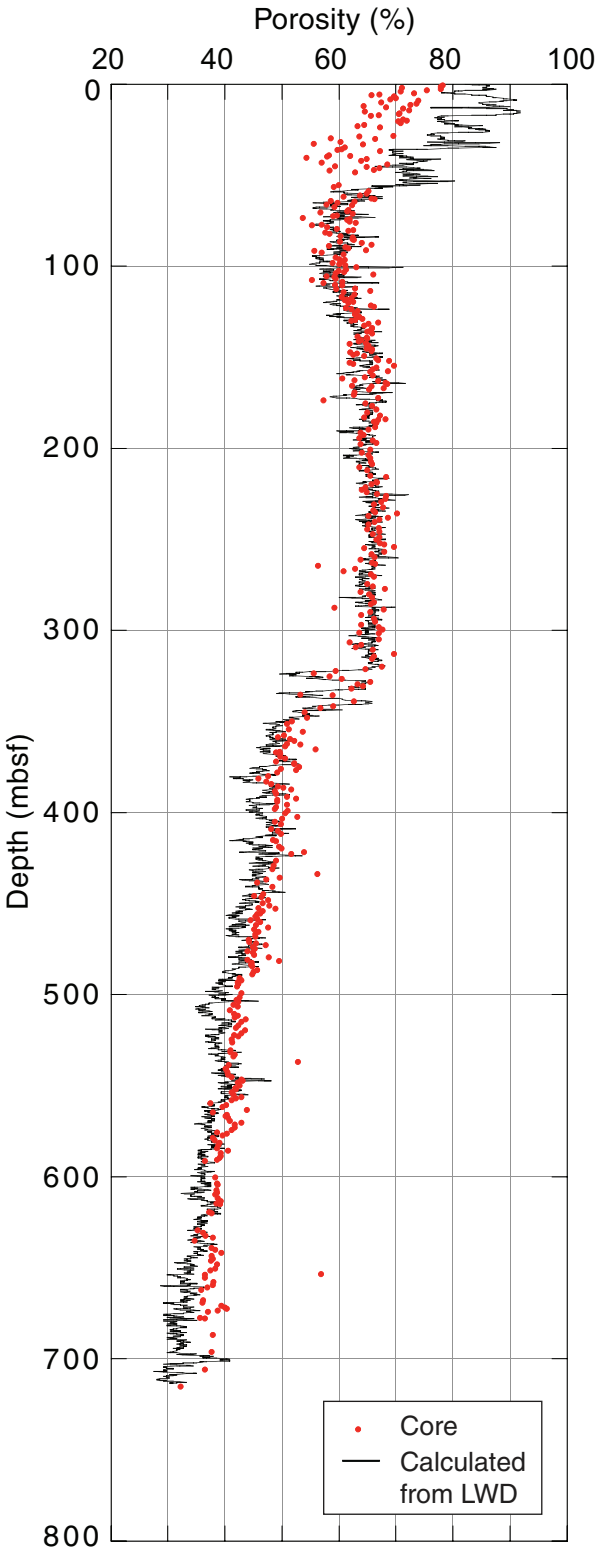

Figure F25. Comparison of differential caliper and logging-while-drilling density in the upper 100 m of Hole 1173C. Horizontal lines indicate intervals discussed in the text.

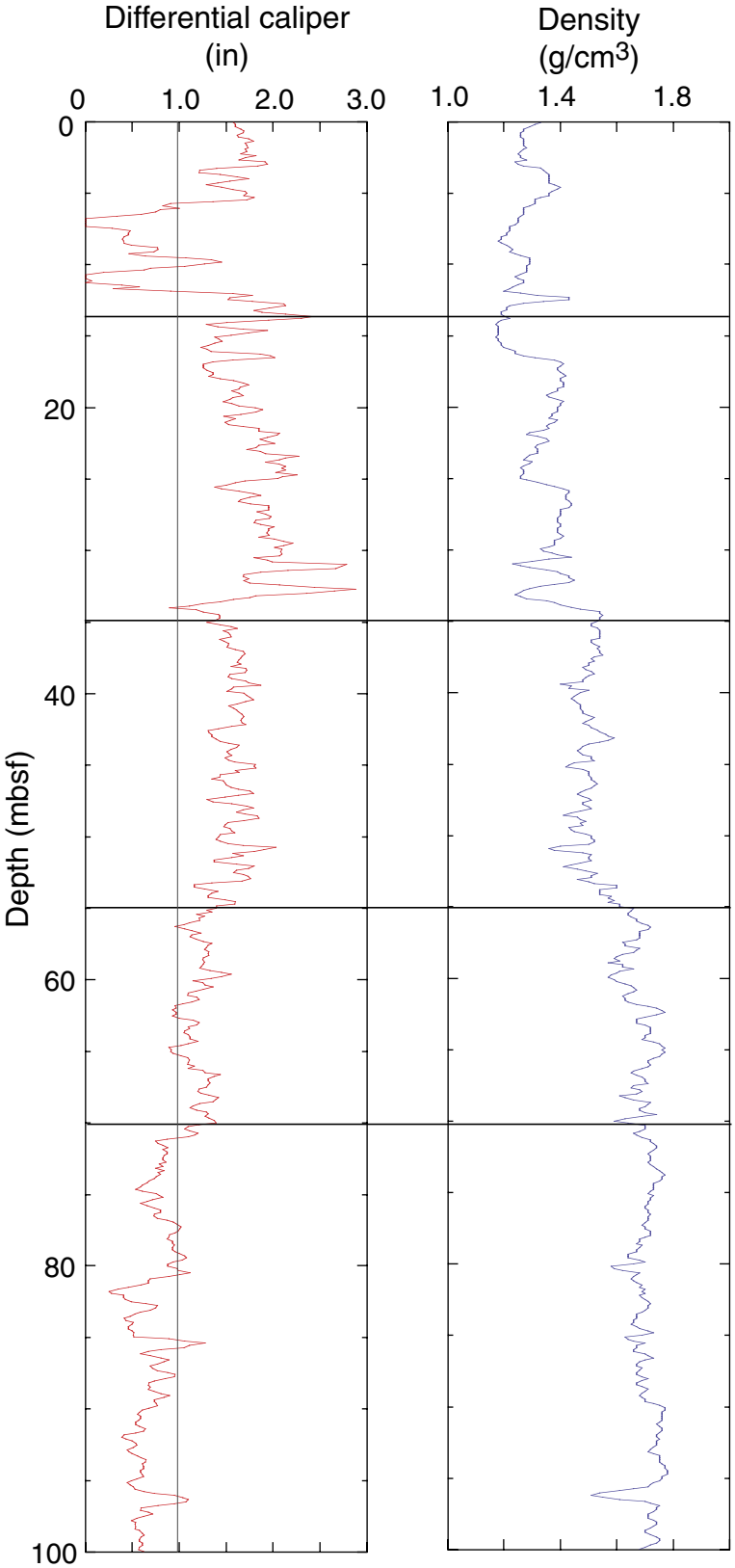

Figure F26. A. Hole 1173C logging-while-drilling (LWD) density (RHOB) and Hole 1173A core bulk density values for the upper 100 m. The superimposed logarithmic curve was calculated based on core bulk densities. **B.** Porosity calculated from the LWD density, Hole 1173A core porosities, and logarithmic porosity.

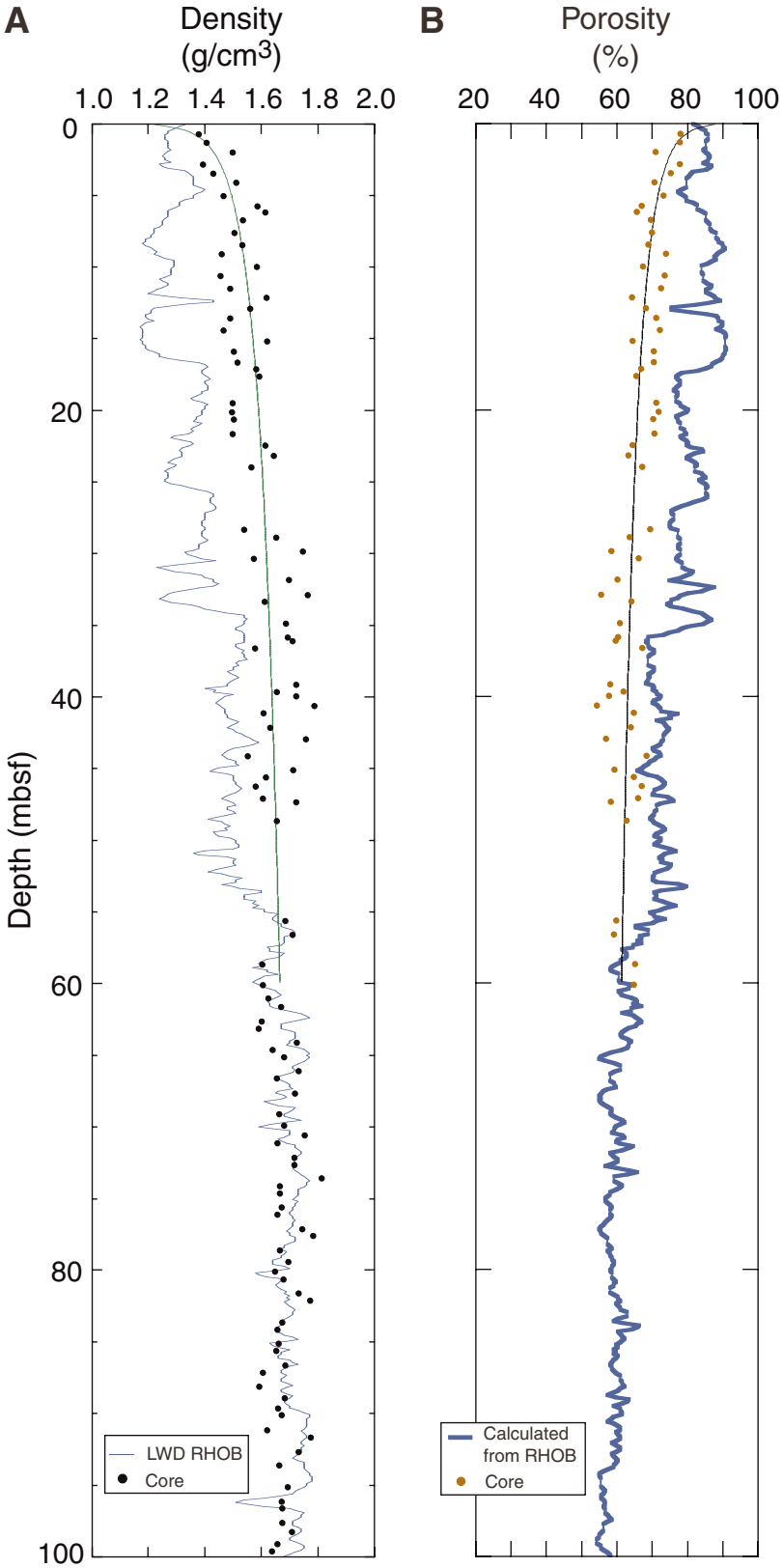

Figure F27. Five resistivity logs acquired with the resistivity-at-the-bit tool. Lines separate log Units 1–4. The horizontal scale was chosen to emphasize the variations of resistivity in the upper 730 m but excludes the high resistivity values of the basement, which are shown in Figure F28, p. 66.

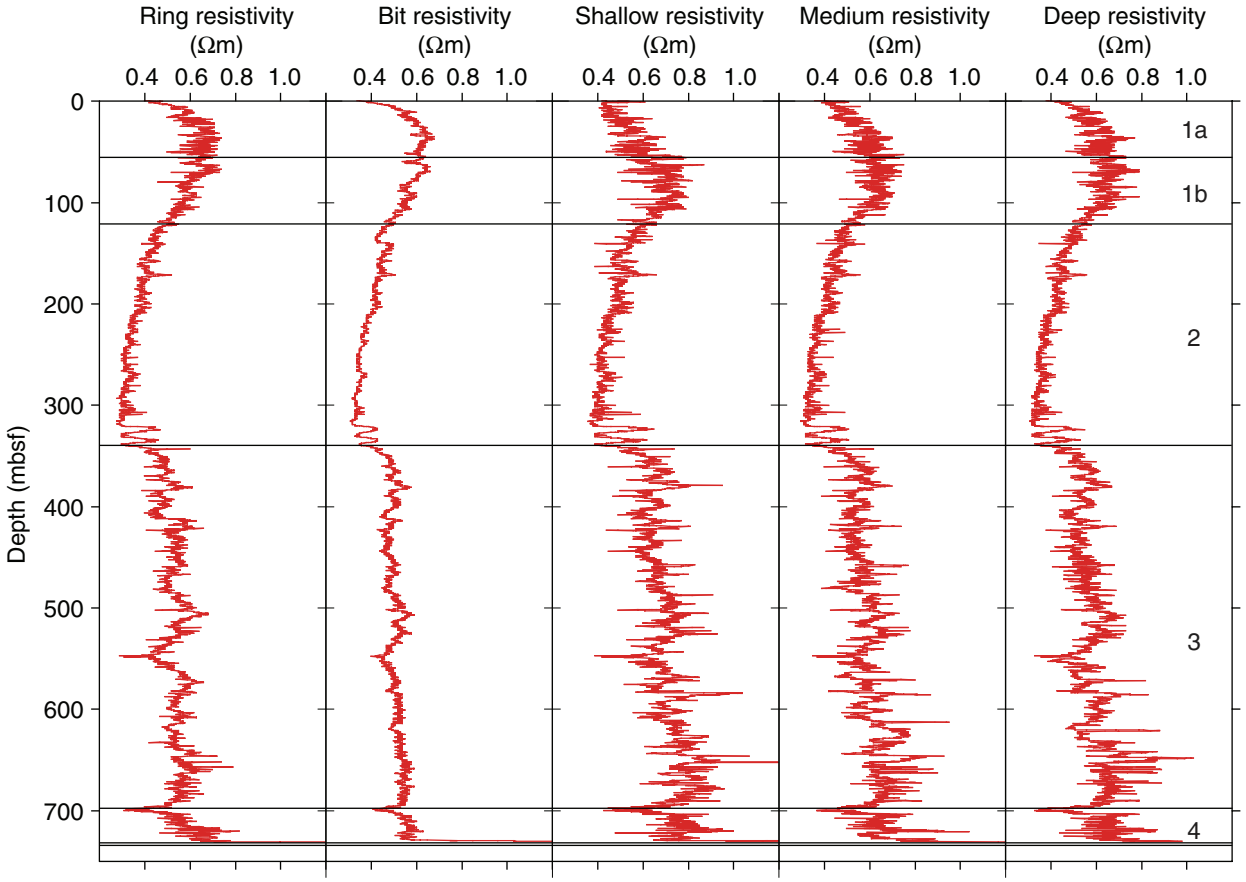

Figure F28. Resistivity logs for basement log Unit 5.

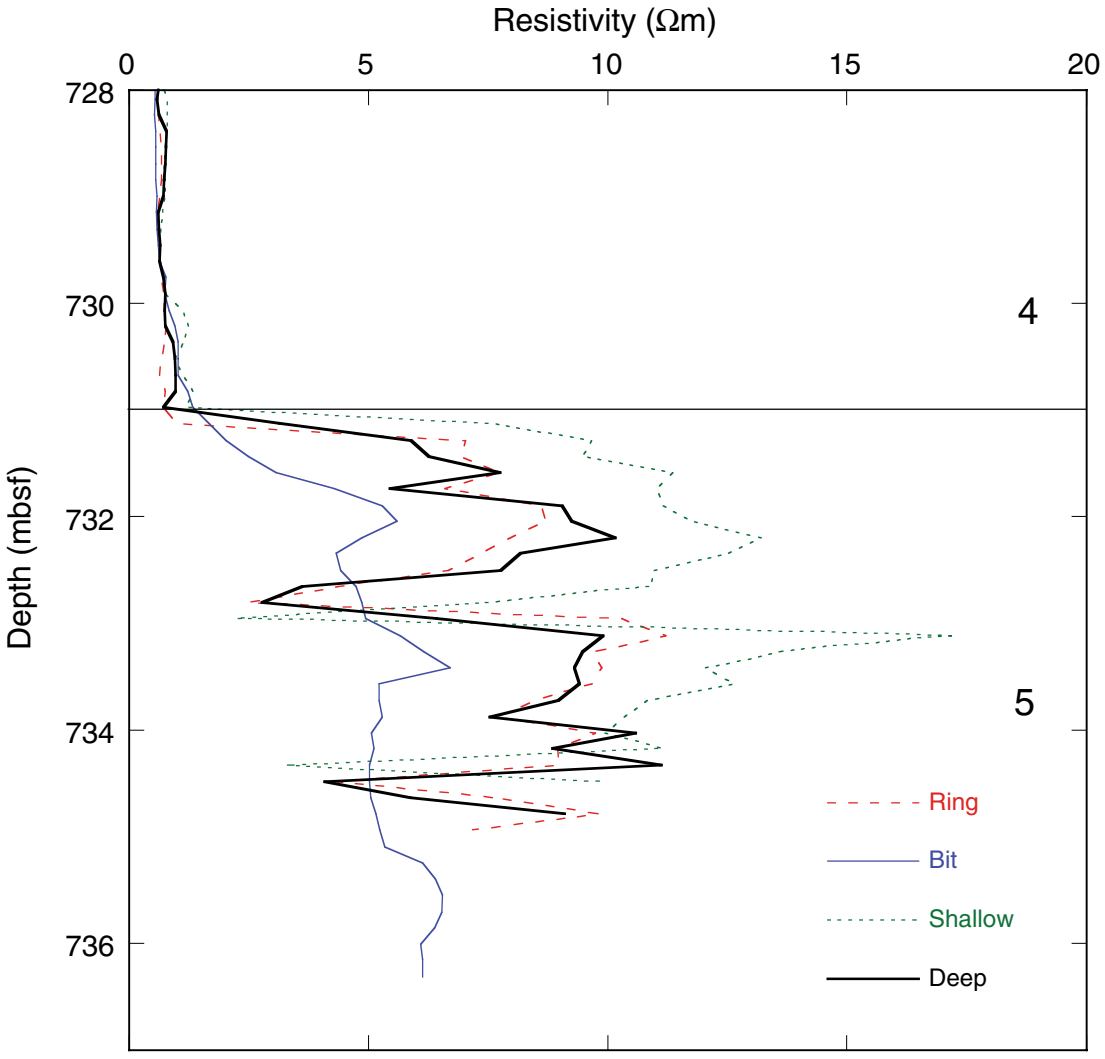

Figure F29. A. Ring and bit resistivity acquired with the resistivity-at-the-bit (RAB) logging-while-drilling (LWD) tool and Leg 190 shallow resistivity acquired with the wireline (DIT) tool. **B.** Shallow-, medium-, and deep-focused button resistivity acquired with the RAB tool. Lines separate log Units 1–4.

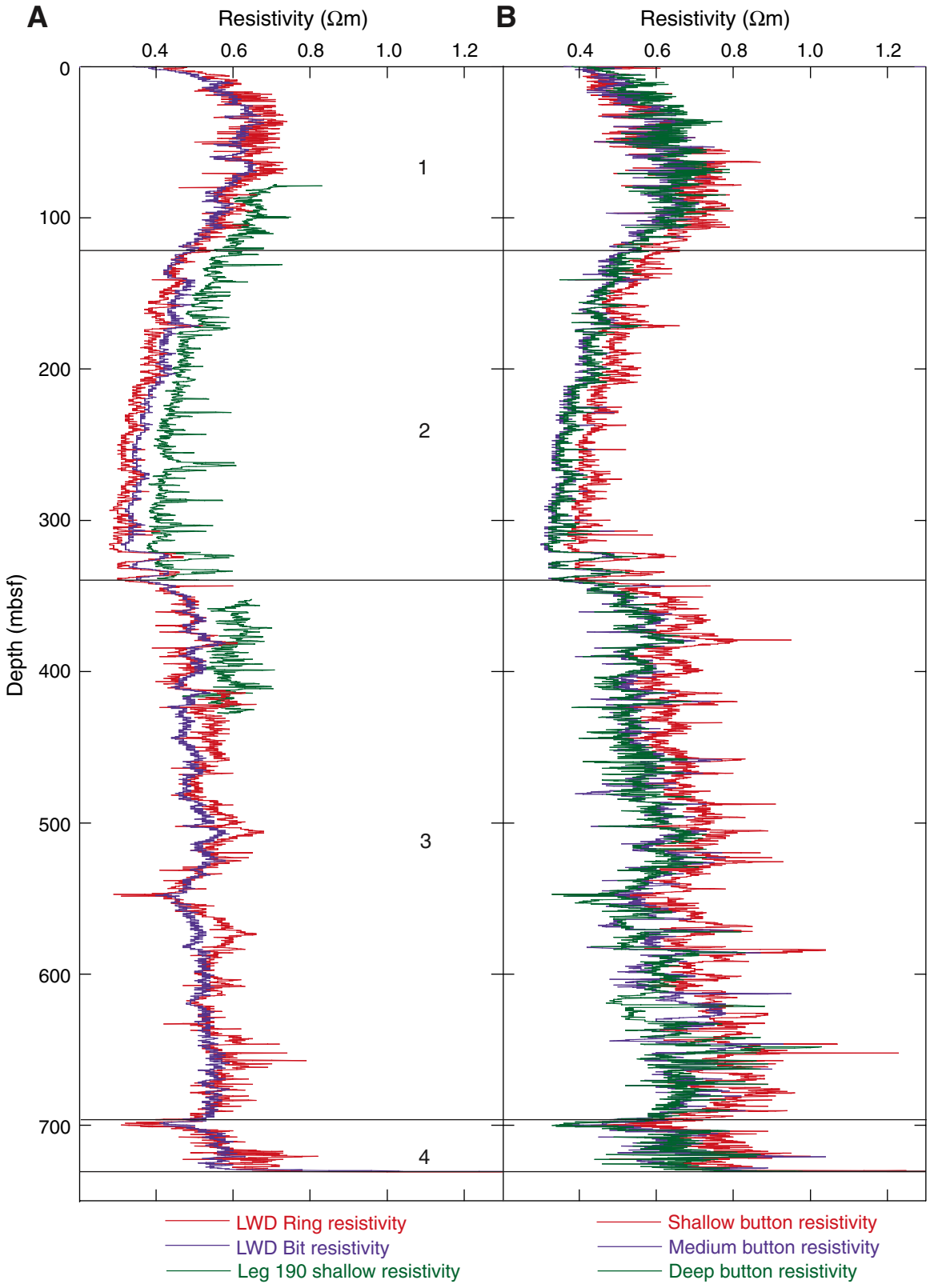

Figure F30. Correlation diagrams of (**A**) deep vs. medium resistivity, (**B**) deep vs. shallow resistivity, (**C**) ring vs. bit resistivity, and (**D**) deep vs. ring resistivity. On each plot, the black line is the line of unit slope passing through the origin and the red line is the linear fit to the data. Equations describe the least-squares regression curves and *R* is the correlation coefficient.

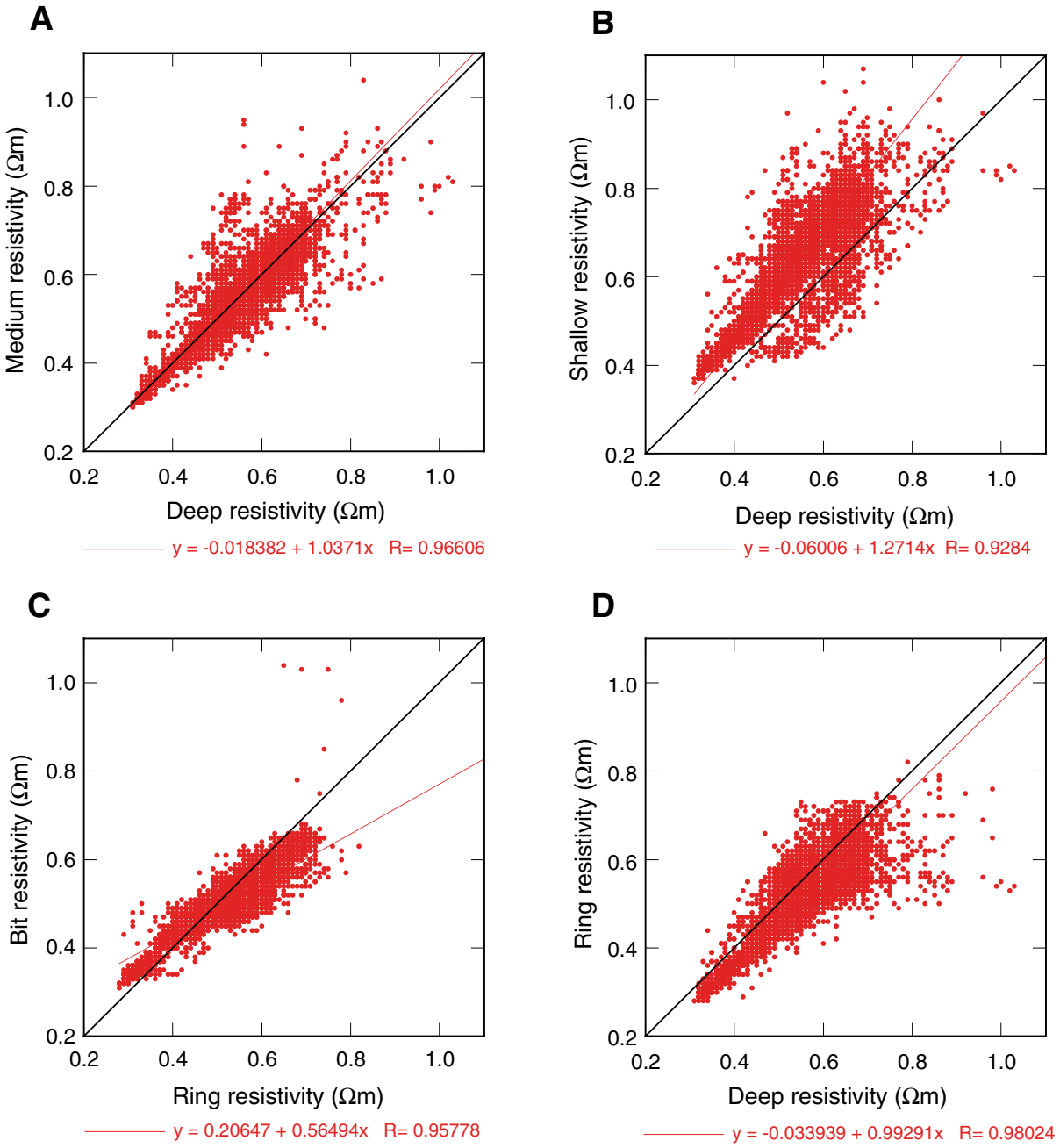

Figure F31. A. Logging-while-drilling porosity (TNPH), core, and RHOB-derived porosity. Lines separate log Units 1–4. **B.** Difference between neutron and calculated porosity (differential porosity).

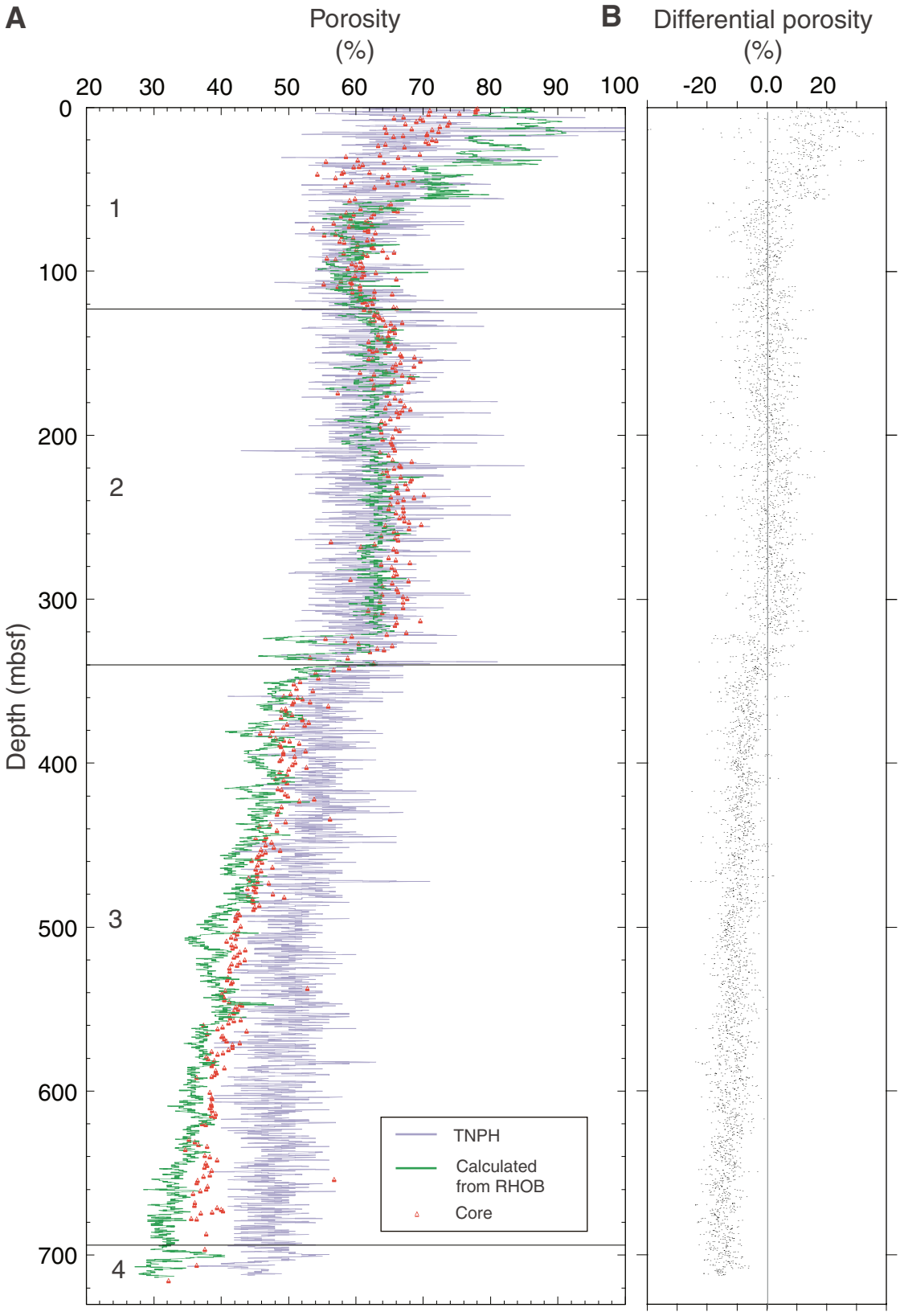

Figure F32. Hole 1173B IDEAL sonic-while-drilling *P*-wave velocity profile compared with Hole 1173A wireline log and core velocity measurements. Note that Hole 1173B is cased to 120.9 mbsf.

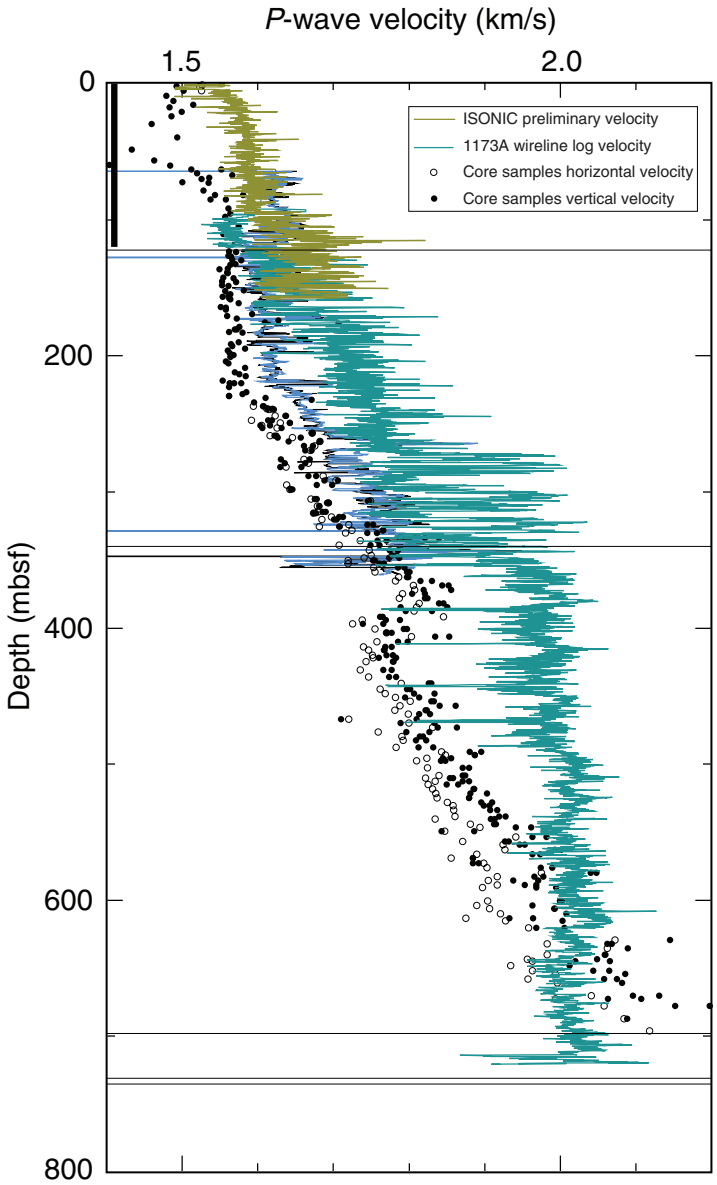

Figure F33. Summary of synthetic seismogram analyses, Site 1173. **A.** Two-way traveltime (TWT) vs. depth relationship. **B.** Density and velocity curves where velocity is shown as slowness (inverse of velocity). **C.** Modeled source wavelet. **D.** Reflection coefficient. **E.** Common depth midpoints (CMPs) 237–256 from Inline 215 with the synthetic seismogram displayed in the center as three identical traces. CMP spacing = 25 m.

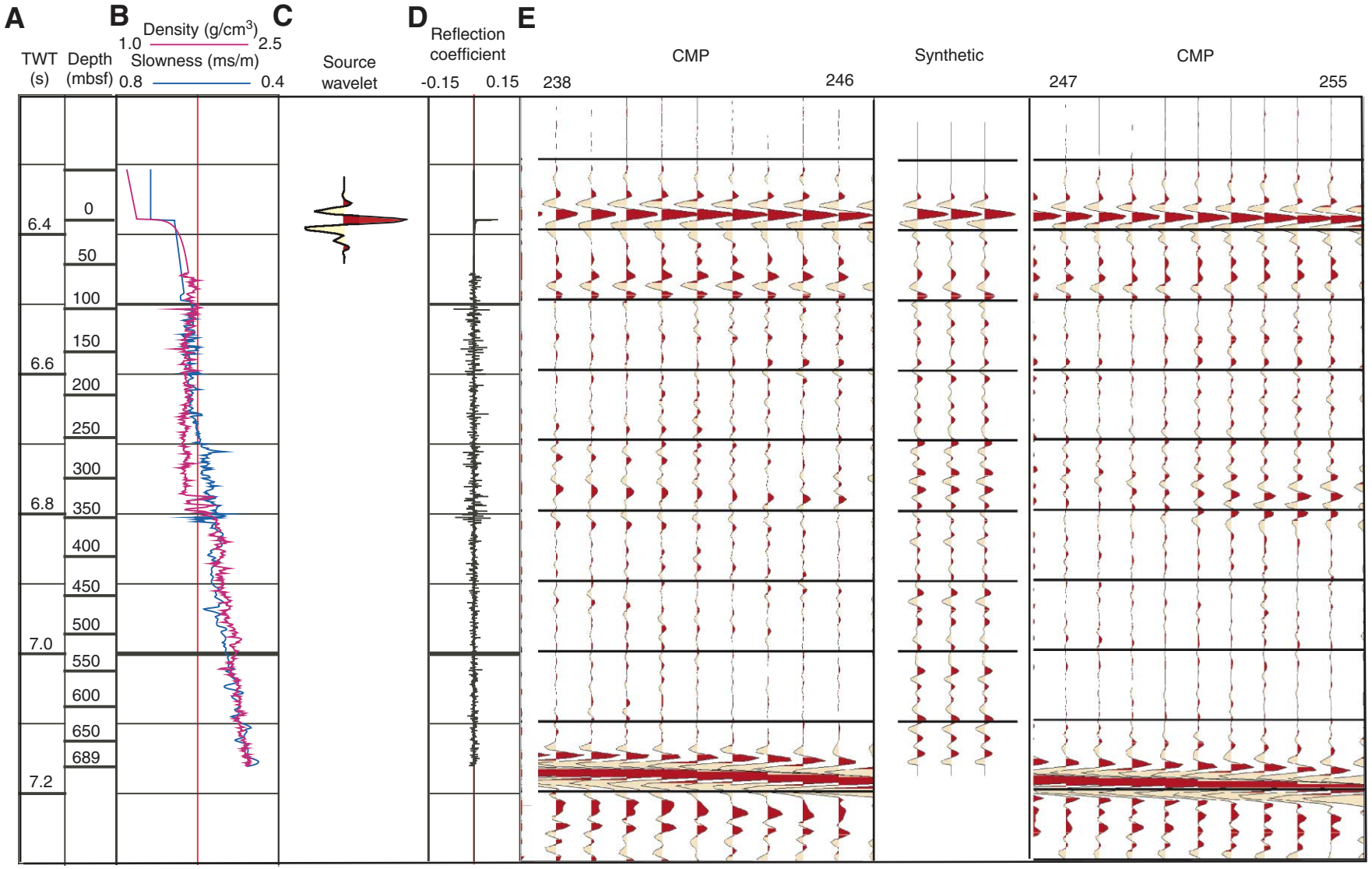

Figure F34. Video of the reentry of the Advanced CORK (ACORK) at Hole 1173B with the rotary core barrel bottom-hole assembly. Note that the ACORK head extends ~2–3 m above the remotely operated vehicle platform visible in the main reentry cone. (QuickTime software is available for the Macintosh and Windows platforms only. Please see **"QuickTime Movies"** in 196IR.PDF for further information. Click the image to play the movie.)

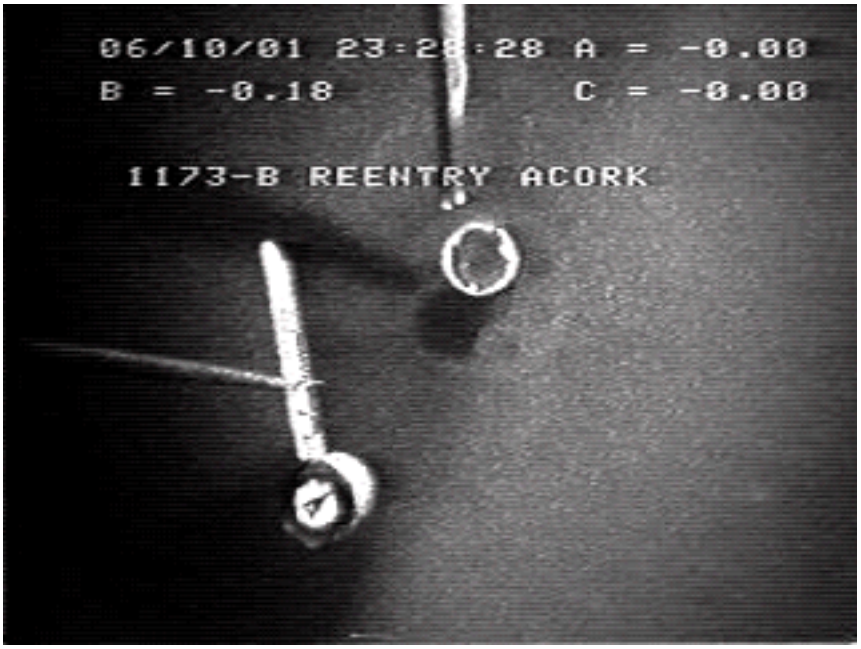

Figure F35. Video inspection of the completed Advanced CORK (ACORK) installation in Hole 1173B. The end of the drill pipe, which broke off after the premature setting of the bridge plug, is visible in the center of the small ACORK reentry cone. Otherwise, the ACORK appears to be in excellent condition. (QuickTime software is available for the Macintosh and Windows platforms only. Please see **"QuickTime Movies"** in 196IR.PDF for further information. Click the image to play the movie.)

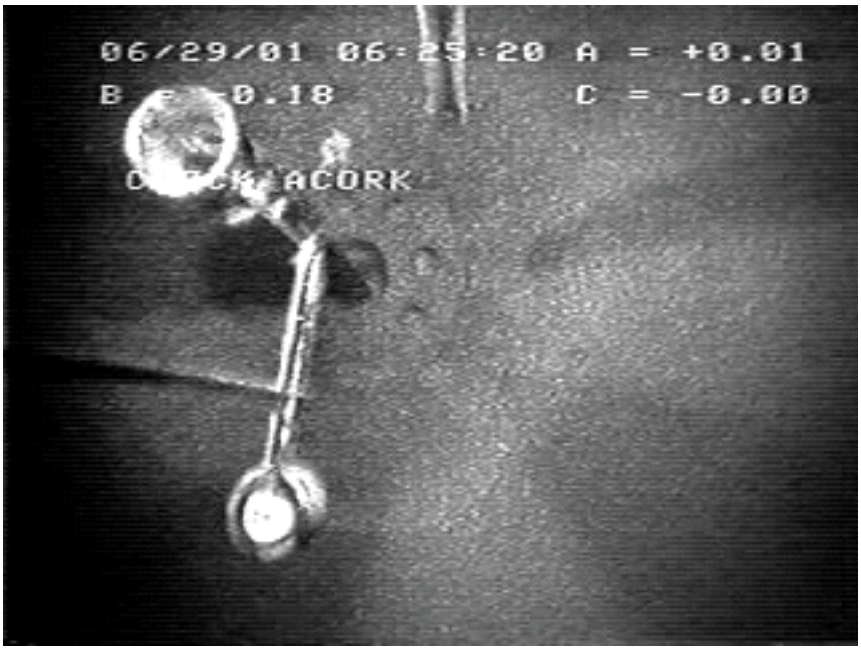

Figure F36. Core physical properties, Hole 1173B. In the velocity panel, solid circles = transverse velocities (z direction), open circles = longitudinal velocities (averages in the x and y directions).

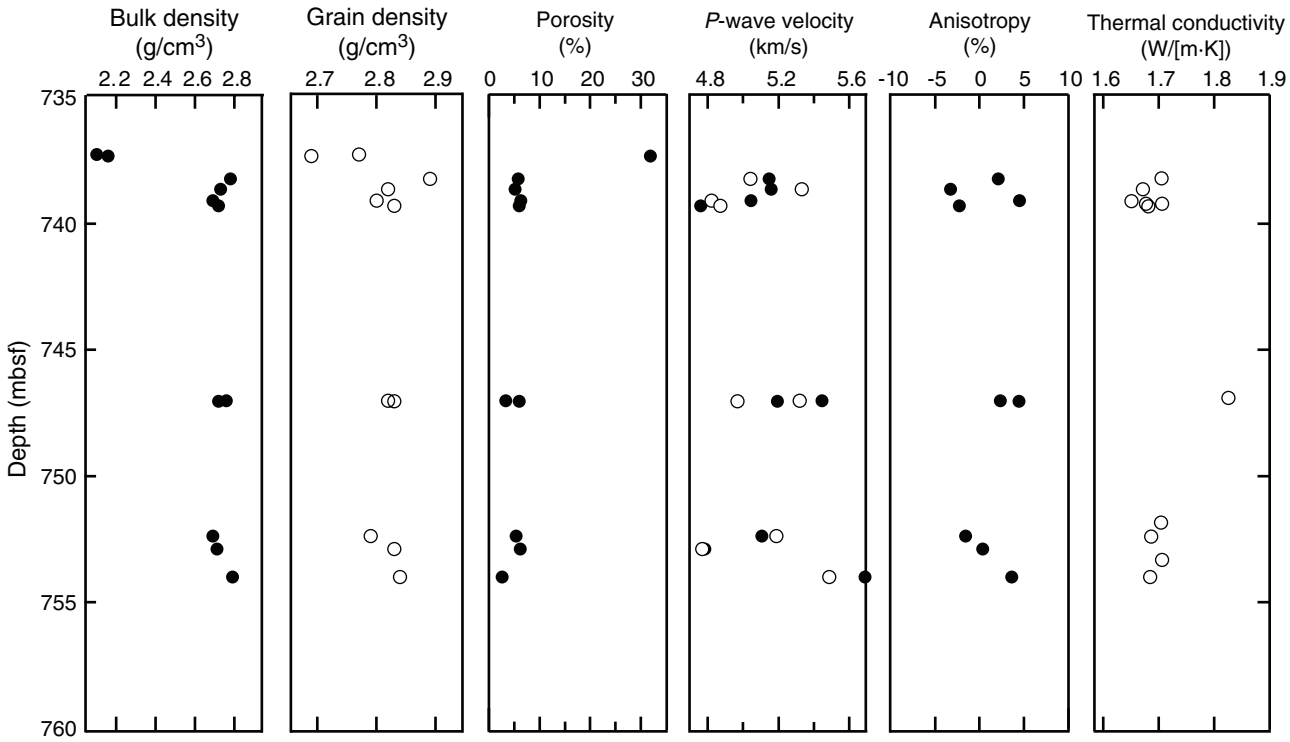

Figure F37. Large olivine phenocryst in thin section **Sample 196-1173B-3R-1, 38–40 cm,** pseudomorphed by serpentine in fractures and by talc in the center of the grain. Field of view = 5.5 mm.

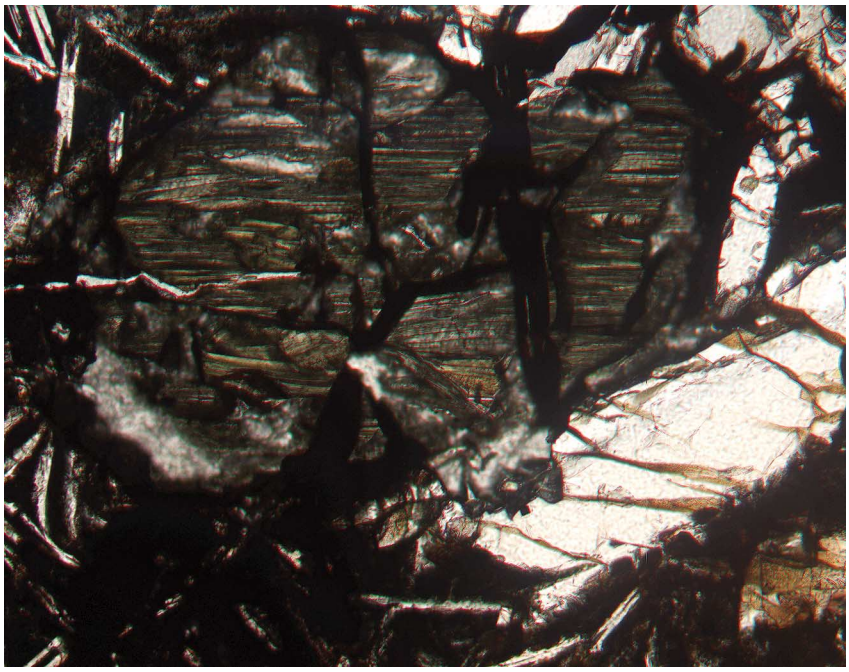

Figure F38. Fine-grained groundmass surrounding a microscopic amygdale in thin section **Sample 196-1173B-3R-2, 83–85 cm.** The intergranular groundmass texture is comprised of skeletal plagioclase with interstitial dendritic clinopyroxene and subordinate titanomagnetite. Field of view = 5.0 mm.

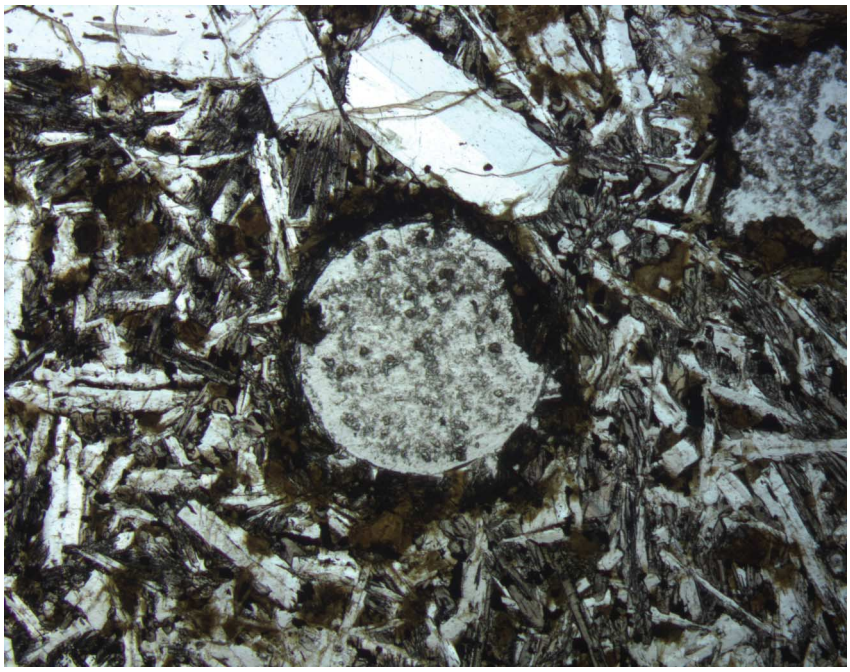

Figure F39. Variolitic texture in thin section **Sample 196-1173B-1R-2, 18–20 cm,** showing skeletal plagioclase laths with fans of dendritic clinopyroxene. Field of view = 2.5 mm.

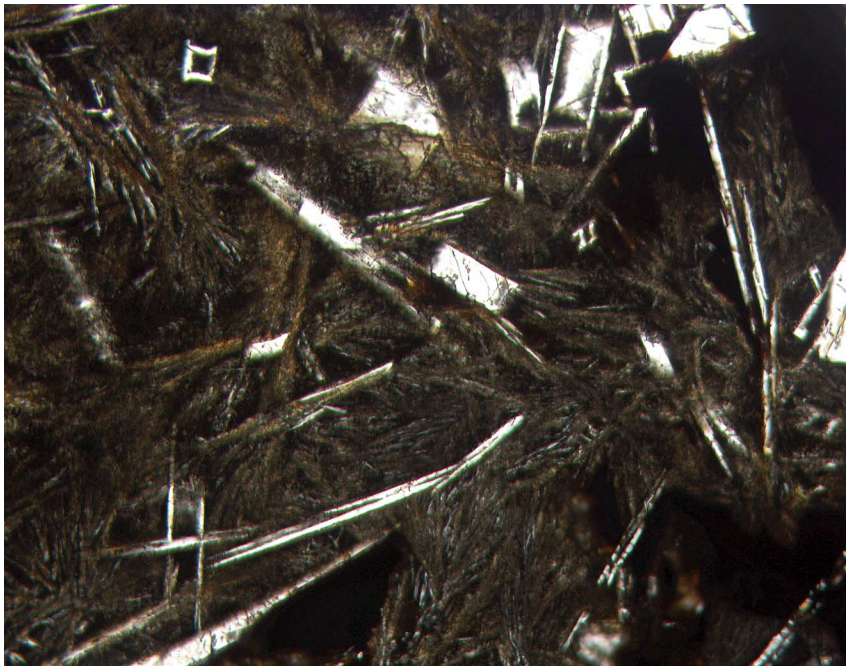

Figure F40. Zidjerveld diagrams of alternating-field (AF) demagnetization data and normalized AF demagnetization spectra of minicores, Hole 1173B. Open squares = inclination vectors, solid circles = declination vectors. **A.** Sample 196-1173B-1R-1, 107–109 cm; NRM intensity = 2.29 A/m. **B.** Sample 196-1173B-1R-1, 141–143 cm; NRM intensity = 1.13 A/m. (Continued on next two pages.)

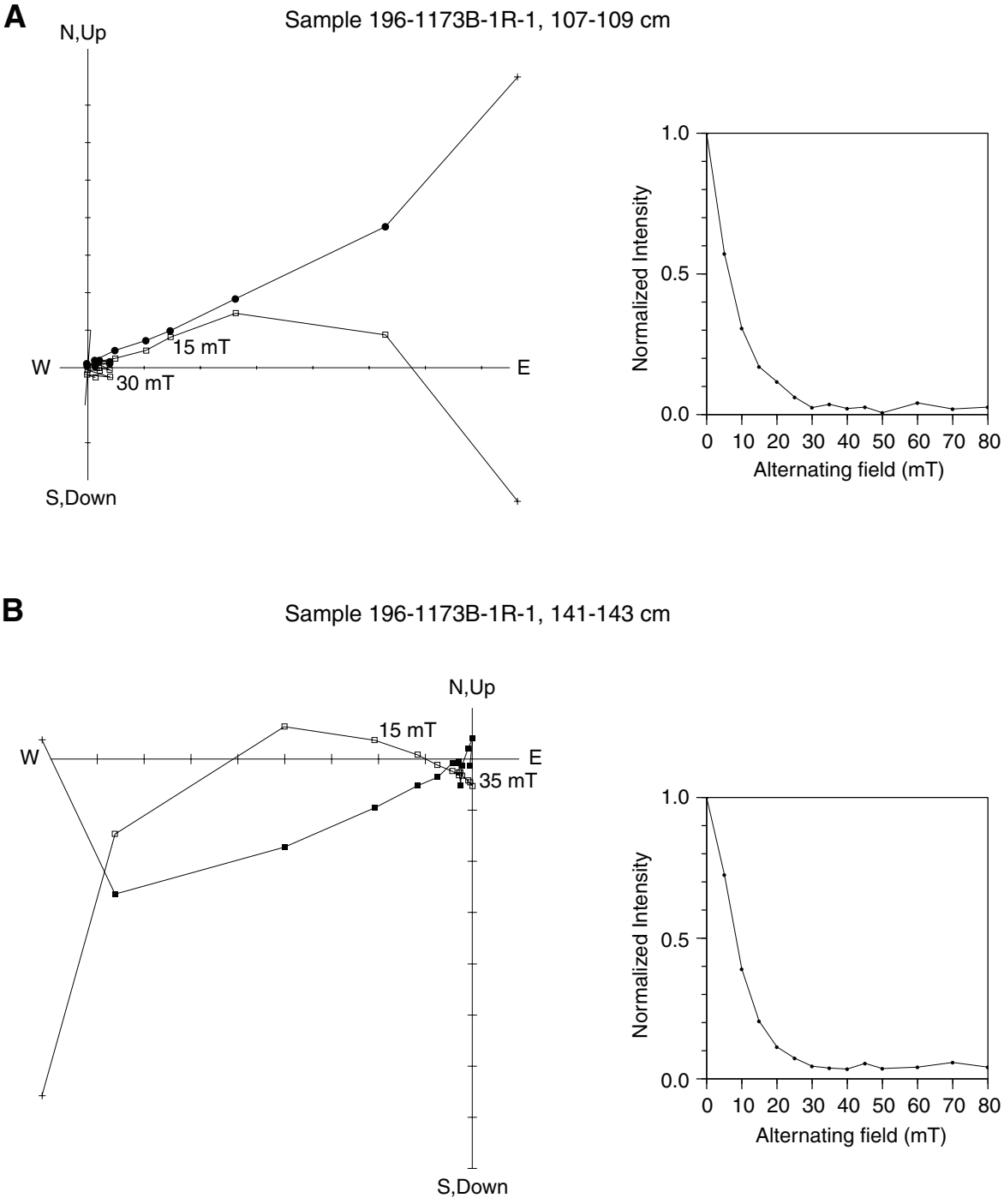

Figure F40 (continued). **C.** Sample 196-1173B-1R-2, 61–63 cm; NRM intensity 2.26 = A/m. **D.** Sample 196-1173B-2R-1, 34–36 cm; NRM intensity = 2.07 A/m.

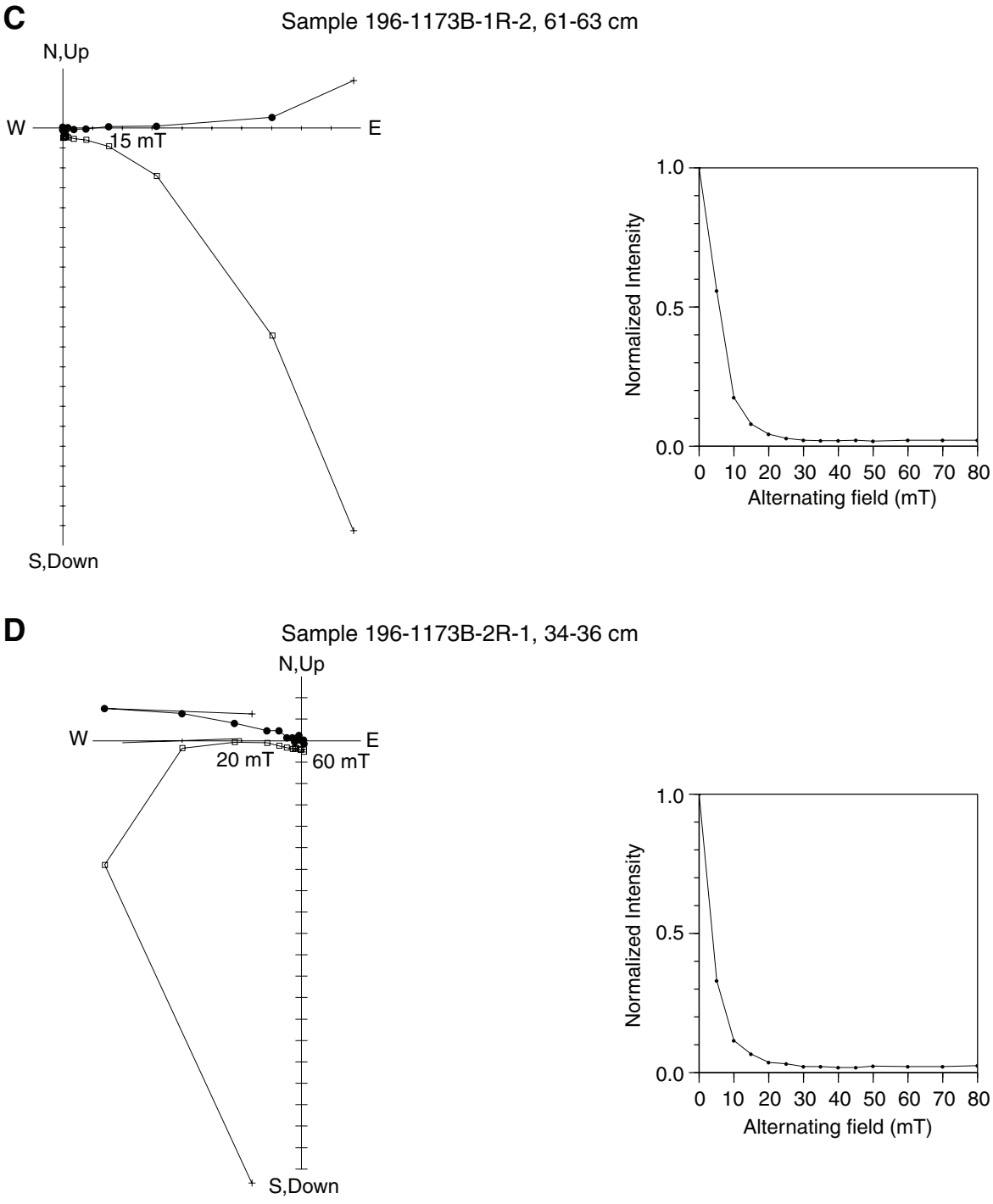

Figure F40 (continued). **E.** Sample 196-1173B-3R-1, 84–86 cm; NRM intensity = 1.50 A/m. **F.** Sample 196-1173B-3R-2, 14–16 cm; NRM intensity = 1.11 A/m.

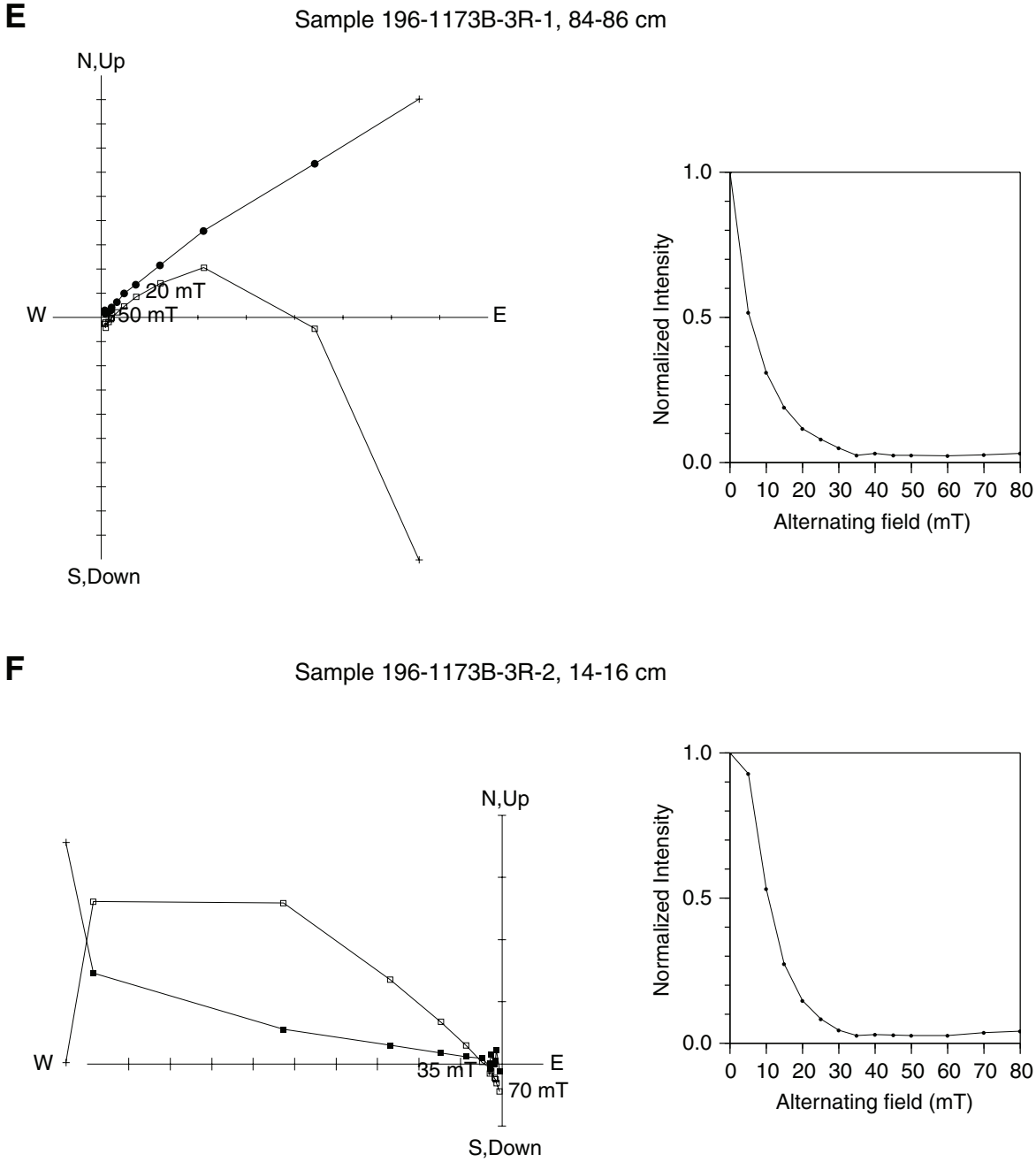

Figure F41. Possible age of Site 1173 indicated along with the geomagnetic polarity timescale of Cande and Kent (1995).

Figure F42. Comparison of Hole 1173A Formation MicroScanner (FMS) and Hole 1173B resistivity-at-the-bit (RAB) resistivity images of the basal ash layer and log Unit 2/3 boundary, 330–350 mbsf.

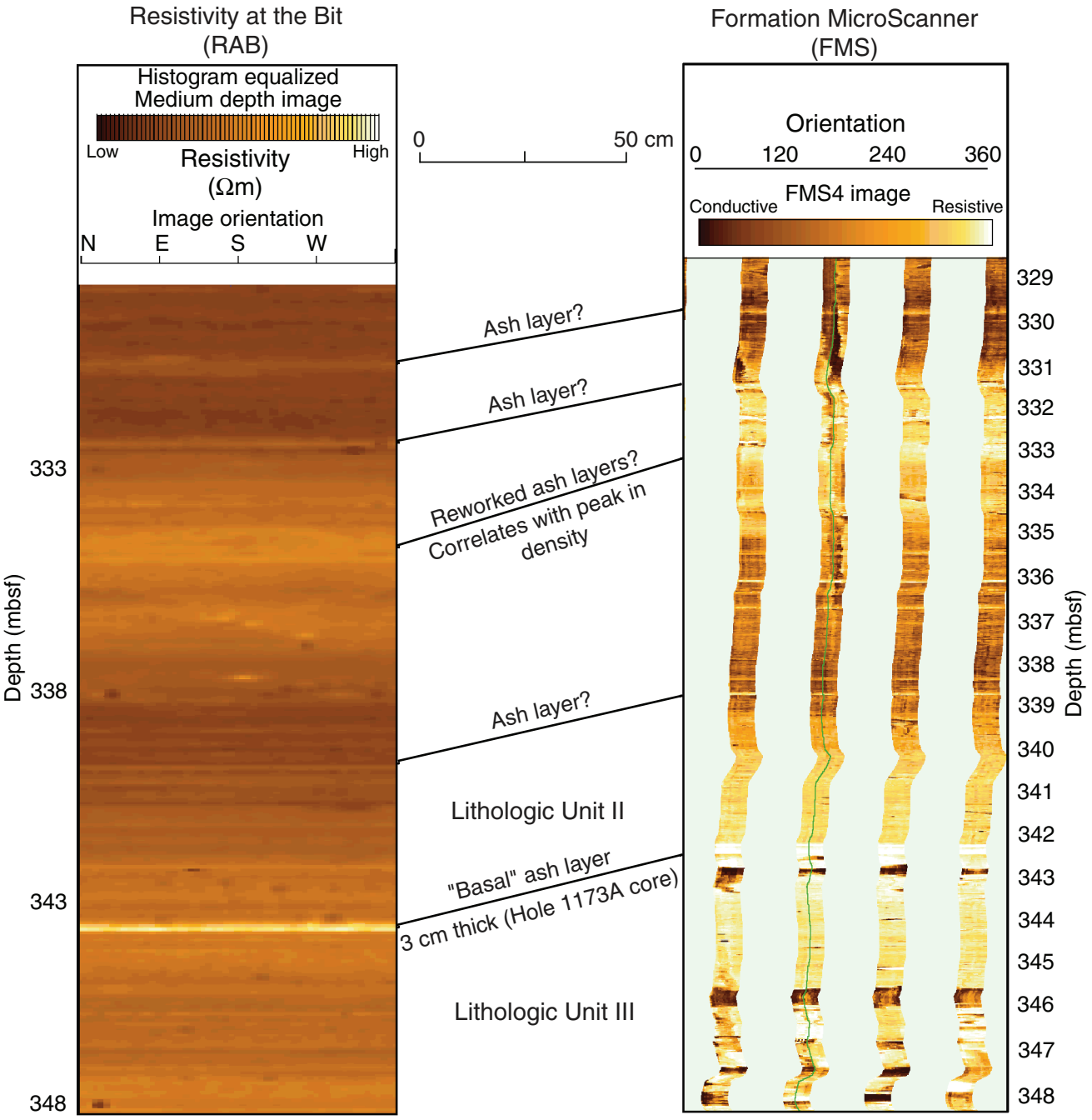

Figure F43. Detailed log properties of the Site 1173 interval around the stratigraphic equivalent of the Site 1174 décollement zone, projected by correlating core magnetic susceptibility patterns among Sites 808, 1173, 1174, and 1177.

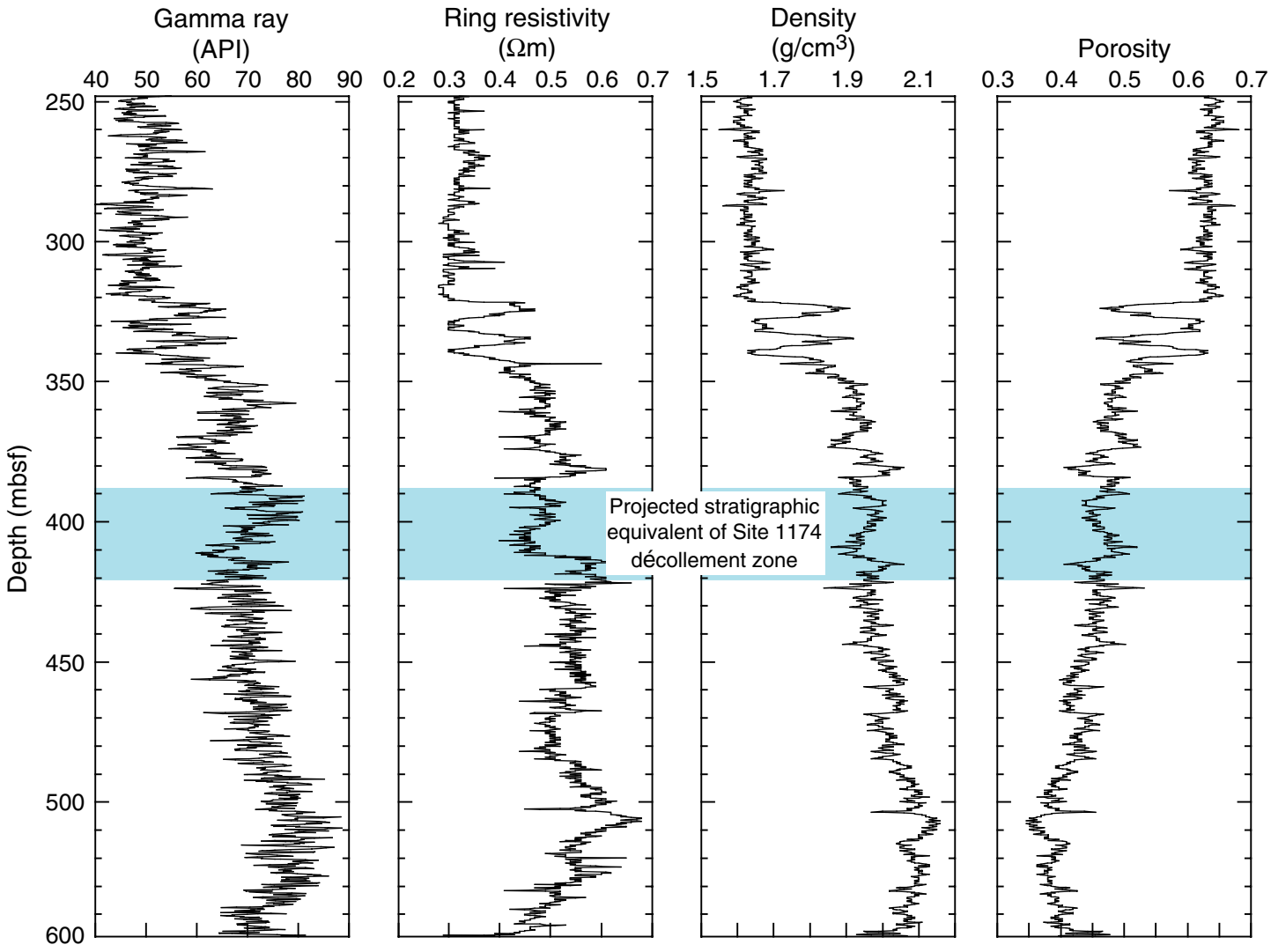

Table T1. Operations summary, Site 1173.

Hole 1173B
Latitude: 32°14.6831′N
Longitude: 135°01.4845′E
Seafloor (drill pipe measurement from rig floor, mbrf): 4801.9
Distance between rig floor and sea level (m): 10.8
Water depth (drill pipe measurement from sea level, m): 4791.1

Hole 1173C
Latitude: 32°14.6978′N
Longitude: 135°01.4612′E
Seafloor (drill pipe measurement from rig floor, mbrf): 4801.9
Distance between rig floor and sea level (m): 10.8
Water depth (drill pipe measurement from sea level, m): 4791.1

Operation	Start		End		Depth (mbsf)		Drilled (mbsf)	Time on hole		Comments
	Date (2001)	Time (local)	Date (2001)	Time (local)	Top	Bottom		Hours	Days	
196-1173B:										
Install reentry cone and 20-in casing	10 May	0224	13 May	2315	0	124.2	124.2	88.5	3.69	20-in casing shoe at 120.6 mbsf; includes 43 hr due to reentry cone loss.
LWD	13 May	2315	17 May	2135	124.2	737.1	612.9	94.3	3.93	Includes 24 hr spent evading tropical storm.
Open 9⅞-in LWD hole to 17½ in for ACORK	23 May	1910	2 Jun	0230	124.2	735.1	610.9	79.3	3.31	17½-in hole extends to 732.1 mbsf.
Assemble and drill in ACORK	2 Jun	0230	10 Jun	0445	—	—	—	194.2	8.09	ACORK extends from 0 to 727.10 mbsf; includes 58-hr DP transit back to site.
RCB core below ACORK: Open basement hydrologic system to deepest monitoring zone	10 Jun	0445	12 Jun	1615	737.1	756.6	19.5	59.5	2.48	Three cores; 19.5 m cored; 5.19 m recovered (27%).
Install bridge plug inside ACORK	12 Jun	1615	14 Jun	0000	—	—	—	31.7	1.32	Bridge plug set at 466 mbsf; drill pipe broke off at ACORK head.
Conduct camera survey of ACORK	29 Jun	0400	29 Jun	2215	—	—	—	18.3	0.76	
					Totals for Hole 1173B:		1367.5	565.8	23.58	
196-1173C:										
LWD	17 May	2135	18 May	1655	0	175.0	175.0	19.4	0.81	
					Totals for Hole 1173C:		175.0	19.4	0.81	
					Totals for Site 1173:		1542.5	585.2	24.39	

Notes: LWD = logging while drilling, ACORK = Advanced CORK, RCB = rotary core barrel. DP = dynamic positioning. — = not applicable.

Table T2. Heave compensator experiment, AHC-off intervals.

Interval	Depth (mbrf)		Depth (mbsf)		Stand length	Time (local)		
	Top	Bottom	Top	Bottom		Start	End	Date (May 2001)
1	4955.7	4974.7	153.8	172.8	Double	1623	1646	16
2	5080.0	5099.3	278.1	297.4	Single x2	2151	2125	16
3	5224.2	5243.3	422.3	441.4	Single x2	0214	0258	17
4	5387.7	5406.9	585.8	605.0	Double	0821	0852	17
5	5464.6	5493.9	662.7	691.6	Single + double	1120	1218	17
6	5527.0	5532.0	725.1	730.1	1/2 single	1403	1430	17

Note: AHC = active heave compensation system.

Table T3. Heave compensator experiment, AHC-preloaded intervals.

Interval	Depth (mbrf)		Depth (mbsf)		Stand length	Time (local)		
	Top	Bottom	Top	Bottom		Start	End	Date (May 2001)
1	5329.8	5358.7	527.9	556.8	Double + single	0623	0703	17
2	5406.9	5435.7	605.0	633.8	Single + double	0908	1001	17
3	5435.7	5464.6	633.8	662.7	Single + double	1001	1102	17
4	5522.3	5527.0	720.4	725.1	1/2 single	1312	1403	17

Note: AHC = active heave compensation system.

Table T4. Coring summary, Hole 1173B.

Core	Date (June 2001)	Time (local)	Depth (mbsf) Top	Depth (mbsf) Bottom	Length (m) Cored	Length (m) Recovered	Recovery (%)	Section	Length (m) Liner	Length (m) Curated	Section depth (mbsf) Top	Section depth (mbsf) Bottom
196-1173B-												
					***** Drilled from 0 to 737.1 mbsf *****							
1R	11	1545	737.1	746.8	9.7	2.34	24					
								1	0.96	1.48	737.10	738.58
								2	1.38	1.50	738.58	740.08
								3	0.00	0.12	740.08	740.20
								Totals:	2.34	3.10		
2R	12	0025	746.8	751.7	4.9	0.67	14					
								1	0.67	0.69	746.80	747.49
								Totals:	0.67	0.69		
3R	12	0445	751.7	756.6	4.9	2.18	45					
								1	0.98	1.50	751.70	753.20
								2	1.20	0.94	753.20	754.14
								Totals:	2.18	2.44		
				Cored totals:	19.5	5.19	27					
				Drilled total:	737.1							
				Total:	756.6							

Table T5. Mean values and standard deviations of log properties for each log unit, Holes 1173B and 1173C.

Log unit	Resistivity (Ωm)		Gamma ray (API)		Neutron porosity (pu)		Density (g/cm^3)		Photoelectric effect (b/e$^-$)		Differential caliper (in)	
	Mean	SD	Mean	SD	Mean	SD	Mean	SD	Mean	SD	Mean	SD
1	0.61	0.06	47.19	8.24	0.63	0.08	1.55	0.18	3.05	0.23	1.15	0.55
2	0.37	0.06	51.27	4.55	0.62	0.05	1.65	0.05	3.26	0.18	0.42	0.23
3	0.53	0.05	74.32	6.75	0.51	0.05	2.06	0.09	3.38	0.17	0.18	0.12
4	0.58	0.10	73.44	9.29	0.20	0.23	1.03	1.09	1.62	1.74	0.15	0.19
5	7.66	2.40	6.31	6.87								

Note: SD = standard deviation.

Table T6. Logging-while-drilling density trends with depth.

Depth (mbsf)	Mean density (g/cm^3)	Standard deviation (g/cm^3)	Characteristics
0–55	1.38	0.11	Rapid, stepped rise
55–122	1.69	0.05	Near constant
122–321	1.64	0.03	Near constant
321–340	1.75	0.09	High-amplitude variation
340–468	1.95	0.06	Gradual rise
468–503	2.04	0.04	Rapid rise
503–558	2.08	0.03	Gradual fall
558–698	2.15	0.04	Gradual rise

Table T7. Important components and their depths in the Advanced CORK deployed in Hole 1173B.

Component	Depth (mbsf)	Notes
Screen (center)	353.2	¼-in pressure monitoring line
Packer (center)	374.6	
Screen (center)	396.0	¼-in pressure monitoring line and ⅛-in geochemical sampling line
Packer (center)	417.7	
Screen (center)	439.2	¼-in pressure monitoring line
Packer (center)	495.5	
Screen (center)	563.4	¼-in pressure monitoring line
Packer (center)	712.2	
Screen (center)	722.1	¼-in pressure monitoring line
Casing shoe	727.8	
Rat hole	727.8–731.0	
Basement	731.0	
17½-in hole TD	732.1	
9⅞-in LWD TD	737.1	
9⅞-in RCB TD	756.6	

Note: TD = total depth, LWD = logging while drilling, RCB = rotary core barrel.

Table T8. *P*-wave velocity and moisture and density properties of core samples, Hole 1173B.

Core, section, interval (cm)	Piece	Depth (mbsf)	*P*-wave velocity				Density (g/cm³)		Porosity (%)	Comments
			x* (km/s)	y* (km/s)	z† (km/s)	Anisotropy (%)	Bulk	Grain		
196-1173B-										
1R-1, 13–20	—	737.27	—	—	—	—	2.10	2.77	38.43	Sediment
1R-1, 20–27	—	737.34	—	—	—	—	2.16	2.69	31.81	Sediment
1R-1, 113–115	23	738.24	4.93	5.15	5.15	2.1	2.78	2.89	5.78	Basalt
1R-2, 3–7	1	738.65	—	5.33	5.16	–3.3	2.73	2.82	5.09	Basalt
1R-2, 49–52	9	739.11	4.75	4.90	5.05	4.5	2.69	2.80	6.22	Basalt
1R-2, 69–72	11	739.31	4.87	4.60	4.76	–2.3	2.72	2.83	5.99	Basalt
2R-1, 21–24	4	747.03	5.32	5.32	5.45	2.3	2.76	2.82	3.31	Basalt
3R-1, 13–15	2	747.04	4.76	5.18	5.19	4.4	2.72	2.83	6.02	Basalt
3R-1, 67–69	12	752.38	5.11	5.27	5.11	–1.6	2.69	2.79	5.34	Basalt
3R-1, 118–120	17	752.89	4.73	4.81	4.78	0.3	2.71	2.83	6.17	Basalt
3R-2, 80–82	14	754.01	5.46	5.51	5.69	3.6	2.79	2.84	2.62	Basalt

Notes: * = velocity in the horizontal direction, † = velocity in the vertical direction. — = not measured.

Table T9. Thermal conductivity of basalt core samples, Hole 1173B.

Core, section, interval (cm)	Piece	Depth (mbsf)	Thermal conductivity (W/[m·K])	Standard deviation (W/[m·K])	Comments
196-1173B-					
1R-1, 105–116	23	738.21	1.71	0.04	
1R-2, 1–9	1	738.65	1.67	0.06	
1R-2, 49–56	9	739.13	1.65	0.02	
1R-2, 57–67	10	739.22	1.69	0.02	Vein inside
1R-2, 68–76	11	739.32	1.68	0.01	
2R-1, 23–40	4	746.92	1.83	0.03	Vertical vein
3R-1, 12–18	2	751.85	1.70	0.02	Small piece
3R-1, 65–74	12	752.40	1.69	0.02	
3R-2, 6–19	3	753.33	1.71	0.01	
3R-2, 77–83	14	754.00	1.68	0.01	Small piece

Table T10. Summary of volcanic textures. (See table notes. Continued on next two pages.)

Core, section	Interval (cm)	Piece	Unit	Plagioclase mode (%)	Phenocryst size (mm)	Olivine mode (%)	Phenocryst size (mm)	Unaltered olivine	Grain size	Crystallinity	Vesicularity	Segregation structures	Notes/interpretation
196-1173B-													
1R-1 (737.1 mbsf)*	35–39.5	8A	1	5	0.5–5.0	<0.5	<1		mc	hc	nv (<1%)	sv	Variolitic domains, close to a upper lobe boundary
	39.5–42	9A											Variolitic domains
	42–46.5	10A									spv	sv	Variolitic domains
	46.5–51	11A									nv		Variolitic domains
	51–55	12A											
	55–58	13A							mc/fg	c			
	58–65	14A											
	65–71	15A											
	71–74.5	16A											
	74.5–80	17A				<2	<1.5						
	80–84	18A							mc	hc			Variolitic domains
	84–94	19A							mc/cc	hc/hy	spv (3%)		Variolitic texture and boundary: 3-mm-thick silicified glassy selvage with relict domains of varioles (= quenched lobe margins)
	94–98	20A							mc	hyh/hc	nv		
	98–102	21A											
	102–106	22A							mc	hc	spv (3%)		
	106–116.5	23A							fg/mc	c	nv/spv		Amygdales contain secondary pyrite
	116.5–124.5	24A											Secondary pyrite lining the inner walls of vesicles
	124.5–133	25A							mc				
	133–139	26A											
	139–148	27A				2–3							
1R-2 (738.58 mbsf)*	1–11	1A	1	7	0.5–5.0	<2	0.3–2.0		fg	c	spv		
	11–16.5	2A							mc				Variolitic domains
	16.5–24	3A											Variolitic domains
	24–31	4A							mc	hc/hyh/G			Variolitic texture and boundary: 5-mm-thick silicified glassy selvage with relict domains of varioles (= quenched lobe margins)
	31–36	5A							mc	hc/c	nv		Variolitic domains
	36–40	6A									spv		Variolitic domains
	40–45	7A							mc	hyh/G			Variolitic texture and boundary: 5-mm-thick silicified glassy selvage with relict domains of varioles (= quenched lobe margins)
	45–49	8A							mc	hyh/hc	spv		Variolitic domains
	49–57	9A								hc/c			
	57–68	10A									nv		
	68–78	11A							mc	hc/hyh	spv (3%–5%)		Variolitic domains; close to lobe margins?
	78–88	12A							mc	hc/c	spv		
	88–95	13A											
	95–100.5	14A									nv		
	100.5–112.5	15A							fg/mc	c			
	112.5–118.5	16A											
	118.5–125	17A							mc	hc	spv		Variolitic domains; close to lobe margins?

Table T10 (continued).

Core, section	Interval (cm)	Piece	Unit	Plagioclase mode (%)	Phenocryst size (mm)	Olivine mode (%)	Phenocryst size (mm)	Unaltered olivine	Grain size	Crystallinity	Vesicularity	Segregation structures	Notes/interpretation
	125–132	18A							mc	hc	spv		Variolitic domains
	132–140	19A											
	140–146	20A									nv		
	146–150	21A									spv		
2R-1 (746.8 mbsf)†	0–5	1A	1	5	0.5–4.0				mc	hc/c	spv		Variolitic domains; close to lobe margins?
	5–8	2A									spv/mov		
	8–19.5	3A								c	mov		
	19.5–53	4A								c	spv		
	53–63	5A								hc/hyh	spv		Variolitic domains; close to lobe margins?
	63–69	6A							mc/fg	c	spv/mov		
3R-1 (751.7 mbsf)‡	0–11	1A	2	10	0.5–5.0	2–3	0.2–2	ol	fg	c	nv (<1%)		Variolitic domains
	11–19	2A											Variolitic domains
	19–22	3A							mc	hc/G	spv/mi		Variolitic texture and boundary: 5-mm-thick silicified glassy selvage with relict domains of varioles (= quenched lobe margins)
	22–25	4A								c	spv		
	25–28	5A								c/hc	spv/mov		Close to boundary: fining of grain size and dominance of variolitic texture in groundmass
	28–32.5	6A						ol			nv		
	32.5–36.5	7A								hc	spv		Close to boundary: fining of grain size and dominance of variolitic texture in groundmass
	36.5–40	8A						ol			nv		
	40–43	9A											Variolitic domains
	43–55	10A									spv (3%)		Variolitic domains
	55–63.5	11A				1–3					spv (3%–5%)		Variolitic domains
	63.5–88	12A							mc/cc	hc/hy	spv		Close to boundary: fining of grain size and dominance of variolitic texture in groundmass
	88–95	12C							mc/fg	c			
	95–98	13A							mc/cc	hc/hy	nv		Close to boundary: fining of grain size and dominance of variolitic texture in groundmass
	98–105	14A							mc	hc	spv (3%)		
	105–110.5	15A							mc/cc	hy/G	nv		Variolitic texture and boundary: 3-mm-thick silicified glassy selvage with relict domains of varioles (= quenched lobe margins)
	110.5–116	16A							mc/cc	hc/hy	nv		Variolitic texture and boundary: 3-mm-thick silicified glassy selvage with relict domains of varioles (= quenched lobe margins)
	116–128	17A						ol	mc	hc	spv (3%)		
	128–132.5	18A						ol	mc	hc	spv (3%)		
	132.5–144.5	19A				2–3			mc	hc	nv		Variolitic groundmass texture
	144.5–149.5	20A				2–3			mc	hc	nv		Variolitic groundmass texture; approaching a boundary?

Table T10 (continued).

Core, section	Interval (cm)	Piece	Unit	Plagioclase mode (%)	Phenocryst size (mm)	Olivine mode (%)	Phenocryst size (mm)	Unaltered olivine	Grain size	Crystallinity	Vesicularity	Segregation structures	Notes/interpretation
3R-2 (753.2 mbsf)‡	0–3	1A	2	10	0.5–5.0	2–4	0.2–2		mc	c/hc	spv		
	3–6	2A											Variolitic texture
	6–20	3A							mc	hc/hy	spv		Variolitic texture
	20–23	4A							mc/cc	hc/G	spv		Variolitic texture and boundary: 3-mm-thick silicified glassy selvage with relict domains of varioles (= quenched lobe margins)
	23–29	5A							mc	hc/c	nv		Variolitic texture
	29–32.5	6A								hc			
	32.5–36	7A											Variolitic texture
	36–45.5	8A								hc/hy	spv (2%)		Variolitic texture
	45.5–52.5	9A									nv		Variolitic domains
	52.5–56.5	10A							cc/mc	hy			Close to boundary: fining of grain size and dominance of variolitic texture in groundmass
	56.5–62	11A							mc	hc	nv		Close to boundary: fining of grain size and dominance of variolitic texture in groundmass
	62–65	12A											Variolitic texture
	65–76	13A							mc/cc/G	hc/hy	nv/spv		Variolitic texture and boundary: 2-mm-thick glassy rind with film of vitric tuff adhering to surface (= quenched lobe margins)
	76–86	14A							mc	hc	spv (3%–5%)		

Notes: * = Sparsely to moderately plagioclase-olivine-phyric basalt (groundmass texture is intergranular with plagioclase needles and interstitial feathery pyroxene, unless specified otherwise); † = Sparsely to moderately plagioclase-phyric basalt (groundmass texture is intergranular with plagioclase needles and interstitial feathery pyroxene, unless specified otherwise), ‡ = Moderately plagioclase-olivine phyric basalt (groundmass texture is intergranular with plagioclase needles and interstitial feathery pyroxene, unless specified otherwise). Abbreviations: see Figure **F12**, p. 47, in the "Explanatory Notes" chapter for definitions.

Table T11. Chemical analyses of basalts, Hole 1173B.

	Sample 196-1173B-1R-1, 99–101 cm	Sample 196-1173B-3R-2, 83–85 cm
Major oxides (wt%):		
SiO_2	48.78	48.85
MnO	0.26	0.13
Fe_2O_3	10.61	9.78
MgO	5.95	6.19
TiO_2	1.95	1.53
CaO	11.91	11.62
Al_2O_3	16.46	16.99
Na_2O	3.06	2.96
K_2O	0.25	0.12
P_2O_5	0.24	0.17
Totals	99.46	98.35
LOI	1.62	2.02
Trace elements (ppm):		
Ni	76	88
Cr	213	243
V	341	279
Zr	170	133
Sc	42	38
Y	39	33
Sr	236	215
Ba	21	17
Co	58	51
Cu	113	82
Zn	92	74

Note: LOI = loss on ignition.

Table T12. Characteristic remanent magnetization (ChRM) inclinations fit by principal component analysis of alternating-field demagnetization data.

Core, section, interval (cm)	*N*	Demagnetization step (mT)	MAD (°)	ChRM inclination (°)	*k* ($\times 10^{-6}$ SI)	Koenigsberger ratio
196-1173B-						
1R-1, 107	5 (+o)	15–30	5.3	–23.1	7195	8.71
1R-1, 141	5	15–35	2.9	–18.7	6545	4.73
1R-2, 61	NA	NA	NA	NA	6300	9.82
2R-1, 34	6*	20–60	11.1	–22.8	5680	9.98
3R-1, 84	7	20–50	3.9	–38.2	5660	7.26
3R-2, 14	6	35–70	29.7	–38.1	4550	6.68

Notes: *N* = number of demagnetization points used in fit. MAD = median angular deviation of the directional fit. The magnetic susceptibility (*k*) was volume normalized assuming a 10-cm^3 sample. Koenigsberger ratio = NRM/($k \times$ H), where NRM is the intensity of the natural remanent magnetization and H is the strength of Earth's present-day magnetic field at the site (36.5 A/m). +o = origin included in the fit, * = outliers excluded from fit, NA = fit not available.